NORTHWESTERN UNIVERSITY

Complex Patterns in Oscillatory Systems

A DISSERTATION

SUBMITTED TO THE GRADUATE SCHOOL

IN PARTIAL FULFILLMENT OF THE REQUIREMENTS

for the degree

DOCTOR OF PHILOSOPHY

Field of Applied Mathematics

By

Jessica Maral Conway

EVANSTON, ILLINOIS

December 2008

ABSTRACT

Complex Patterns in Oscillatory Systems

Jessica Maral Conway

Motivated by the rich variety of complex patterns observed on the surface of fluid layers that are vibrated at multiple frequencies, we investigate the effect of such resonant forcing on systems undergoing a Hopf bifurcation to spatially homogeneous oscillations. We use an extension of the complex Ginzburg-Landau equation (CGLE) that systematically captures weak forcing functions with a spectrum consisting of frequencies close to the 1:1-, 2:1-, and 3:1-resonance. We first examine the case where the multi-resonant forcing is unmodulated in time. Our third-order, weakly nonlinear analysis shows that for small amplitudes only stripe patterns or hexagons (up *and* down) are linearly stable; for larger amplitudes rectangles and super-hexagons (or super-triangles) may become stable. The larger-amplitude super-hexagons arise in a transcritical bifurcation because of the quadratic interaction introduced by the 3:1-forcing, and are linearly stable only on the upper branch. Numerical simulations show, however, that in the latter regime the third-order analysis is insufficient: super-hexagons are unstable. Instead large-amplitude hexagons can arise and be bistable with the weakly nonlinear hexagons.

By slowly modulating the amplitude of the 2:1-forcing component we render the bifurcation to subharmonic patterns subcritical despite the quadratic interaction introduced by the 3:1-forcing, so there is always a range in which the weakly nonlinear analysis with cubic truncation is valid. Our weakly nonlinear analysis shows that quite generally the forcing function can be tuned such that resonant triad interactions with weakly damped modes stabilize subharmonic patterns comprised of four or five Fourier modes, similar to quasi-patterns exhibiting elements with 4-fold and 5-fold rotational symmetry, respectively. Using direct simulations of the extended CGLE we confirm our weakly nonlinear analysis. In simulations domains of different complex patterns compete with each other on a slow time scale. As expected from energy arguments, with increasing strength of the triad interaction the more complex patterns eventually win out against the simpler patterns. We characterize these ordering dynamics using the spectral entropy of the patterns. For system parameters reported for experiments on the oscillatory Belousov-Zhabotinsky reaction we explicitly show that the forcing parameters can be tuned such that 4-mode patterns are the preferred patterns.

Acknowledgements

This marks the end of my Ph.D. career and, like anyone in my position, I didn't make it through on my own. I owe many a debt of gratitude for their help along the way. I don't know that I can ever really convey how much I appreciate the aide and support I have been lucky enough to have over the years, but I'll try.

First I'd like to thank my defense committee, Drs. Hermann Riecke, Mary Silber, and Vladimir Volpert. Your thoughful questions and comments greatly improved the final version of mydissertation. I'd also like to thank Dr. Silber for being open to and available for questions when my own advisor was away, and Dr. Volpert for just being Dr. Volpert.

But in particular I want to thank my advisor Dr. Hermann Riecke. Any good qualities I now possess as a math person or scientist I owe to you. I will forever hear your voice saying "Slowly, slowly" any time I rush to quickly through an explanation or a calculation. You met any discouragement on my part with enthusiasm, and any slowness in understanding with patience. And thank you, and also Marge, Charlie, and Toby, for welcoming me at family dinners while we were in Heidelberg. It made my time there so much more pleasant!

And to my parents, thanks for listening to me whine and offering advice and being supportive even when I didn't take it - simply put, thanks for putting up with me! I'm sorry that I didn't visit home as much as you (or I) would have liked. To my sisters, Stéphanie and Élise, well, thanks for letting me back in the house at Christmas. :) I know

that we don't always get along, and I hope that someday that will change. Thank you for picking up the slack for me at home, like when we planned Mom & Dad's anniversary party. It made being away, and completing this degree, so much easier.

I got to Northwestern in the first place with the help of my old friend Diego Galindo up at the University of Wisconsin: he and I moved to the midwest together (sorry I fell asleep while you were driving the U-Haul truck!). Thank you Diego for your support over the years. And for helping me move again in Evanston after that slight flooding incident!

Upon arrival, nervous and new to the department and to the country, I was made to feel very much at home. Support staff member Judy Piehl and department chair Alvin Bayliss were in particular welcoming. After Judy retired Beth Siculan joined the support staff - Beth, you make visiting the main office a pleasure! It was always nice to be able to go down the hall and have a fun chat with you and Mary Catsicopoulos, or Mo Ormiston, or Danielle Jackson, or Molly Scanlon.

The IT staff was always there when something went wrong. Which is good because I spent a lot of time on computers here, especially good ol' Venus! In particular Ken Kalan, who made a hard drive disaster no big deal, and Joe Urbanski, who said it was ok to nag him, thank you. And of course there's my first line of IT defense, my office mate of 5 years, Justin Kao. On the scale of me to him, Justin's a Linux expert. Thanks; I bet you'll miss my asking "Hey Justin, how do I...?" at least once a week.

Anthony Anderson, Anne Catllá, Daniel Grady, Margo Levine, Brian Merkey, David Salac, Christine Sample, Elaine Spiller, Liam Stanton, and Stuart Wick were all kind enough at various stages to hear me practice different talks, and offered valuable feedback. If there's anyone I forgot I'm sorry, know that I appreciate it. Anne and Tony

were also kind enough to take time out to read my dissertation and offer suggestions for improvement. Anne owed me but now... Tony don't hesitate to send your dissertation my way when your turn comes!

I'll miss "Russian nights," hosted by Sasha Golovin. Sasha, you and Anna and Peter made us feel welcome in your home, and I always had a great time. I'll miss coffee breaks with my caffeine habit enablers: Anne and Elaine (early on) and Tony (who helped me let go of my juvenile desire to add milk and sugar to my coffee).

Finally, I'll miss the many friends I made here at ESAM and in Evanston in general, beyond those mentioned above. Like the gang with whom I played cards over lunches in my second year. And only you suffered the consequences (ha ha)! There are two points of constant debate amongst us that I'd like to address: (a) the better sandwich shop - the CLEAR winner is Al's Deli, especially on pea soup days. Rollin' To Go? No. (b) the lower form of humour, puns or sarcasm - Puns are the lower form of humour. I don't know why it's not as obvious to everyone! There. It's in print, in black and white, and therefore must be true. Anyway, thank you all for your support and for just being there, to grab a meal with, to grab a drink with, to bowl a few frames with, to make me laugh. I'm very glad to have met you all.

Table of Contents

List of Figures

CHAPTER 1

Introduction

1.1. Motivation

Spontaneous pattern formation is a phenomenon that has been observed in physical, biological, and chemical non-equilibrium systems in many forms, from wind-driven sand ripples [**1**], to fluid convection [**2**]. Understanding spatio-temporal order in open systems kept far from equilibrium has been the objective of much theoretical and experimental research [**3**, **4**]. The objective of this dissertation is to show stability of complex patterns in oscillatory systems, a particular class of non-equilibrium system, which we will meet by using tools developed in the study of complex patterns in Faraday wave systems.

Stripe, square, and hexagon patterns constitute simple patterns, and can be thought of as tiling the plane with a single element. These patterns can be constructed by the superposition of one, two, or three appropriately-oriented standing waves, respectively. Specifically, square patterns arise from the interaction of perpendicular standing waves, and hexagon patterns arise from the interaction of standing waves 60° degrees apart. The complex patterns that we have in mind can be constructed from a more elaborate combination of standing waves.

We consider two types of complex patterns, superlattice patterns and quasi-patterns. Superlattice patterns are ordered and spatially periodic patterns; they are distinct from simple planar patterns in that they are characterized by two length scales. For example,

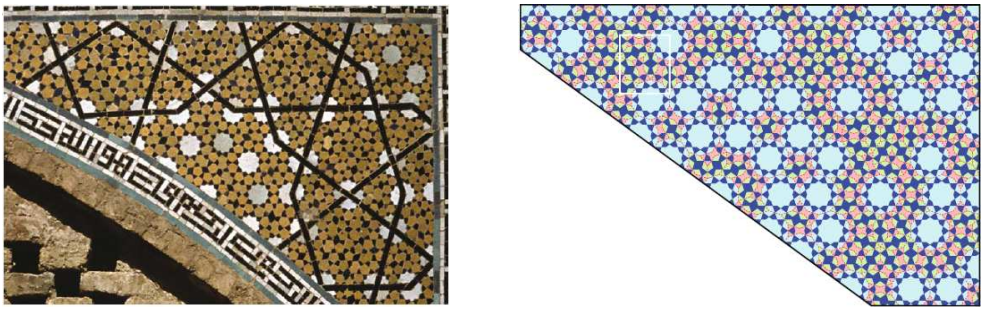

(a) (b)

Figure 1.1. 10-fold quasi-pattern - decagonal girih pattern above an arched doorway in the Darb-i Imam shrine, Isfahan, Iran (1453 C.E.). (A) Photograph of the spandrel. (B) Reconstruction of the smaller-scale pattern using girih tiles, which helps clarify the quasi-pattern aspect of the tile pattern. Note the local 10-fold rotational symmetry, but the lack of translational symmetry. Figures from [**6**]. Reprinted with permission from AAAS.

there may be some smaller spatial structure on one length scale and spatial periodicity on the other. Quasi-patterns are patterns that possess the same spatial symmetries as quasi-crystals obtained in metal alloys at thermodynamic equilibrium [**5**]. The essential spatial features of quasi-patterns are beautifully illustrated in Fig.1.1 which shows a tiling pattern, constructed from five tile shapes, on a spandrel at the Darb-i Imam shrine, Isfahan, Iran (1453 C.E.) [**6**]. Quasi-patterns are aperiodic, lacking the translational symmetry of the superlattice or simple planar patterns. However, the Fourier spectrum of a quasi-pattern has discrete rotational symmetry. This is reflected in the pattern itself by elements of local rotational symmetry and preferred orientation. The latter appears in Fig.1.1 in the alignment of the large, blue circles.

Complex patterns have been observed in a variety of non-equilibrium systems, for example on the surface of ferrofluids driven by time-periodic magnetic fields, where they are due to spatial period-doubling [**7**]. In particular, various kinds of superlattice patterns

and quasi-patterns have been found experimentally in Faraday systems - in which a layer of fluid is vertically vibrated [**8**] - depending on the frequency content of the forcing function [**9**–**17**].

In this dissertation, motivated by the richness of patterns observed in the Faraday system, we investigate whether such complex spatio-temporal patterns are also accessible in systems undergoing a Hopf bifurcation to spatially homogeneous oscillations. These systems constitute a class that differs from those in which quasi-patterns have been observed previously and they may offer the potential for additional complexity through the interaction between the spontaneous oscillations arising from the Hopf bifurcation and the external forcing. Chemical oscillations like those observed in the Belousov-Zhabotinsky reaction are a classic example of such a system.

In the absence of any temporal forcing, the Hopf bifurcations we have in mind lead to spatially homogeneous oscillations or long-wave traveling waves, which may break up to form spirals or more complex chaotic states (e.g. [**18**–**22**]). With temporal forcing, which in the case of the Belousov-Zhabotinsky reaction can be achieved by time-dependent illumination to exploit the photosensitivity of the reaction, the oscillations can become locked to the forcing and - depending on the ratio between the Hopf frequency and the forcing frequency - different types of patterns can arise [**23**–**28**]. Forcing near twice the Hopf frequency can lead to competition between two types of domains differing in their temporal phase or to labyrinthine patterns. For a frequency ratio of 1:3, spiral patterns or competing domains have been observed. So far, ordered patterns with multiple length scales have been observed experimentally in chemical systems only when a spatially

periodic illumination mask was applied to initialize the pattern [**29**, **30**]. We focus on the case of spatially uniform illumination.

The temporal aspect of the forcing greatly increases the diversity of patterns accessible in non-equilibrium systems. And while stable quasi-patterns have been shown with single-frequency forcing [**16**,**31**], experiments and analysis of Faraday waves employing simultaneous forcing at multiple frequencies have been much more fruitful. Specifically the ability to control in detail the temporal wave form of the vibration's forcing contributes to the great variety of complex patterns observed in the Faraday system [**11**, **13**, **15**, **32**, **33**]. This allows extensive tuning of the interaction between plane waves of different orientation, which can in turn stabilize superlattice patterns and quasi-patterns. Two main stabilization mechanisms have been identified, both of which exploit the presence of weakly damped resonating modes. The idea comes from the study of quasi-crystals in thermodynamic equilibrium, where the significance of damped, resonating modes has been recognized for the stabilization [**34**–**36**].

In the first mechanism, the competition between plane-wave modes of different orientation is suppressed for a relatively narrow range in the angle subtended by the competing modes [**32**, **33**, **37**–**40**]. Fourier modes between which the competition is suppressed can stably co-exist in the same pattern. Since suppression is only in a narrow range in the angle, control over this range allows the selection of modes that will co-exist in a stable pattern. In the second mechanism the damping self-coupling of each mode is strongly enhanced, rendering the competitive coupling between the modes effectively weak over a considerable range in the angle [**31**, **39**–**45**] and allowing patterns comprised of multiple modes to become stable [**35**]. The latter mechanism captures qualitatively the scenario

envisioned for the stabilization of 'turbulent crystals' [**36**]. Both mechanisms have been used to stabilize a variety of superlattice patterns and quasi-patterns in Faraday waves (cf. [**15**]). We will use both mechanisms in the context of oscillatory systems, and in particular exploit the second to stabilize complex patterns.

The results presented in this dissertation are in an oscillatory system but below the onset of oscillations. In this regime, resonant forcing can still induce instabilities to spatial perturbations and produce ordered patterns. By manipulation of the temporal wave form of the forcing function, mimicking the approach and mechanisms used in Faraday waves to produce complex patterns, we will demonstrate the stability of patterns similar to quasi-patterns exhibiting elements with 4- and 5-fold rotational symmetry.

1.2. Organization of dissertation

The organization of this dissertation is as follows. We begin in Chapter 2 with a review of oscillatory systems in the context of chemical oscillators. Our focus is on the historical development of the study of such non-equilibrium systems, and on understanding the pattern-forming instabilities that lead to dissipative spatial structures in that context.

In Part 1, we examine the case of an oscillatory system just below the onset of spontaneous oscillations, the Hopf bifurcation point, forced near the 1:1, 2:1, and 3:1 resonances. This work has been published [**46**]. In Chapter 3, we first extend the complex Ginzburg-Landau equation (CGLE) to include the terms that describe the external forcing. The CGLE is the equation that generically models systems near a Hopf bifurcation. In Chapter 4, we perform a linear stability analysis of the zero-solution of the CGLE to find the onset of instability. We perform a weakly nonlinear analysis about that point to obtain

amplitude equations for rectangle, hexagon, and super-hexagon patterns. Using the amplitude equations, we calculate the linear stability of these patterns in different regimes of CGLE parameters, and verify the stability predictions through numerical simulation of the CGLE. Chapter 5 contains conclusions from Part 1.

Part 2 begins with Chapter 6 in which we extend the complex Ginzburg-Landau equation (CGLE) to include the terms that describe the external forcing at various frequencies including modulation of the forcing near twice resonance. This inclusion is inspired by our results from Part 1. The derivation of this equation for the Brusselator, which is a simple model for chemical oscillations, is sketched in the Appendix. A brief account of this work has been published [**47**], and a more detailed account submitted for publication [**48**]. In Chapter 7, we present a linear stability analysis of the equation to find the onset of standing waves that are phase-locked to the driving. In particular, we focus on the vicinity of the codimension-2 point at which the subharmonic and the harmonic standing waves bifurcate simultaneously. To determine the stability of the desired subharmonic patterns, we derive in Chapter 8 the corresponding amplitude equations by performing a weakly nonlinear analysis of the CGLE, and then use energy arguments to guide us in terms of the relative stability of various pattern comprised of different numbers of modes. In order to confirm our predictions for the pattern selection, we perform in Chapter 9 numerical simulations of the CGLE in small and large domains, and characterize the temporal evolution of patterns by using a spectral pattern entropy. Chapter 10 contains conclusions from Part 2, and discusses possible extensions of this work.

CHAPTER 2

Oscillatory Systems Background

This dissertation centers on the resonant excitation of complex spatial patterns in media that naturally oscillate in time. Though the results we will present apply to any systems that undergo a Hopf bifurcation to spatially homogeneous oscillations, we will focus on chemical oscillator systems. In this chapter we offer an overview of chemical oscillators, paying special attention to pattern formation and the effects of forcing at a single resonant frequency in nonlinear chemical dynamics. Comprehensive reviews can be found in [**49**–**52**]. As will be discussed, chemical oscillations are a non-equilibrium phenomenon, and the field of non-equilibrium dynamics was developed because of irrefutable evidence of chemical oscillations. A thorough review of pattern formation outside of equilibrium can be found in [**3**].

This chapter is organized as follows. In Section 2.1 we give an overview of the history of oscillatory chemical reactions. We discuss in Section 2.2 the Turing instability and both analytic and experimental results of the resulting periodic structures, including complex patterns. Then in Section 2.3 we discuss the effects of resonant forcing on the system above the onset of spontaneous oscillations. Finally in Section 2.4 we summarize the main points of this chapter.

2.1. Beginnings - reactions can be oscillatory?

In 1828 Fechner described oscillating current in an electro-chemical cell in *Schweigg J.* as reported in [**49**, **50**]; this constitutes the first published instance of oscillations in a chemical system. Then in 1899 Wilhelm Ostwald reported in *Phys. Z.* a periodic increase and decrease in the rate of chromium dissolution in acid (cited in [**50**]). In both these instances the chemical oscillations arise through an inhomogeneous reaction, in which reactants are in different phases (solid, liquid, or gaseous). For the better part of a century it was thought that oscillations in homogeneous reactions, in which reactants are in the same phase, were not possible.

The first report of a periodic reaction in a *homogeneous* solution was made in 1921 by Bray [**53**], and followed up with his student Liebhafsky in 1931 [**54**]. They described the reaction of iodate, iodine, and hydrogen peroxide: the hydrogen peroxide decomposes into oxygen and water. The rate of evolution of the concentrations of oxygen O_2 and iodine I_2 vary periodically [**53**, **54**]. Bray's conclusion, that the reaction in a homogeneous solution was indeed periodic, was believed to be false: chemists assumed that this periodicity was an artifact of some unreported inhomogeneity, like dust or bubbles [**49**, **50**]. His results were not believed until the 1970s, after the phenomenon of chemical oscillations was accepted [**55**].

The belief in the impossibility of oscillations in a homogeneous chemical reaction stemmed from a misinterpretation of how the oscillations occur. Specifically it was believed that these oscillations violate the second law of thermodynamics, that in an isolated system a process can only occur if it increases the total entropy of the system. In other words spontaneous chemical reactions can only occur if they decrease the free energy

of the system. It was thought that oscillations in a chemical reaction indicate that the reaction passes through its equilibrium point, and that as it oscillates, free energy is continually increasing and decreasing, violating the second law of thermodynamics. The flaw in this logic is that chemical oscillations are a far-from-equilibrium phenomenon and that at no point in a period of oscillation does an oscillatory reaction pass through equilibrium [**49**, **50**].

The scientific community finally became convinced that these oscillations are possible through work done on the Belousov-Zhabotinsky (B-Z) reaction. Belousov, a Russian chemist, came across chemical oscillations in 1950 while investigating an inorganic version of the Krebs cycle. The Krebs cycle, also known as the citric acid cycle, is a key metabolic process in cellular respiration that uses citric acid as an intermediary. He was studying a reaction mixture of bromate, citric acid, and ceric ions (Ce^{+4}). His expectation was that as the reaction progressed the solution would undergo a monotonic change from yellow to clear as the Ce^{+4} ions (which make the solution yellow) are reduced to Ce^{+3}. Instead of the anticipated monotonic transition, the solution periodically changed from yellow to clear to yellow again, indicating that at some point in the reaction Ce^{+3} is oxidized, losing an electron to become Ce^{+4}. Belousov noted that in an unstirred graduated cylinder the solution showed yellow traveling waves. He submitted his results for publication in 1951 but they were rejected - skeptics believed that the oscillations violated the second law of thermodynamics. He finally published them in unrefereed conference proceedings [**49**,**50**].

Beginning a decade later, Zhabotinsky picked up where Belousov left off. He replaced the citric acid with malonic acid, which has become the standard B-Z reagent [**49**]. The use of a different redox indicator that doubles as a catalyst allowed him (with Zaikin) to

study unstirred solutions in thin layers [**49**,**56**]. Zaikin and Zhabotinsky then found spatial concentration waves in a thin layer, experimentally demonstrating spatial order in addition to temporal order in the B-Z reaction [**56**]. Fig.2.1 shows the experiment, snapshots taken one minute apart. Initially the catalyst is completely reduced (1); the subsequent snapshots show oxidation beginning at certain points called 'leading centers,' from which circular oxidation waves propagate. The interaction between different concentration waves depends on the frequency of the leading centers from which the concentration waves originate. Eventually fronts break and spatial disorganization takes place (snapshots 12-16) as the reaction reaches equilibrium. Thus, Zaikin and Zhabotinsky demonstrated experimentally the spontaneous appearance of temporal and spatial order, in the form of travelling waves, in a homogeneous system using the B-Z reaction [**56**].

A new theory was required to apply thermodynamics to systems far from equilibrium, which became non-equilibrium thermodynamics. Among those involved in the development of this theory was Prigogine and his group in Brussels who focused on chemical systems, working concurrently with Zhabotinsky's group in the USSR. They pointed out that a system could organize (which would decrease its entropy) so long as the net entropy of the universe increases monotonically. In a chemical system, the concentrations of intermediate reactants could oscillate as the overall entropy is increased by the conversion of high-energy reactants into low-energy products [**50**]. Oscillations in a closed system are a transient behavior in the reaction's approach to equilibrium.

Prigogine and his group demonstrated that oscillations can be sustained in a dissipative chemical system if the system is open and kept in its non-equilibrium state by feeding the system with reagents and removing the waste products of any chemical reaction [**57**, **58**].

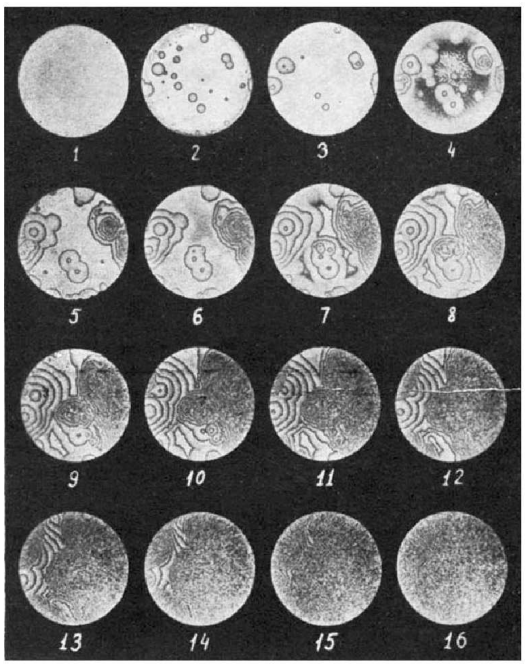

Figure 2.1. Concentration wave propagation in a two-dimensional self-oscillatory chemical system, the B-Z reaction [**56**]. Ring diameter 10cm, snapshots taken 1 minute apart. Experimental conditions in [**56**]. Figure reprinted from [**56**] by permission from MacMillan Publishers Ltd.

The group developed the first chemically plausible mechanism for oscillating reactions, the 'Brusselator' [**58**], first presented in 1968. Subsequently Field, Körös, and Noyes developed a mechanism describing the Belousov-Zhabotinsky in the early 1970s by combining kinetic and thermodynamic approaches. They later presented a simplified version, isolating a few key components, called the 'Oregonator.' This mechanism is commonly used to describe oscillatory reactions [**49**, **59**, **60**].

In 1972, Winfree published his results concerning the breakup of the circular propagation waves observed by Zaikin and Zhabotinsky [**61**]. Winfree modified Zaikin and Zhabotinsky's reagents to suppress bulk oscillation while retaining propagation excitability in order to isolate propagation fronts and study the emergence of spiral waves. He

then induced spiral waves by tipping the thin-layer reaction dish which results in fluid flow in the reacting solution. A flow component parallel to the wave front has no effect, but inducing a flow component perpendicular to the wave front mixes phases. As a result segments of the wave front disappear, and each free end becomes a center around which each remaining concentration wave propagates, winding into spirals. Winfree went on to use geometric arguments to describe these spirals and show that wave breakup results in the appearance of pairs of spiral waves and that the spiral waves persist eventually to the exclusion of all concentric ring waves.

In spite of its shaky beginnings, early research in chemical oscillations and nonlinear chemical dynamics yielded interesting results and spurred the development of non-equilibrium thermodynamics. For his work in that development, Prigogine was awarded the Nobel prize in chemistry in 1977, and for discovering chemical oscillations in the reaction that bears their names, Belousov and Zhabotinsky were awarded the order of Lenin in 1980 (though the latter was sadly after Belousov's death in 1970).

2.2. Turing regime - periodic structures

Pattern formation in non-equilibrium systems and, in particular, chemical systems, has quickly become a field of considerable interest and work. For reviews see [**3**, **51**]. Essentially all chemical systems are reaction-diffusion systems; in this section we discuss a pattern-forming instability particular to reaction-diffusion systems: the Turing instability. Through this instability, spatially-periodic patterns arise from a spatially homogeneous state. In contrast to the spatio-temporal target wave [**56**] and spiral [**61**] patterns described above, the spatially-periodic patterns that arise from a Turing instability are

stationary. Experimental results presented in this section were obtained far away from any Hopf bifurcation.

2.2.1. The Turing instability

Turing published "The chemical basis of morphogenesis" in 1952 [**62**], describing the possibility to create ('genesis') shapes ('morfi') in a homogeneous mixture of chemical reactants. Turing proposed that homogeneity in such a mixture may, when some parameter threshold is crossed, become unstable to stationary spatially-periodic patterns in the concentration of the reactants. The instability is described in the context of a system of reaction-diffusion equations, which describe the chemical reactions. For N chemical species with concentrations x_i these equations take the form

$$\frac{\partial x_i}{\partial t} = F_i(\mathbf{x}) + D_i \nabla^2 x_i, \qquad i = 1, ..., N. \tag{2.1}$$

The reactions are given by $F_i(\mathbf{x})$, and the D_i denote the diffusion coefficients.

In terms of the chemical kinetics, the reactions involve inhibitory processes and activator species. The diffusion of the different reactants must be such that the inhibitory effects are transported over a larger spatial region than the activator effects. This allows for local growth through the activator mechanism, whose spread is limited by the overall inhibitor processes, leading to stationary spatial structures [**49**, **50**, **62**, **63**]. Note that it is difficult to attain a regime where the diffusion coefficients of the activator and inhibitor species differ sufficiently in an aqueous solution; for example, computations on the B-Z reaction predict pattern formation through a Turing instability only in an unphysical regime [**64**].

2.2.2. Early experimental results

The first experimentally-obtained Turing structures were reported in a chemical reaction, in 1990 by De Kepper's group in Castets et al [**64**]. The chemical reaction that they used was the chlorite-iodide-malonic acid (CIMA) reaction, first proposed by De Kepper et al. in 1982 [**65**], in a gel. A gel was used because it binds key species and thus creates the necessary difference in effective diffusion coefficients [**49**, **66**] for the Turing instability to give rise to spatially periodic structures. The gel reactor is fed by reservoirs of reactants to keep the reaction from reaching its equilibrium state (to see the experimental set up see Fig.2.2a) and the control parameter is the concentration of those different reactants. Initially they observed a stripe pattern. The stripe pattern could be a Turing structure, or it could be an artifact of the experimental set up as the stripe orientation respects the symmetry imposed by the feeding reservoirs. However they showed for a well-defined range of the malonic-acid concentration in one of the reservoirs, the stripe patterns break up into spots, see Fig.2.2c. This breakup constitutes a symmetry breaking phenomenon, transverse to the imposed gradient. They observed that the experimentally-obtained pattern seemed to be indefinitely sustainable and the wavelength seemed to be based on properties of the reaction, rather than being based on strictly geometric properties of the experimental setup. Castets et al supported their result with the remark that similar lines of spots parallel to the main front were found in numerical studies of the Brusselator. This in combination with the spontaneous symmetry breaking, stationary nature, and intrinsic wavelength of the experimentally-obtained patterns strongly support the interpretation of these results as the first Turing structures [**49**, **64**]. The following year, Ouyang and Swinney reported more intricate Turing patterns in the CIMA reaction [**67**]. By varying

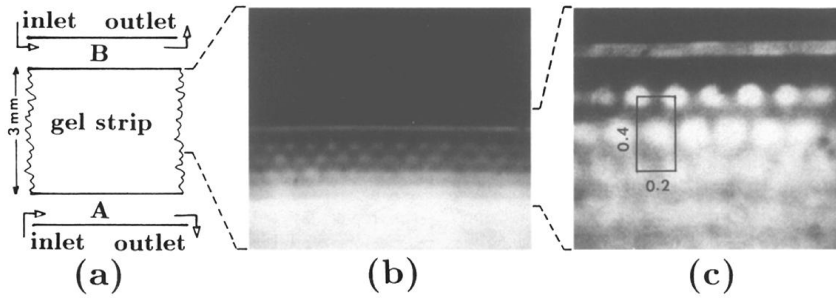

Figure 2.2. The first experimentally-obtained Turing structures: a sustained chemical pattern in a gel strip reactor [**64**]. (a) Sketch of the reactor: gel strip is squeezed between flat plates 1mm apart, reactants fed through the well-mixed reservoirs A and B. (b) Snapshot of the reactor, clear and dark regions represent different reaction states. (c) Zoom into region with Turing pattern. Experimental conditions in [**64**]. Figure reprinted from [**64**] with permission. Copyright ©1990 by the American Physical Society.

both temperature and reactant concentration they showed stable stripe, hexagon, and mixed patterns arising from a homogeneous state. For a snapshot of the results see Fig.2.3. Again they show an intrinsic pattern wavelength, spontaneous symmetry-breaking, and stationary nature of the patterns. Their experiments also show good qualitative agreement with numerical simulations of the Brusselator and other two-species reaction-diffusion models [**67**].

In 1991, Lengyel and Epstein developed a model of Turing structures in the CIMA reaction [**66**], a system of reaction-diffusion equations now called the Lengyel-Epstein equations. A variant of the model to include the effects of illumination was presented in 1999 [**68**]. These are often used to study Turing structures in both the CIMA reaction and the chlorine dioxide-iodine-malonic acid (CDIMA) reaction. The CDIMA reaction was derived from the CIMA by Lengyel and Epstein [**69**], who observed that in the CIMA reaction the chlorite and iodide ions are quickly consumed and that the major species are

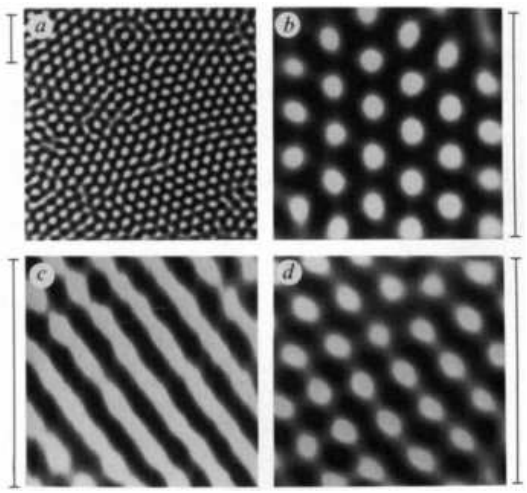

Figure 2.3. Chemical Turing patterns in a continuously-fed CIMA reaction [**67**]. (a),(b) Hexagon patterns. (c) Stripe pattern. (d) Mixed state. Bar next to each snapshot represent 1mm; reactor diameter is 25mm. Other experimental conditions in [**67**]. Figure reprinted from [**67**] by permission from MacMillan Publishers Ltd.

chlorine dioxide, iodine, and malonic acid. These then are the principle reactants used in the CDIMA reaction.

2.2.3. Superlattice patterns in the CDIMA reaction

In 1999, Muñuzuri et al. reported that the dynamics of the CDIMA reaction can be controlled by visible light [**70**]. Specifically they noted that visible light suppresses oscillations and shifts the steady state to a lower concentration iodide ions, of one of the principle reactants. They proposed a mechanism explaining this effect (cf. [**70**]). Technically speaking, the concentrations of atomic iodine and chlorite increase through photodissociation of molecular iodine - which initiates a redox reaction, reducing chlorine dioxide to chlorite and oxidizing iodine ions to atomic iodine. The change in concentrations with illumination intensity gradually decreases the amplitude of oscillations (conditions are

such that the reaction is closer to the Hopf bifurcation) until, with large enough intensity, the oscillations stop altogether (conditions are such that the reaction is below the Hopf bifurcation). Muñuzuri et al. went on to suggest that illumination may be employed to control Turing structures in experiments. Then Horváth et al. showed that spatially uniform illumination of Turing structures (that arose without illumination, controlled by other experimental constraints like temperature) affects the pattern characteristics [**68**].

In particular, they showed that large intensity light could in fact suppress Turing structures, and that temporally periodic illumination more efficiently suppresses the Turing structures than temporally uniform oscillation with the same average light intensity. Fastest suppression was observed at frequencies near the natural frequency of the corresponding well-stirred system. Their numerical simulations of the L-E equations, modified to include illumination, showed good agreement with their experimental results. In 2001, again in the same group, Dolnik et al. demonstrated that spatially periodic, temporally constant illumination can be used to remove defects in pre-existing Turing structures. Their investigation focused on the role of illumination intensity and wavelength of the spatially periodic forcing on a hexagonal Turing structure, with defects. Ultimately they found through experiment and numerical simulation in the L-E equations that forcing at wavelengths slightly larger than the pattern is most effective at removing defects and producing an ordered symmetric hexagon pattern.

Motivated by these early results, the same group explored the possibility of stabilizing *superlattice* patterns using spatially periodic illumination [**30**, **71**]. Their approach was to apply spatially periodic illumination patterns with carefully chosen wavelengths and to compare their experimental results with numerical simulations using the L-E equations.

Some of their experimental results are shown in Fig.2.4. In a regime where, without

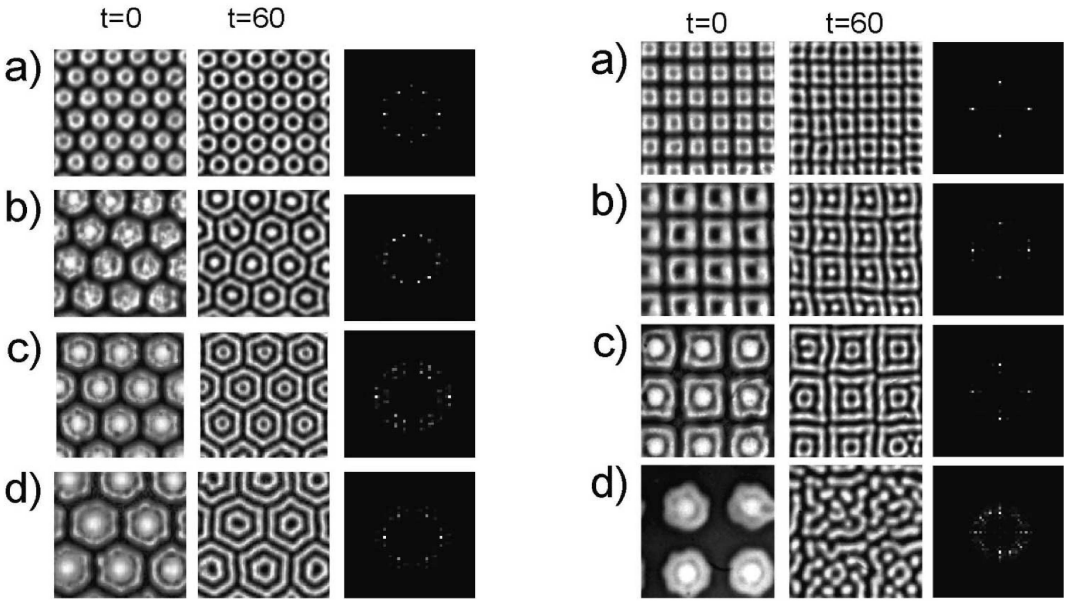

Figure 2.4. Experimental results, using spatially periodic illumination on the CDIMA reaction in a regime where the system without illumination exhibits labyrinthine patterns [**30**]. (I) Hexagonal superlattice patterns obtained using a mask with transparent circles in a hexagonal array; (a),(b),(c),(d) correspond to masks of different radii. (II) Square superlattice patterns obtained using a a mask with transparent circles in a square array; (a),(b),(c),(d) correspond to masks of different radii. In both (I) and (II), the first column shows the pattern after illumination is turned off, the second column shows the pattern 60 min later, and the third the Fourier transform of the pattern in the second column. Experimental conditions in [**30**]. Figures reprinted from [**30**] with permission. Copyright ©2003 by the American Physical Society.

illumination, labyrinthine patterns would arise, spatially periodic illumination of either a hexagonal or square pattern is imposed. The spatially periodic illumination was achieved by placing a mask, with circular holes arranged in either hexagonal or square alignments, between the reactor an the light source. The spatial period of the forcing imposed by the mask is an integer multiple of the spatial period of the unforced pattern. After

some time, the mask was removed (t=0 min in Fig.2.4). Subsequently the corresponding superlattice forms and persists for some time (t=60 min in Fig.2.4). They get good agreement with results from numerical simulations of the corresponding L-E equations. In this manner, [**30**,**71**] show superlattice Turing structures in a non-equilibrium chemical system, the CDIMA reaction.

2.3. Periodically Forced Oscillations

Zaikin and Zhabotinsky [**56**], and Winfree [**61**] noted interesting spatio-temporal dynamics in the B-Z reaction in the oscillatory regime. Coullet and Emilsson [**23**] used an analytic framework to study such non-equilibrium, spatially extended systems as a system of continuous, spatially distributed oscillators. They focused on the impact of strongly resonant forcing on symmetry-breaking and pattern formation and showed that forcing near one resonant frequency can lead to the formation of a variety of spatial patterns. Subsequent experiments, numerical simulations, and further analytic studies confirm the predictions made by Coullet and Emilsson.

They began by reviewing the unforced state and considered the case of oscillations in a steady system arising through a Hopf bifurcation, which breaks the time-translation symmetry. Near the onset of oscillations, measurable quantities, such as chemical concentrations C in the case of chemical oscillations, have time dependence of the form $C = C(Ae^{i\omega_0 t}, \bar{A}e^{-i\omega_0 t})$, where ω_0 is the frequency of oscillation and A represents the complex envelope of the oscillations. The original system possesses a time translation symmetry, with action on the amplitude $A \rightarrow Ae^{i\omega_0 \Delta t}$. Taking into account this action, which eliminates quadratic terms and most cubic terms, the normal form of the equation

for the amplitude of the envelope of oscillations A taken to cubic order is:

$$\frac{\partial A}{\partial t} = \mu A + (1 + i\beta)\nabla^2 A - (1 + i\alpha)A|A|^2. \tag{2.2}$$

Here the Laplacian ∇^2 is assumed to be on the same scale as the growth rate μ. Eq.(2.2) is called the complex Ginzburg-Landau equation (CGLE) and its derivation will be discussed in detail in Chapters 3 and 6. This equation admits the continuous family of spatially homogeneous, temporally periodic solutions of the form $A_0 = \sqrt{\mu}e^{-i\alpha\mu t + i\phi}$. Linear stability calculations show that for $1 + \alpha\beta > 0$ this solution is stable with respect to phase perturbations; defects result in spiral waves which can organize themselves in a cell-like structure. Fig.2.5(I) shows a zoomed-in snapshot of a single spiral within a cell-like structure in a B-Z reaction experiment. For $1 + \alpha\beta < 0$ the periodic solution is unstable to phase perturbations. This instability can lead to spatio-temporal turbulence characterized by the spontaneous appearance and annihilation of defect pairs.

Coullet and Emilsson discussed the impact of external spatially-uniform, temporally-periodic forcing with frequency $\omega_f = (n/m)(\omega_0 + \nu)$, for n/m an irreducible fraction and ν the detuning, in the spatially-extended oscillatory systems [**23**]. The forcing breaks the continuous time translation symmetry, and the resulting extended CGLE is

$$\frac{\partial A}{\partial t} = (\mu + i\nu)A + (1 + i\beta)\nabla^2 A - (1 + i\alpha)A|A|^2 + \gamma_n \bar{A}^{n-1}. \tag{2.3}$$

Here γ_n is proportional to $|f_n|^m$ with $|f_n|$ being the forcing strength. We have in mind the case $m = 1$ which because forcing with frequencies such that $m = 1$ has the strongest effect. By letting $A = R_0 e^{i\phi_0}$ and examining the stationary states of (2.3), they showed the existence of *frequency-locked* states: for n:1-frequency forcing the solution can lock

into one of n possible stationary phases, depending on the initial condition, separated by $2\pi/n$. Because it is the phase of the solution that becomes locked, these states are also commonly called phase-locked.

Phase-locked states can be obtained over a range of forcing frequencies and intensities, depending on particular system parameters; resonance regions form tongues in intensity-frequency space. In the two-dimensional case, captured experimentally by making the reactor a thin layer, many qualitatively different solutions, from irregularly-shaped domains or labyrinthine-like stripe patterns, are possible in the phase-locked regime. An example of the resulting phase-locked tongues experimentally obtained for a B-Z reaction in a thin layer is given in Fig.2.5(II); the tongues are similar to Arnol'd tongues, which describe resonance regions for a single oscillator [**72**, **73**], but also capture different spatial patterns. Pattern selection depends on system parameters and in particular on forcing intensities. Below we briefly discuss a few of the different patterns that can arise.

2.3.1. Forcing near 2:1 resonance: Bloch and Ising fronts

In general in the strong forcing limit $\gamma_n \gg \mu, \nu, \alpha, \beta$ in (2.3), spatially homogeneous phase-locked solutions are always linearly stable to amplitude perturbations and, for n:1 forcing with $n < 4$, have amplitude $R_0 \propto \gamma_n^{1/(4-n)}$ [**23**]. $n < 4$ corresponds to the strongly resonant forcing we have in mind; in the strong forcing limit with $n \geq 4$, the terms in (2.3) would scale differently, yielding a different spatially-homogeneous amplitude. For 2:1 forcing the two phase-locked states - associated with phases 0 and π - are separated by a stationary Ising front. Fig.2.6(I), left panel, shows an experimental snapshot of the B-Z reaction forced near 2:1 resonance, demonstrating two phase-locked states separated

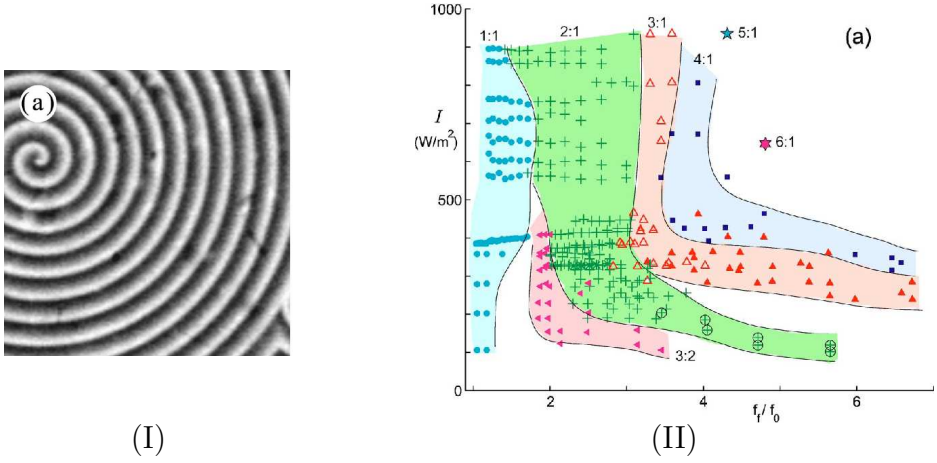

(I) (II)

Figure 2.5. (I) Experimentally-obtained spiral in unforced system [**73**]. (II) Largest $m:n$ phase-locking tongues in the phase-intensity (f_f/f_0-I) plane in the spatially-extended B-Z reaction with same system parameters as in (I) [**73**]. f_f is the forcing phase, f_0 the homogeneous frequency. System with parameters at points in each tongue respond subharmonically with the forcing frequency. Figures reprinted from [**73**] with permission. Copyright ©2004 by the American Physical Society.

by an Ising front. Along an Ising front the complex amplitude remains real as its phase jumps from 0 to π and vice-versa, as shown in the complex plane in Fig.2.6(I), right panel. Symmetry requires that this front is stationary. The velocity of the front connecting the state with phase 0 to the state with phase π is opposite and equal in magnitude to that of the reverse front from π to 0. Since the CGLE is equivariant under the reflection $A \to -A$, which transforms these two fronts into each other, they both must be stationary.

As the forcing strength γ_2 decreases from the strong forcing limit, while staying in the phase locking regime, a qualitatively different solution appears: near-resonant, rotating, 2-armed spirals [**23**], also observed experimentally [**73**]. Fig.2.7(I) shows snapshots of these solutions in experiment and their corresponding phase-space diagrams. This results

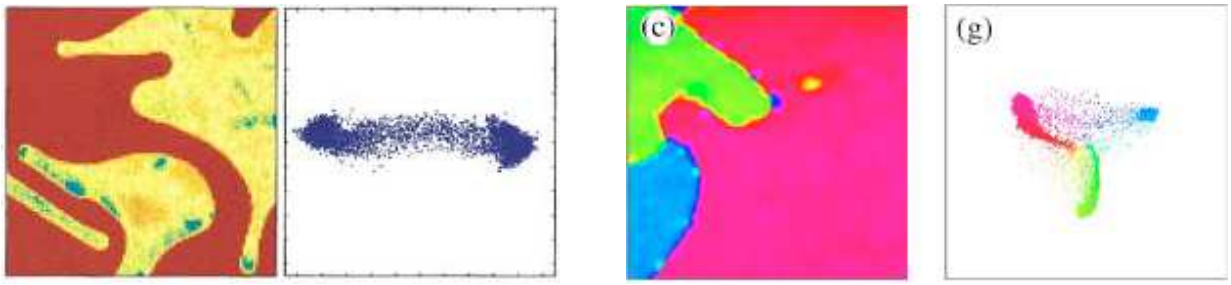

Figure 2.6. Standing wave patterns, phases phase-locked to the resonant forcing. Left panel: experiment snapshot. Right panel: complex plane; the complex amplitude of oscillations A is plotted in the complex plane for each pixel from camera data (which generated the snapshot). (I) With 2:1 resonant forcing [**72**], (II) with 3:1 resonant forcing [**73**]. (I) Figure reprinted from [**72**] with permission. Copyright ©2000 by the American Physical Society. (II) Figure reprinted from [**73**] with permission. Copyright ©2004 by the American Physical Society.

from a non-equilibrium Ising Bloch (NIB) bifurcation [**74**], through which a single stationary Ising front becomes unstable to Bloch fronts. The behaviour of the complex amplitude as its phase shifts between two different phase-locked domains changes through the NIB bifurcation. In the Ising regime above the NIB bifurcation point the complex amplitude remains real through the transition between phase-locked states; beyond the NIB bifurcation point the complex amplitude rotates in the complex plane as its phase changes, as shown in the complex plane in Fig.2.7(I). In this regime the Bloch wall between 0 and π domains breaks the chiral symmetry, as the change in complex amplitude associated with the phase shift between domains can now have two rotational directions, left or right. Bloch fronts of opposite chirality counter-propagate. Thus, the NIB bifurcation is a pitchfork bifurcation of a stationary Ising front to two counter-propagating Bloch fronts. When a two-dimensional Ising front becomes unstable to Bloch fronts, different sections can have opposite chirality. Their counter-propagating motion leads to the formation of

two-armed spiral, as shown in Fig.2.7(I) (see, for example, [**23**, **74**, **75**]). The two-armed spirals are called "near-resonant" solutions because they are travelling patterns [**73**].

2.3.2. n:1-resonant forcing for $n \geq 3$

For n odd, the parity symmetry $A \rightarrow -A$ is broken. Symmetry does not require then that the fronts between phase-locked states be stationary, so in general they are expected to be traveling. Low-intensity n:1-resonant forcing, within the phase-locked regime, results in near-resonant, rotating n-armed spirals [**23**], also observed experimentally [**73**]. Fig.2.7(II-V) shows snapshots of these solutions in experiment and their corresponding phase-space diagrams. As with the Bloch fronts the complex amplitude does not go through zero along the fronts connecting the different phase-locked states.

In experiments it has been observed that for stronger forcing the patterns are stationary or nearly stationary, in spite of the broken parity-symmetry which suggests that the fronts move. In this case the phase-locked states can form standing patterns in irregularly-shaped domains. Fig.2.6(II) shows an example of the B-Z reaction strongly forced near 3:1 resonance with three irregularly-shaped phase-locked phase states. The corresponding phase diagram shows the complex amplitude passing through zero between the phase states, which reflects the stationary character of the pattern (it is similar to the phase diagram for the Ising case). The experimentally-observed stationary patterns are not well understood, though it is thought the observed near-stationary patterns - propagating on a time scale orders of magnitude larger than the unforced spiral period - could evolve to other patterns such as large, slowly rotating, three-phase spiral waves [**28**], which can be understood using the CGLE.

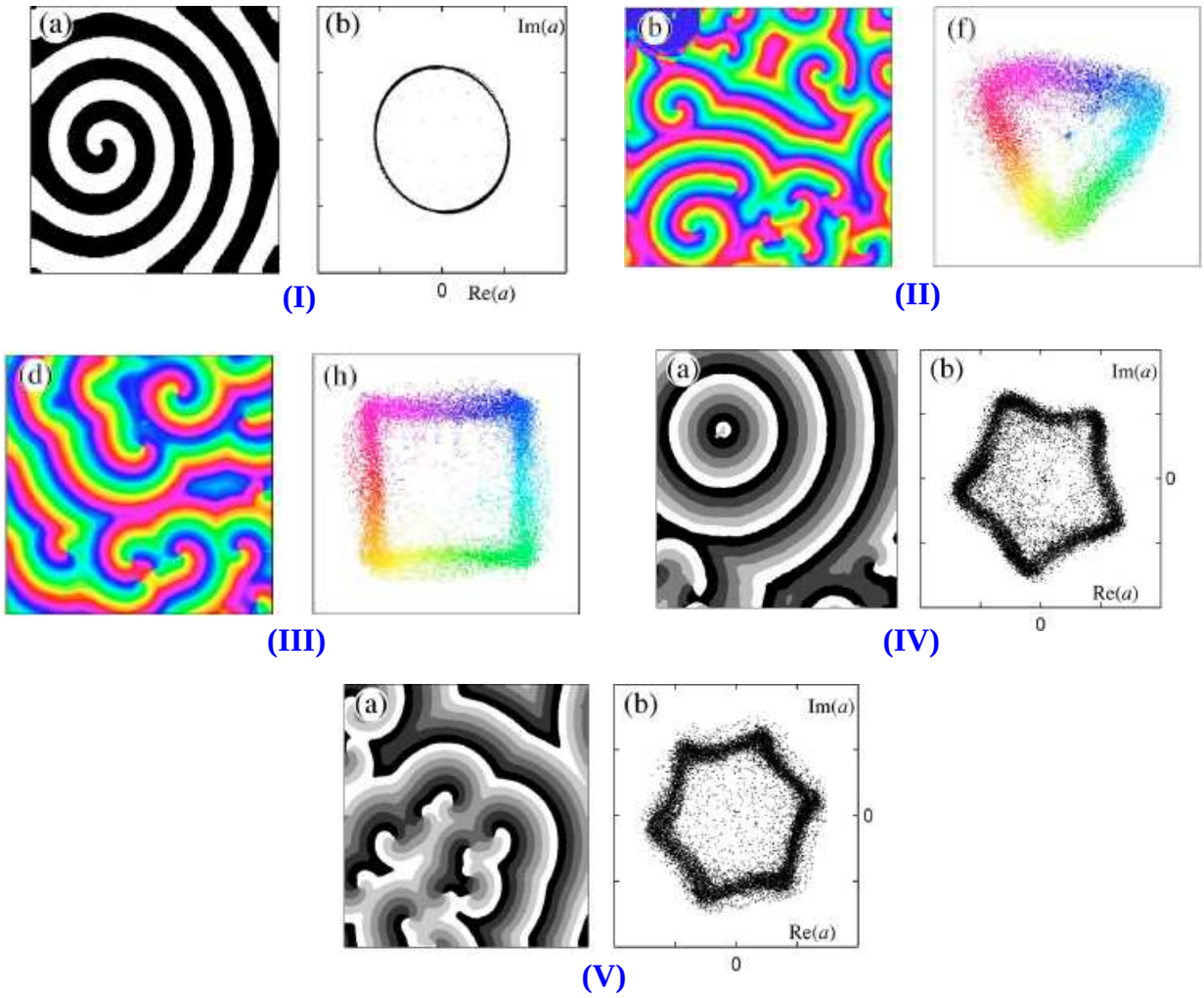

Figure 2.7. Near-resonant Bloch-front spiral waves in the B-Z reaction for different resonant forcings, [**73**]. All chemical parameters are the same as for the $m : n$ tongues given in Fig.2.5, unforced state is a spiral wave. Left: experiment snapshot. Right: complex plane; the complex amplitude of oscillations A is plotted in the complex plane for each pixel from camera data (which generated the snapshot). (I) With 2:1 resonant forcing, (II) with 3:1 resonant forcing, (II) with 4:1 resonant forcing, (III) with 4:1 resonant forcing, (IV) with 5:1 resonant forcing, and (V) with 6:1 resonant forcing. Figures reprinted from [**73**] with permission. Copyright ©2004 by the American Physical Society.

2.3.3. Interaction between forcing and the Benjamin-Feir instability

In [**23**] Coullet and Emilsson also discussed the interplay between the Benjamin-Feir instability, for $1+\alpha\beta < 0$, that results in defect mediated turbulence in the unforced case (2.2) and the stabilizing influence of the resonant forcing. Using a phase approximation they show that the competition between the phase instability and the forcing leads eventually to the formation of periodic structures such as stripes (in one or two dimensions) and hexagonal structures (in two dimensions). Specifically Coullet and Emilsson anticipated that, in two dimensions, as γ_n decreases the locked states become unstable to hexagons in a weakly transcritical bifurcation, and that there can also be a transition to stripe patterns and a 'turbulent' complex spatio-temporal state [**23**].

Stripe solutions under 1:1-resonant are investigated in [**76**, **77**]; using a phase approximation and the resulting phase equation they derive an analytic solution for the stripe state. They use the analytic solution to show that stripes arise through an instability of the homogeneous steady state through a supercritical bifurcation as the forcing strength γ_1 is decreased, and to understand stability boundaries of the homogeneous and stripe states.

The hexagons, stripes, and turbulence predicted by Coullet and Emilsson were found in a numerical simulation of the Brusselator with 2:1-resonant forcing by Zhang et al. in [**78**]; Fig.2.8 shows snapshots from these simulations. Interestingly to obtain the different states shown in Fig.2.8 they varied only the frequency across the 2:1-resonant tongue (see for example Fig.2.5), except for the case of turbulence, which was obtained by decreasing 2:1-forcing strength γ_2 so the simulation is outside of the phase-locking regime. Zhang et al. showed by reducing the Brusselator to a CGLE (2.3) for the oscillation amplitude

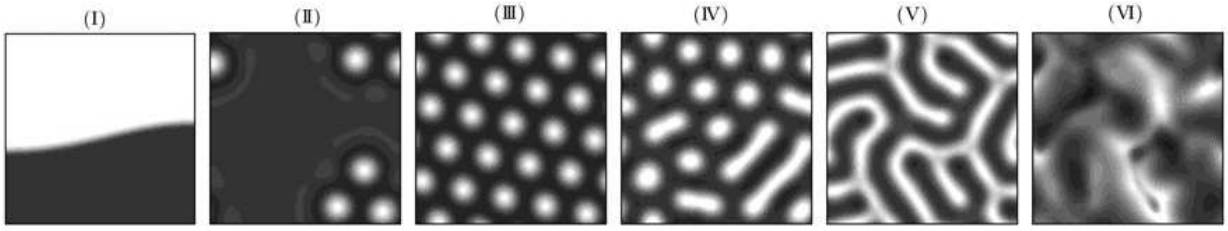

Figure 2.8. Numerical simulations of the Brusselator with forcing in the 2:1 resonant band [**78**] with parameters $a = 2$, $b = 5.3$, and $\gamma = 1.2$, showing pattern formation through interaction between the phase instability and external forcing as described in [**23**]. (I) Stationary Ising fronts for $\omega = 4.18$, (II) isolated hexagons for $\omega = 4.24$, (III) hexagon standing-wave pattern for $\omega = 4.28$, (IV) hexagon-stripe transition for $\omega = 4.34$, (V) labyrinthine standing-wave pattern for $\omega = 4.40$, and (VI) turbulent pattern for $\gamma = 0.3$ and $\omega = 4.40$. Figure reprinted with permission from the author.

that the hexagons arise from a dispersive instability [**24**] of non-zero, homogeneous steady states.

2.3.4. Other instabilities in the 2:1 resonant forcing regime

Petrov, Ouyang, and Swinney [**25**] showed a variety of spatial behaviors in the B-Z reaction when the oscillations are phase-locked with different m:n-resonant forcings, including an unforced spiral pattern coexisting with labyrinthine patterns in the 2:1-resonant forcing regime. The stability of the spiral pattern in the unforced state indicates that there is no Benjamin-Feir instability in the unforced system ($1+\alpha\beta > 0$) and that the stripe patterns creating the labyrinth do not arise from an instability due to the competition between the forcing and the phase instability, as described in the previous subsection. Instead they arise out of other mechanisms.

In the case of 2:1 resonant forcing two other pattern-forming mechanisms have been identified, through which a homogeneous oscillating state transforms to a standing-wave

labyrinthine pattern. Both occur near the boundary where phase-locked solutions become stable; Fig.2.9 shows the bifurcations in (γ_2, ν) parameter space, away from the NIB bifurcation line. The first mechanism is the transverse front instability which sets in at

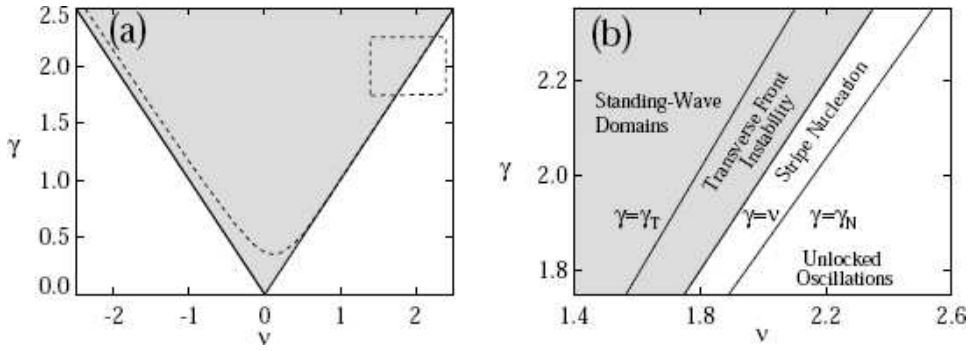

Figure 2.9. Parameter space diagram of (2.3) for $n = 2$ corresponding to 2:1 resonant forcing, with parameters $\mu = 1$, $\alpha = 0$, and $\beta = 0.5$ [**79**]. Note that in this plot γ corresponds to γ_2 in our notation. In (a) the solid line $\gamma = \nu$ represents the transition from unlocked oscillations ($\gamma < \nu$) to phase-locked states ($\gamma > \nu$), and the dashed line $\gamma = \gamma_{NIB}$ represents the transition from near-resonant Bloch fronts ($\nu < \gamma < \gamma_{NIB}$) to stationary Ising fronts ($\gamma = \gamma_{NIB}$). In (b), a close-up of the rectangular region in (a), shows regions of instabilities that lead to labyrinthine patterns. For $\gamma < \gamma_N$ the dominant pattern are unlocked oscillations, $\gamma_N < \gamma < \nu$ labyrinthine patterns arise from stripe nucleation (see Fig.2.10b), $\nu < \gamma < \gamma_T$ labyrinthine patterns arise from a transverse instability (see Fig.2.10a), and $\gamma > \gamma_T$ the dominant pattern is irregularly-shaped standing wave domains. The boundaries γ_{NIB} and γ_T were calculated numerically from the CGLE. Figures reprinted from [**79**] with permission. Copyright ©2002 Society for Industrial and Applied Mathematics.

$\gamma_2 = \gamma_T$, inside the phase-locking region ($\gamma_2 > \nu$) [**79**]. For $\gamma_2 > \gamma_T$ the Ising fronts are stable; for $\nu < \gamma < \gamma_T$ the Ising fronts are unstable to transverse perturbations. Perturbations along the front grow into fingers, which can change orientation and split. Fig.2.10a shows the development of a labyrinthine pattern due to this instability in a numerical simulation of the CGLE (2.3) [**79**]. A labyrinthine pattern can also arise through

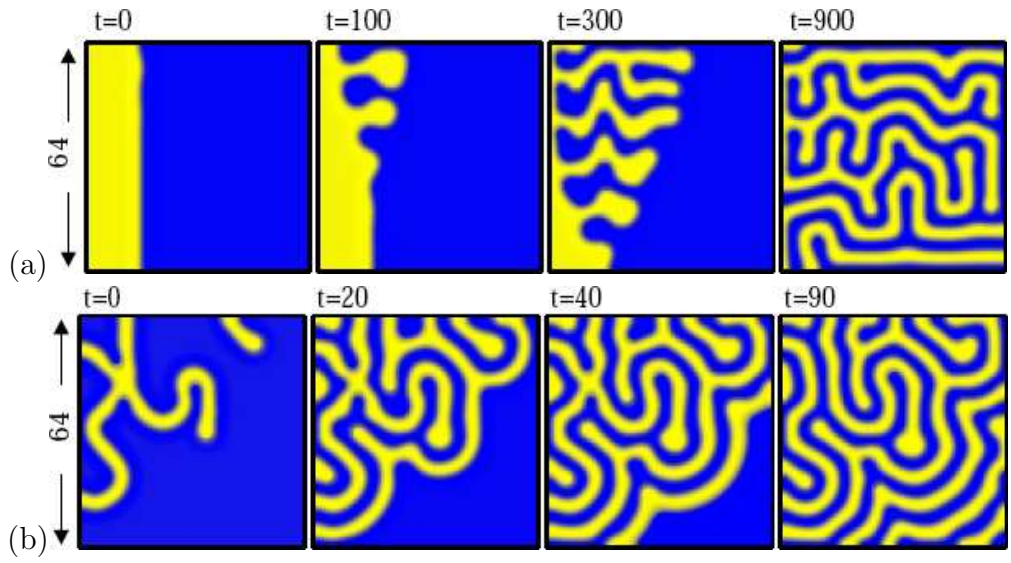

Figure 2.10. Eq.(2.3) for $n = 2$ corresponding to 2:1 resonant forcing, with parameters $\mu = 1$, $\alpha = 0$, $\beta = 0.5$, and $\nu = 2.0$ [**79**]. Blue and yellow regions represent phases separated by π (Ising fronts). (a) $\gamma = 2.02$ ($\nu < \gamma < \gamma_T$), labyrinthine pattern arising out of a transverse front instability. (b) $\gamma = 1.98$ ($\gamma_N < \gamma < \nu$), labyrinthine pattern arising from stripe nucleation. Figures reprinted from [**79**] with permission. Copyright ©2002 Society for Industrial and Applied Mathematics.

the nucleation of stripes in the regime of unlocked oscillations, below the phase-locking limit. Yochelis et al. in [**79**] showed that the stability of these labyrinthine patterns can be explained by the coupling of a oscillating, zero-wave number mode B_0, and a stationary, finite-wave number mode B_k in a Turing/Hopf bifurcation at $\gamma = \nu/\sqrt{1+\beta^2}$, below $\gamma = \nu$ where the phase-locked states become unstable to unlocked oscillations. The pure mode solutions (either $B_0 = 0$ or $B_k = 0$) are bistable near and below the $\gamma = \nu$ boundary. Thus the labyrinthine patterns can arise from the nucleation of stripes (see Fig.2.9b), γ_N computed numerically. Fig.2.10b shows snapshots from a numerical simulation of 2.3 demonstrating a labyrinthine pattern arising from the nucleation of stripes [**79**].

2.4. Conclusion

We have given an overview of the development of non-equilibrium thermodynamics and theory of dissipative systems in the context of nonlinear chemical oscillators. The development of the theory was spurred on by Belousov's initial experiments, Zaikin and Zhabotinsky's experiments showing concentric travelling waves [**56**], and Winfree's work on spiral patterns [**61**], in the B-Z reaction in a thin layer. These constitute the first experimentally-observed dissipative structures.

We reviewed the Turing instability [**62**] and spatially periodic patterns in oscillatory systems below the Hopf bifurcation, including the first experimental evidence of Turing structures in any system [**64**, **67**]. We also reviewed experimental and analytic results concerning oscillatory systems with single-frequency resonant forcing. Interaction between the forcing and the natural dynamics of the system causes a variety of symmetry-breaking bifurcations to a wealth of spatial patterns phase-locked to the forcing, including near-resonant Bloch spirals, labyrinthine patterns, and hexagon patterns [**67**, **73**, **79**]. We have discussed the Hopf and the Turing bifurcations separately. Additional richness is available through the interaction between the Hopf and Turing bifurcation [**51**].

In this dissertation we seek to stabilize complex stationary patterns like superlattice patterns and quasi-patterns in an oscillating system below, but near, the Hopf bifurcation. We model the system using the CGLE as described in Section 2.3 but consider $\mu < 0$ and apply resonant forcing near *multiple* resonant frequencies. The desired patterns arise in a bifurcation from a homogeneous, non-oscillating state. In Part 1 presented next we show our first efforts, forcing the system near twice and three times the Hopf frequency.

Part 1

Pattern selection in oscillatory systems with periodic resonant forcing

CHAPTER 3

The Complex Ginzburg-Landau Equation

We are interested in the formation of complex patterns in systems that undergo a Hopf bifurcation at vanishing wave number and that are forced at frequencies near integer multiples of the Hopf frequency ω. Near the Hopf bifurcation and for weak forcing such systems can be described by a suitably extended complex Ginzburg-Landau equation (CGLE), the form of which can be derived using symmetry arguments.

In the absence of forcing the complex amplitude $A(t)$ satisfies the usual CGLE,

$$\frac{\partial A}{\partial t} = a_2 A + a_3 \Delta A + a_4 A|A|^2, \tag{3.1}$$

where $a_i \in \mathbb{C}, i = 2 \ldots 4$ and $\Delta = \partial_{xx} + \partial_{yy}$ is the Laplacian in two dimensions [**21**]. The CGLE exhibits the normal-form symmetry $T_\tau : A \to A e^{i\omega\tau}$ reflecting the invariance of the original system under translations of the time $\tilde{t}$ by an arbitrary amount τ, $T_\tau : \tilde{t} \to \tilde{t} + \tau$. Here ω is the Hopf frequency. The slow time t is given by $t = \delta^2 \tilde{t}$ and the slow spatial scale is given by $(x, y) = \delta(\tilde{x}, \tilde{y})$, $0 < \delta \ll 1$.

The extension of the CGLE that describes strongly resonant multi-frequency forcing of the form $F = f_1 e^{i\omega\tilde{t}} + f_2 e^{2i\omega\tilde{t}} + f_3 e^{3i\omega\tilde{t}} + c.c.$ can be obtained by considering the multiple scale analysis [**80**] of the extended dynamical system in which the forcing amplitudes f_1, f_2, and f_3 are considered as dynamical variables that vary on the slow time scale t. Under time translations T_τ they transform as $f_1 \to f_1 e^{i\omega\tau}$, $f_2 \to f_2 e^{2i\omega\tau}$, $f_3 \to f_3 e^{3i\omega\tau}$ (e.g. [**81**]).

For general periodic time dependence of f_j the overall forcing is quasi-periodic. We focus here on choices for f_j corresponding to periodic forcing. To cubic order in A the most general equation that is equivariant under T_τ is then given by

$$\frac{\partial A}{\partial t} = a_1 + a_2 A + a_3 \Delta A + a_4 A|A|^2 + a_5 \bar{A} + a_6 \bar{A}^2. \tag{3.2}$$

To ensure all forcing terms appear in the leading order equation we employ the scaling $A(t) = O(\delta)$, $f_1 = O(\delta^3)$, $f_2 = O(\delta^2)$, and $f_3 = O(\delta)$. Then $a_1 = b_{11} f_1 + b_{12} \bar{f}_2 f_3$, $a_2 = b_{21} + b_{22}|f_3|^2$, $a_5 = b_{51} f_2$, $a_6 = b_{61} f_3$. The b_{ij} are O(1) complex coefficients. Spatial coordinates are scaled as $(x, y) = \delta(\tilde{x}, \tilde{y})$, where $(\tilde{x}, \tilde{y})$ are the original spatial coordinates of the system.

The forcing terms f_j satisfy decoupled evolution equations on their own. In the simplest case this evolution expresses a detuning ν_j of the forcing f_j from the respective resonance and the f_j satisfy

$$\frac{df_j}{dt} = i\nu_j f_j, \qquad j = 1 \ldots 3. \tag{3.3}$$

In general, the detuning introduces time dependence into (3.2).

We simplify (3.2) by absorbing the time dependence of f_2, $e^{i\nu_2 t}$, into A through the transformation $A \rightarrow A e^{i\nu_2 t/2}$. Further, we write $a_3 = 1 + i\beta$ by rescaling the spatial coordinates and $a_4 = -(1 + i\alpha)$ by rescaling A. We focus on the case of a supercritical Hopf bifurcation and choose the real part of a_4 to be negative. We now introduce a restriction on the forcing f_j to make the coefficients of the CGLE time-independent in order to simplify the analysis, at the expense of some generality. To remove the time dependence from the inhomogeneous term a_1 and the $\bar{A}^2$ term we choose the detuning of

the 1:1-forcing ν_1 to be half that of the 2:1-forcing, $\nu_1 = \nu_2/2$, and the detuning of the 3:1-forcing ν_3 to be three halves that of the 2:1-forcing, $\nu_3 = 3\nu_2/2$. This yields

$$\frac{\partial A}{\partial t} = (\mu + i\sigma)A + (1 + i\beta)\Delta A - (1 + i\alpha)A|A|^2 + \gamma\bar{A} + \eta\bar{A}^2 + \zeta. \tag{3.4}$$

Since f_3 is $O(\delta)$, both μ and σ are modified by the forcing function $|f_3|^2$. The coefficient σ is a linear function of the detuning ν_2, η is a complex linear function of $|f_3|$, and ζ is a complex linear function of $|f_1|$. The parameters ζ, γ, and η characterize the strength and phase of the forcing near 1:1, 2:1, and 3:1, respectively. Note that γ can be chosen real without loss of generality as the argument ϕ of γ can be absorbed into A through a transformation $A \to Ae^{i\phi/2}$ (modifying the phases of η and ζ). This is the extended version of the CGLE we will use in the next chapter to study pattern selection in a forced Hopf bifurcation. In this dissertation we stay below the Hopf bifurcation and focus on the case $\mu < 0$. Without forcing there are then no oscillations; the only solution is the basic state $A = 0$ as in the Faraday system.

CHAPTER 4

Pattern Selection

In this chapter we investigate spatial patterns in a forced Hopf bifurcation induced by forcing near twice and three times the Hopf frequency ω. As is apparent from (3.4), the forced Hopf bifurcation is described by an equation that is very similar to a two-component reaction-diffusion equation. The only and significant difference is the term involving β which characterizes the dispersion of unforced traveling wave solutions, which would be absent in the reaction-diffusion context. It plays, however, an essential role in exciting patterns with a characteristic wavenumber [**24**] and cannot be omitted. Pattern selection in a general two-component reaction-diffusion system has been studied in detail by Judd and Silber [**82**], who find that in principle not only stripe and hexagon patterns can be stable in such systems, but also super-square and super-hexagon patterns. They show that despite the large number of parameters characterizing these systems surprisingly few, very special combinations of the parameters enter the equations determining the pattern selection. We show an identical parameter collapse in the CGLE (3.4) motivating our use of the special combinations to study pattern selection in a system undergoing a Hopf bifurcation to spatially homogeneous oscillations, forced near twice and three times the Hopf frequency ω. We remind the reader that in this investigation we stay below the Hopf bifurcation taking $\mu < 0$. Thus, as in Faraday systems, in the absence of forcing, no oscillations arise.

4.1. Amplitude Equations

To investigate the weakly nonlinear stable standing wave patterns possible in (3.4) we derive amplitude equations for spatially periodic planforms. The linear stability of the state $A = 0$ is easily obtained by splitting the equation and the amplitude A into real and imaginary parts ($A \equiv A_r + iA_i$). The usual Fourier ansatz $A_{r,i} \propto e^{ikx}$ yields then the neutral stability curve $\gamma_n(k)$ with the basic state being unstable for $\gamma > \gamma_n(k)$. The minimum $\gamma_c(k)$ of the neutral curve is found to be at $k_c^2 = (\mu + \nu\beta)/(1 + \beta^2)$, $\gamma_c^2 = (\nu - \mu\beta)^2/(1 + \beta^2)$. Since $\mu < 0$, the condition $k_c^2 > 0$ implies that spatial patterns arise only if the detuning of the forcing relative to the Hopf frequency is such that waves with non-zero k are closer to resonance than homogeneous oscillations with $k = 0$ [**24**]. A typical neutral curve is illustrated in Fig.4.1 for $\mu = -1$, $\nu = 4$, $\beta = 3$ and $\zeta = 0$. The weakly nonlinear analysis presented in this paper is valid for values of γ near γ_c. An upper bound for the range of validity is given by $\gamma_n(k = 0)$ where spatially homogeneous oscillations are excited by the forcing, which interact with the standing-wave modes with wavenumber k_c.

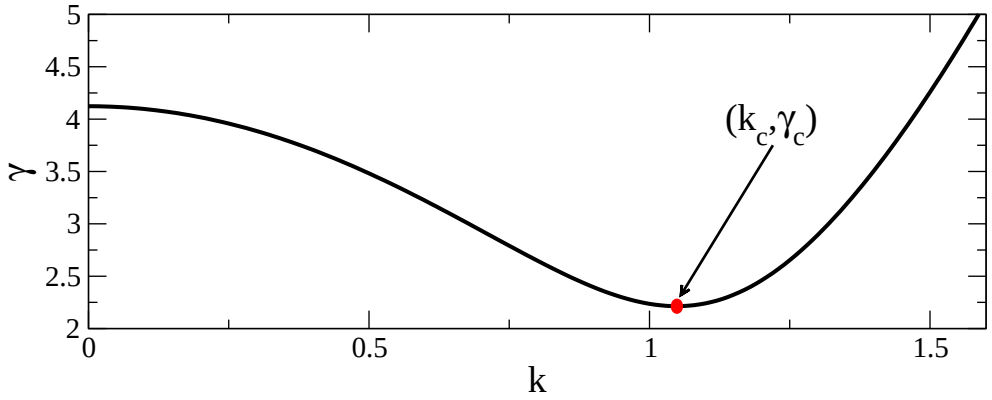

Figure 4.1. Neutral stability curve for (3.4) with $\mu = -1$, $\beta = 3$, $\nu = 4$ and $\zeta = 0$, resulting in $k_c = \sqrt{11/10}$, $\gamma_c = 7/\sqrt{10}$.

To determine the stability of the various planforms we first determine the amplitude equations for rectangle patterns, which are comprised of two modes separated by an angle θ in Fourier space. We expand (A_r, A_i) as

$$\begin{pmatrix} A_r \\ A_i \end{pmatrix} = \epsilon \sum_{j=1,\theta} Z_j(T) e^{i\mathbf{k}_j \cdot \mathbf{r}} \begin{pmatrix} v_1 \\ v_2 \end{pmatrix} + c.c. + \mathcal{O}(\epsilon^2), \tag{4.1}$$

where $0 < \epsilon \ll 1$ and the complex amplitudes $Z_1(T)$ and $Z_\theta(T)$ depend on the slow time $T = \epsilon^2 t$. The wave vectors are given by $\mathbf{k_1} = (k_c, 0)$ and $\mathbf{k}_\theta = (k_c \cos(\theta), k_c \sin(\theta))$. We also expand γ as $\gamma = \gamma_c + \epsilon^2 \gamma_2$. The eigenvector $\mathbf{v} = (v_1, v_2)^T$ is normalized so that $\|\mathbf{v}\|_2 = 1$.

The usual expansion leads to the amplitude equations for (Z_1, Z_θ),

$$\frac{dZ_1}{dT} = \lambda(\gamma - \gamma_c) Z_1 - \left(b_0 |Z_1|^2 + b_1(\theta) |Z_\theta|^2\right) Z_1, \tag{4.2}$$

$$\frac{dZ_\theta}{dT} = \lambda(\gamma - \gamma_c) Z_\theta - \left(b_1(\theta) |Z_1|^2 + b_0 |Z_\theta|^2\right) Z_\theta. \tag{4.3}$$

If $\theta = \frac{n\pi}{3}$, $n \in \mathbb{Z}$, the quadratic nonlinearity induces a secular term and the expansion has to include three modes rotated by 120° relative to each other. The parameters can be chosen such that a single solvability condition arises at cubic order (cf.(4.4) below, with $Z_{4,5,6} = 0$).

More complex patterns can be described by combining these two analyses. For example, a super-hexagon pattern comprised of two hexagon patterns $\{Z_1, Z_2, Z_3\}$ and $\{Z_4, Z_5, Z_6\}$ that are rotated relative to each other by an angle θ_{SH} is described by the

amplitude equation

$$\begin{aligned}\frac{dZ_1}{dT} =&\lambda(\gamma-\gamma_c)Z_1+\sigma\bar{Z}_2\bar{Z}_3- \\ &-\left(b_0|Z_1|^2+b_2\left(|Z_2|^2+|Z_3|^2\right)\right)Z_1 \\ &-\sum_{j=0}^{2}b_1(\theta_{SH}+j\frac{2\pi}{3})|Z_{4+j}|^2Z_1 \end{aligned} \tag{4.4}$$

and corresponding equations for Z_j, $j=2,\ldots,6$. These patterns are periodic for a discrete set of angles θ_{SH} [**82**].

The coefficients of the amplitude equations can be written in a simple form, setting $\eta \equiv \eta_r + i\eta_i$:

$$\lambda = \frac{\sqrt{1+\beta^2}}{|\beta|}, \quad \sigma = \frac{2\sqrt{1+\beta^2}(a\eta_r+\eta_i)}{\beta\sqrt{1+a^2}}, \tag{4.5}$$

$$b_0 = 3\psi + \frac{76}{9}\chi, \quad b_2 = 6\psi + 10\chi + \phi, \tag{4.6}$$

$$b_1(\theta) = 6\psi + 8f(\theta)\chi, \tag{4.7}$$

with

$$\psi = 1-\frac{\alpha}{\beta}, \quad \chi = \frac{-\beta(\nu-\mu\beta)}{2(\mu+\nu\beta)}\sigma^2, \tag{4.8}$$

$$\phi = -\frac{2(1+\beta^2)}{a\beta(\nu-\mu\beta)}\left(2\sqrt{1+\beta^2}\eta_i^2 - \frac{(a+\beta)\eta_i}{\sqrt{1+a^2}}\sigma\right) \tag{4.9}$$

$$f(\theta) = \frac{3+16\cos^4\theta}{(4\cos^2\theta-1)^2}. \tag{4.10}$$

Here $a = \sqrt{1+\beta^2}+\beta$.

4.2. Pattern Selection

4.2.1. $\sigma = 0$ Regime

As shown by Judd and Silber [**82**] for general two-component reaction-diffusion systems, at the point of degeneracy at which the quadratic coefficient σ vanishes not only stripe patterns but also hexagon or triangle patterns can be stable. We show that this is also true in the CGLE. The conditions for hexagons (or triangles) to be stable are

$$\phi < 0, \quad -2\phi/15 < \psi < -\phi/3. \tag{4.11}$$

For $\psi > -2\phi/15$ the bifurcation to hexagons (triangles) is a supercritical pitchfork, while it is a subcritical pitchfork otherwise. For $\psi > -\phi/3$, the hexagons (triangles) are unstable to stripes. Whether hexagon or triangle patterns are stable depends on higher-order terms in the amplitude equations [**83**], which are not considered here.

Comparing the conditions (4.11) with expressions (4.8,4.9) shows that over a wide range of the system parameters α and β stripe or hexagon patterns can be made stable by a suitable choice of the forcing function. Specifically, (4.9) shows that ϕ is always negative at the degeneracy $\sigma = 0$ since $\beta(\nu - \mu\beta) > 0$, which follows from $\mu < 0$ and the condition $k_c^2 > 0$. The surfaces $\psi = -2\phi/15$ and $\psi = -\phi/3$ are shown in Fig.4.2 for $\mu = -1$, $\nu = -1$, and $\sigma = 0$. These results do not depend qualitatively on the choice of μ and ν as long as $\mu < 0$ and $k_c^2 > 0$. For experiments on the Belousov-Zhabotinsky reaction values for α and β have been reported near the point marked by the vertical line ($\alpha = 0.4$, $\beta = -1.4$) [**84**]. Thus forcing should provide a robust mechanism to induce transitions from stripes to supercritical and subcritical hexagons. A distinguishing feature of these

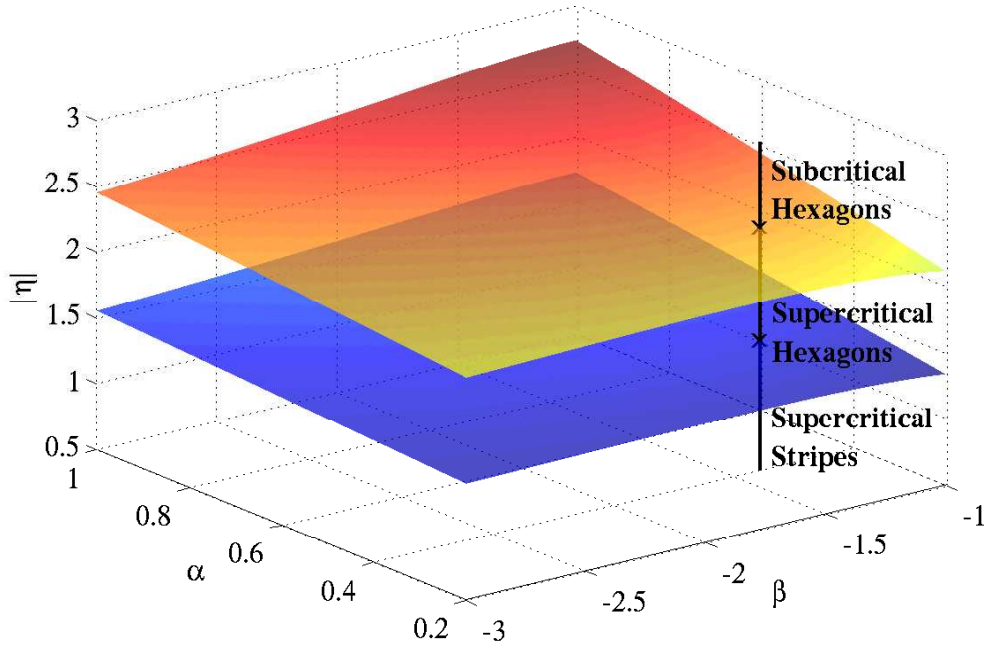

Figure 4.2. Surfaces $\psi = -2\phi/15$ and $\psi = -\phi/3$ for $\sigma = 0$, marking the boundaries of stability between supercritical stripes, supercritical hexagons, and subcritical hexagons, for system parameters α and β with $\mu = -1$, $\nu = -1$.

hexagon patterns is that both 'up'- and 'down'-hexagons are simultaneously stable and are likely to form competing domains. Fig.4.3 shows an example of the competition between 'up'- and 'down'-hexagons in a numerical simulation of (3.4).

4.2.2. $0 < |\sigma| \ll 1$ Regime

Unfolding the degeneracy, i.e. taking $0 < |\sigma| \ll 1$, the transition to hexagons becomes transcritical and hexagons are stable to stripes for a $\gamma-$range given by

$$\gamma_c - \frac{\sigma^2}{4\lambda(b_0 + 2b_2)} < \gamma < \gamma_c + \frac{\sigma^2(2b_0 + b_2)}{\lambda(b_2 - b_0)^2} \equiv \gamma_{HS}. \tag{4.12}$$

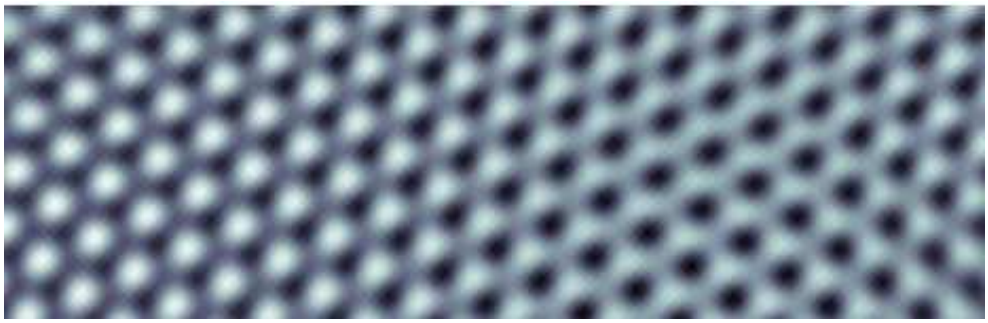

Figure 4.3. Competing domains of up- and down-hexagon domains obtained from random initial conditions with linear parameters as in Fig.4.1 and nonlinear parameters $\alpha = -1$, $\eta_r = 0.4$ and $\eta_i = -0.4(\sqrt{10}+3)$. η_r, η_i chosen so that $\sigma = 0$.

Note that $\gamma_{HS} > \gamma_c$, even if (4.11) are not satisfied, since stripes do not exist for $\gamma < \gamma_c$. The instability of hexagons at γ_{HS} only arises if $b_2 > b_0$, that is, if $3\psi + 14\chi/9 + \phi > 0$. With $\sigma \neq 0$ the up-down symmetry of the hexagon amplitude equations is broken and either up- or down-hexagons are preferred.

Turning to other planforms, Judd and Silber found that rectangular planforms cannot be stable at or near the degeneracy point [**82**]. Interestingly, however, they find that while super-hexagons cannot be stable at the degeneracy point, they can arise in a very small parameter regime in its vicinity if the conditions

$$\phi > 0, \quad -\phi/21 < \psi < \phi/3 \tag{4.13}$$

are met. They then can be bistable with hexagons. We find that in our system this is not the case within the cubic truncation (4.4). (4.9) shows that - for small $|\sigma|$ - ϕ can be made positive only by making η_i small as well ($\eta_i = \mathcal{O}(\sigma)$). Even then ϕ can only be slightly positive, $\phi = \mathcal{O}(\sigma)$, requiring that $\psi = \mathcal{O}(\sigma)$ in order to satisfy the second condition in

(4.13). Under these conditions all cubic coefficients in (4.6,4.7) would become of $\mathcal{O}(\sigma)$ and without knowledge of the next-order coefficients no stability predictions can be made.

4.2.3. $\sigma = \mathcal{O}(1)$ Regime

Often weakly nonlinear analysis gives qualitatively useful information beyond its formal regime of validity. We therefore also consider the case $\sigma = \mathcal{O}(1)$. Considering super-hexagons it should be noted that for $\sigma = \mathcal{O}(1)$ the inequalities (4.13) are not the correct stability conditions, since they were derived assuming $0 < \sigma \ll 1$ and so ignore the angle dependence of the cubic coefficients, which is $\mathcal{O}(\sigma)$. We use (4.13) therefore only as a guide to locate parameter regimes in which super-hexagons may be expected to be stable and then determine the eigenvalues that govern their stability directly from the linearization of (4.4) about the equal-amplitude solution $|Z_j| = |Z|$, $j = 1, \ldots, 6$. We find that indeed there are parameters for which all super-hexagon eigenvalues are negative, suggesting that super-hexagons are stable; for example, one such parameter set is given by the linear parameters used in Fig.4.1 with $\alpha = -1$ and $\eta = \sqrt{2}e^{i\pi/4}$. We will test this weakly nonlinear prediction through numerical simulation.

4.2.4. Numerical Simulation Results

Using direct numerical simulations of the forced complex Ginzburg-Landau equation (3.4) we have studied to what extent the predictions of the weakly nonlinear analysis are borne out. We employed a pseudo-spectral method with Crank-Nicolson-Adams-Bashforth time stepping, using periodic boundary conditions. We ran the simulations in a large system of linear size $L = 10(2\pi/k_c)$, representing 10 wavelengths. Because we are only interested in

the relative stability between hexagon and stripe patterns we used a rectangular grid such that $L_x = 2L$ and $L_y = 4L/\sqrt{3}$; thus, all participating modes lie exactly on the critical circle. Finally to capture higher order harmonics we used 64 modes and their complex conjugates in Fourier space, and for the purposes of accuracy we used a small time-step size $\Delta t = 0.001$.

In the degenerate case $\sigma = 0$, enforced by setting $\eta_i = -a\eta_r$, we find, as predicted, either stripes or hexagons to be stable depending on the values of α and $|\eta|$. To test the stability boundary $\psi = -\phi/3$ in (4.11) we vary the 3:1 forcing strength $|\eta|$ with the remaining parameters in (3.4) fixed at $\gamma = 2.25$ and $\alpha = 0$ and the linear parameters as given for Fig.4.1 and start the simulations with random initial conditions. The simulations agree with the weakly nonlinear prediction to within 5%. Fig.4.3 shows a typical hexagonal pattern obtained from random initial conditions exhibiting competing domains of up- and down-hexagons.

The stability limit $\psi = -2\phi/15$ in (4.11) marks the point at which the pitchfork bifurcation to hexagons becomes subcritical. Extracting the cubic coefficient $b_0 + 2b_2$ from transient hexagon patterns (cf. Fig.4.5 below) for varying values of $|\eta|$ with all other parameters as well as $\sigma = 0$ fixed we find agreement between the weakly nonlinear result and the simulations to within 1%. Fig.4.4 presents a bifurcation diagram in the supercritical regime but close to the tricritical point (ψ only slightly above $-2\phi/15$). While the weakly nonlinear analysis agrees very well in the immediate vicinity of the bifurcation point, the deviations become significant already for values of γ only 0.5% above γ_c. Most surprisingly, however, as γ is further increased the small-amplitude hexagons undergo a saddle-node bifurcation and in the simulations the solution jumps to large-amplitude

hexagons. Both small- and large-amplitude hexagons are simultaneously stable over a range in γ. With increasing $|\eta|$ the saddle-node bifurcation at which the large-amplitude hexagons come into existence is shifted towards smaller values of $\gamma < \gamma_c$. We have not investigated to what extent the existence of the large-amplitude hexagons depends on the parameters α and β of the unforced system.

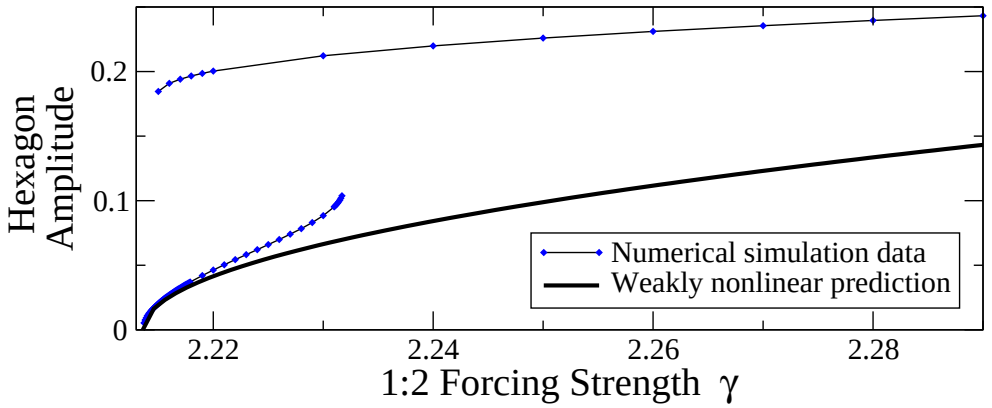

Figure 4.4. Numerically obtained hexagon amplitudes for linear parameters as in Fig.4.1 and nonlinear parameters $\alpha = 0$, $\eta_i = 2.38$ and $\eta_r = -2.38/(\sqrt{10}+3)$. η_r, η_i chosen so that $\sigma = 0$.

Away from the degeneracy, $\sigma = \mathcal{O}(1)$, the validity of the weakly nonlinear analysis can be severely restricted by the fact that the amplitudes of all stable branches are $\mathcal{O}(1)$, which formally suggests the significance of higher-order terms in the expansion. Indeed, in and near the parameter regimes for which the weakly nonlinear analysis predicts stable super-hexagon patterns we do not find any indication of their stability. To assess explicitly the significance of the higher-order terms in the amplitude equations for $\sigma = \mathcal{O}(1)$ we extract them directly from numerical simulations of transients for the case of hexagon patterns. Fig.4.5 shows for $\gamma = \gamma_c$ the numerically determined dependence of $|Z|^{-2}\, d|Z|/dt$ on the hexagon amplitude $|Z| = |Z_j|$, $j = 1, 2, 3$. For very small $|Z|$ it agrees well with the

weakly nonlinear result $\sigma - (b_0 + 2b_2)|Z|$, which yields the straight dashed line. However, even for $\gamma = \gamma_c$ the fixed point FP_3 obtained from the hexagon amplitude equations deviates from the numerically obtained fixed point FP_n by 30%. A fit of $|Z|^{-2}\, d|Z|/dt$ to a higher-order polynomial shows that in the amplitude equation the magnitude of the quartic and quintic terms reach values of 15% and of 20% of the cubic term, respectively. This supports our interpretation that in this regime the cubic amplitude equation does not allow quantitative predictions.

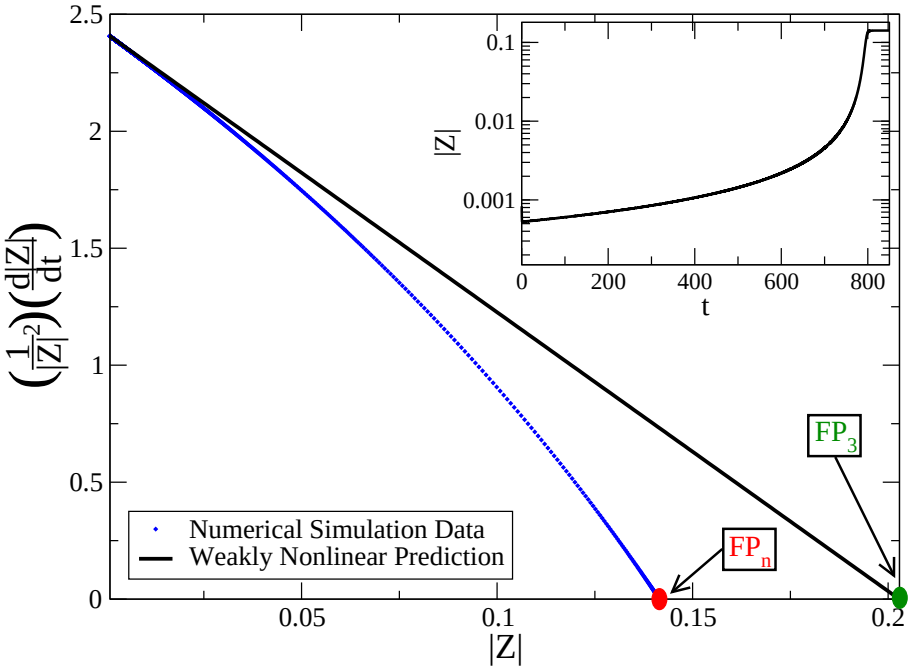

Figure 4.5. Extracting the nonlinear coefficients for hexagons from transients (inset) for $\mu = -1$, $\nu = 4$, $\beta = 3$, $\alpha = -1$, $\eta = \sqrt{2}e^{i\pi/4}$ (so $\sigma = 2.4187$). FP_n corresponds to the fixed point obtained from numerical simulation, FP_3 to that obtained from the weakly nonlinear calculation to cubic order.

CHAPTER 5

Conclusion for Part 1

We have investigated the regular spatial planforms that can be stably excited in a system undergoing a Hopf bifurcation by applying a periodic forcing function that resonates with the second and third harmonic of the Hopf frequency. We have done so within the weakly nonlinear regime by deriving from the complex Ginzburg-Landau equation (3.4) the appropriate amplitude equations describing the selection between various planforms. By tuning the phase of the forcing close to 3ω, three times the Hopf frequency, one can always reach the point of degeneracy at which no quadratic terms arise in the amplitude equations, despite the quadratic interaction in the underlying complex Ginzburg-Landau equation. Over a wide range of the parameters of the unforced system hexagon or stripe patterns can be stabilized depending on the forcing function. In the former case competing domains of up- and down-hexagons are found in numerical simulations when starting from random initial conditions. Hexagons can arise from either a supercritical or subcritical pitchfork bifurcation, which we have shown analytically and confirmed numerically. Moreover, numerical simulations have shown the existence of hexagons with much larger amplitude, which can be bistable with the supercritical hexagons.

Surprisingly, despite the extensive control afforded by the two forcing terms, no square, rectangle, or super-hexagon patterns are stable in the vicinity of the degeneracy $\sigma = 0$, irrespective of the parameters of the unforced system. While in the regime in which

hexagons arise in a strongly transcritical bifurcation the weakly nonlinear theory suggests the possibility of stable super-hexagons, direct numerical simulations of the complex Ginzburg-Landau equation indicate no such stability and we show that terms of higher order in the amplitudes are relevant.

By introducing a further forcing frequency, which is also close to the 2:1-resonance, the transcritical bifurcation to hexagons can be avoided. As we show in a the next part, the corresponding, more elaborate weakly nonlinear theory correctly predicts stable quasi-patterns comprised of four, five, or more modes.

Part 2

Pattern selection in oscillatory systems with modulated resonant forcing

CHAPTER 6

The Complex Ginzburg-Landau Equation

In Chapter 4 and in [**46**] we investigated the extended CGLE (3.4) with constant coefficients, made time-independent by the transformation $A \to Ae^{i\nu_2 t/2}$. For that case we found that the possibly stable superhexagon pattern, a superlattice pattern, arises in a transcritical bifurcation. We showed that the amplitudes on the upper branch of the transcritical bifurcation are $O(1)$ and that therefore a weakly nonlinear analysis taken to cubic order is insufficient to describe these patterns. The bifurcation is transcritical because the quadratic term in the CGLE introduces also a quadratic term in the amplitude equations describing the competing Fourier modes. To eliminate the latter quadratic term without losing the resonant triad interaction we choose in the following the forcing near twice the Hopf frequency to be quasi-periodic,

$$f_2 = f_{21} + f_{22} \qquad \text{with} \qquad \frac{df_{21}}{dt} = i\nu_{21} f_{21}, \quad \frac{df_{22}}{dt} = i\nu_{22} f_{22}. \tag{6.1}$$

The difference between the two detunings ν_{21} and ν_{22} introduces then a periodic time dependence in (3.2). To obtain the desired patterns, we exploit the spatio-temporal resonances induced by the time dependence and focus on patterns that are subharmonic in time. The quadratic interaction of two subharmonic modes induces a harmonic mode and does not generate a quadratic term in the amplitude equation for the subharmonic mode. Consequently, we expect a pitchfork bifurcation.

Considering the quasi-periodic forcing (6.1) we simplify (3.2) by absorbing the time dependence of f_{21}, $e^{i\nu_{21}t}$, into A through the transformation $A \to Ae^{i\nu_{21}t/2}$. Further, we write $a_3 = 1 + i\beta$ by rescaling the spatial coordinates and $a_4 = -(1 + i\alpha)$ by rescaling A. We focus on the case of a supercritical Hopf bifurcation and choose the real part of a_4 to be negative. We now introduce restrictions on the forcing f_j for the purpose of making the analysis manageable at the expense of some generality. To eliminate the inhomogeneous term a_1 we choose $b_{11}f_1 = -b_{12}(\bar{f}_{21} + \bar{f}_{22})f_3$. To remove the time dependence from the $\bar{A}^2$ term we choose $\nu_3 = 3\nu_{21}/2$. This yields

$$\frac{\partial A}{\partial t} = (\mu + i\sigma)A + (1 + i\beta)\Delta A - (1 + i\alpha)A|A|^2 + (\gamma_1 + \gamma_2 e^{i(\nu_{22}-\nu_{21})t})\bar{A} + \eta\bar{A}^2. \quad (6.2)$$

Here again, as in Chapter 3, since f_3 is $O(\delta)$, both μ and σ are modified by the forcing function $|f_3|^2$, the coefficient σ is a linear function of the detuning ν_{21}, and η is a complex linear function of $|f_3|$. We rewrite η in magnitude and phase, $\eta = \rho e^{i\Phi}$, and write $\gamma_1 = \gamma\cos(\chi)$ and $\gamma_2 = \gamma\sin(\chi)$ with χ characterizing the relative forcing strengths. Finally we set $\nu \equiv \nu_{22} - \nu_{21}$, to get the version of the complex Ginzburg-Landau equation (CGLE) that we will investigate in the rest of this dissertation,

$$\frac{\partial A}{\partial t} = (\mu + i\sigma)A + (1 + i\beta)\Delta A - (1 + i\alpha)A|A|^2 + \gamma\left(\cos(\chi) + \sin(\chi)e^{i\nu t}\right)\bar{A} + \rho e^{i\Phi}\bar{A}^2. \quad (6.3)$$

In the appendix we show that this same equation can be derived directly from a model of chemical oscillations, the Brusselator.

We remind the reader that we stay below the Hopf bifurcation and focus on the case $\mu < 0$. Again as in Chapter 3, and similarly to the Faraday case, in the absence of forcing, the only solution is then the basic state $A = 0$.

CHAPTER 7

Linear Stability Analysis

In order to study the onset of complex patterns in the vicinity of a forced Hopf bifurcation described by Eq.(6.3), we begin by examining the linear stability of the $A = 0$ solution. In contrast to Eq.(3.4) studied in Chapter 4, Eq.(6.3) has a periodic, time-dependent coefficient with frequency ν. Therefore, we use Floquet theory [**85**] to identify values of the forcing γ and corresponding wave number k for the onset of oscillating standing waves that oscillate harmonically (with period $2\pi/\nu$) and subharmonically (with period $4\pi/\nu$).

Our goal is to find neutral stability curves such that the primary instability is subharmonic with wave number $k_c^{(S)}$ and a harmonic mode with wave number $k_c^{(H)}$ is weakly damped such that $k_c^{(H)}/k_c^{(S)} = K$ for a given K. We will exploit this regime through resonant three-wave interaction [**37**, **42**] to stabilize complex patterns in Chapter 8.

7.1. Neutral Stability Curves

To obtain the onset of standing waves that are phase-locked to the driving we consider the stability of the solution $A = 0$ of (6.3) [**24**]. As in Section 4.1 we split (6.3) into the real and imaginary parts by setting $A = A_r + iA_i$ and linearize about $(A_r, A_i) = (0, 0)$ to obtain linear partial differential equations for A_r and A_i. In this case, however, the equations are time-periodic with period $2\pi/\nu$, so we use Floquet theory in the same way

as described in [**86**]. The solutions to the linear problem in Floquet form are

$$\begin{pmatrix} A_r \\ A_i \end{pmatrix} = e^{(\hat{\delta}+i\hat{\zeta})\nu t} \sum_{n=-\infty}^{\infty} \begin{pmatrix} X_n \\ Y_n \end{pmatrix} e^{in\nu t+ikx} + c.c. \tag{7.1}$$

Here $(\hat{\delta}+i\hat{\zeta})$ is the Floquet exponent and $e^{(\hat{\delta}+i\hat{\zeta})2\pi/\nu}$ is the Floquet multiplier. We restrict $\hat{\zeta}$ to two values corresponding to a harmonic response ($\hat{\zeta} = 0$) or to a subharmonic response ($\hat{\zeta} = 1/2$). To obtain the neutral curve for the standing waves, the ansatz (7.1) is substituted into the linearized system with $\hat{\delta} = 0$, yielding the infinite-dimensional system of equations

$$\sum_{n=-\infty}^{\infty} e^{i(n+\hat{\zeta})\nu t} \left\{ \begin{pmatrix} \mu - k^2 + \gamma(k)\cos(\chi) - i(n+\hat{\zeta})\nu & -\sigma + \beta k^2 \\ \sigma - \beta k^2 & \mu - k^2 - \gamma(k)\cos(\chi) - i(n+\hat{\zeta})\nu \end{pmatrix} \begin{pmatrix} X_n \\ Y_n \end{pmatrix} \right. \tag{7.2}$$

$$\left. + \frac{\gamma(k)\sin(\chi)}{2} \left[\begin{pmatrix} 1 & i \\ i & 1 \end{pmatrix} \begin{pmatrix} X_{n+1} \\ Y_{n+1} \end{pmatrix} + \begin{pmatrix} 1 & -i \\ -i & 1 \end{pmatrix} \begin{pmatrix} X_{n-1} \\ Y_{n-1} \end{pmatrix} \right] \right\} = 0,$$

which can be written as a matrix equation:

$$\mathbf{M}(\hat{\zeta})\mathbf{v} = \gamma(k)\mathbf{L}\mathbf{v}, \tag{7.3}$$

where

$$\mathbf{v} = (... \; X_{n-1} \; Y_{n-1} \; X_n \; Y_n \; X_{n+1} \; Y_{n+1} \; ...)^T .$$

Here $\mathbf{M}$ is block-diagonal and $\mathbf{L}$ couples adjacent modes (X_n, Y_n) and $(X_{n\pm1}, Y_{n\pm1})$. Equation (7.3) is a generalized eigenvalue problem for the eigenvalue $\gamma(k)$, which represents

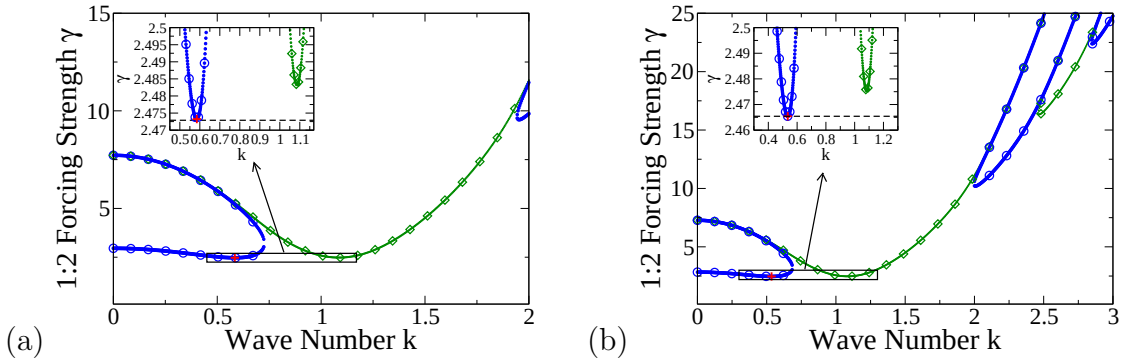

Figure 7.1. Harmonic (green, diamonds) and subharmonic (blue, circles) neutral stability curves for $\mu = -1$, $\sigma = 4$, $\beta = 3$. The parameters χ and ν are tuned to obtain the desired K. (a) For $K = 1.857$, $\chi = 0.4883189$ and $\nu = 3.824884$. (b) For $K = 2$, $\chi = 0.4767180$ and $\nu = 4.2$.

the forcing amplitude at the onset of the instability for a given k. In our formulation of the linear problem γ is assumed to be real; complex eigenvalues therefore do not correspond to solutions of the original problem. To solve for the eigenvalues for a given value of the wave number k, we truncate the sum in (7.3) at some N and calculate the eigenvalues. We test for convergence by requiring that for the real eigenvalues $\gamma_i^{(N)}$ the total change in all eigenvalues when N is increased by 1 is smaller than a tolerance Δ, $\sum(\gamma_i^{(N+1)} - \gamma_i^{(N)})^2 \leq \Delta = 10^{-10}$. We find that generally $N = 10$ is sufficient. Repeating this process over a range of k we construct the neutral stability curves $\gamma^{(H)}(k)$ for the harmonic mode ($\hat{\zeta} = 0$) and $\gamma^{(S)}(k)$ for the subharmonic mode ($\hat{\zeta} = 1/2$). The global minimum of these curves yields the respective critical values $(k_c^{(H)}, \gamma_c^{(H)})$ and $(k_c^{(S)}, \gamma_c^{(S)})$.

The weakly nonlinear analysis presented in the next chapter shows that weakly damped harmonic modes have a strong impact on the selection of subharmonic patterns via resonant triad interactions. Our aim is to exploit this sensitivity to stabilize complex patterns like superlattice patterns. We therefore focus here on parameters for which the minimum of the harmonic mode is only slightly above that of the subharmonic mode;

we use $\gamma_c^{(H)} - \gamma_c^{(S)} = 0.01$. The resonant triads rely on spatio-temporal resonances that depend decisively on the wave number ratio $K \equiv k_c^{(H)}/k_c^{(S)}$. We consider the two cases $K = 2\cos(\tan^{-1}(2/5)) = 1.857$ and $K = 2$ and show in Fig.7.1 the corresponding neutral stability curves for $\gamma_c^{(H)} - \gamma_c^{(S)} = 0.01$. In the next section we discuss how the different parameters affect this codimension-2 point.

7.2. Codimension-2 point for changing parameters

Varying the parameter χ characterizing the ratio of forcing strengths near the 2:1-resonance shifts the critical forcing parameters $\gamma_c^{(H)}$ and $\gamma_c^{(S)}$ relative to each other, while varying the parameter ν characterizing the detuning difference shifts the critical wave numbers $k_c^{(H)}$ and $k_c^{(S)}$. Requiring $\gamma_c^{(H)} - \gamma_0^{(S)} = 0.01$ for a fixed value of K defines a codimension-2 point that determines both χ and ν. For fixed $K = 2$ their dependence on the dispersion β and the damping μ is illustrated in Fig.7.2 along with the corresponding values of $\gamma_c^{(S)}$ and $k_c^{(S)}$. Since $\bar{A}$ satisfies the CGLE with the opposite signs of the imaginary parts of the equation, only positive values of β need to be considered.

For $\chi = 0$ the critical wave number is given by $k_c^2 = (\mu + \nu\beta)/(1 + \beta^2)$ corresponding to a critical forcing $\gamma_c^2 = (\nu - \mu\beta)^2/(1 + \beta^2)$ [**24**]. Thus, k_c has a local maximum and $k_c^2 \sim 1/\beta$ for large β; qualitatively the same behaviour is found at the codimension-2 point, as illustrated in Fig.7.2d. Fig.7.2c confirms that the amount of forcing necessary to generate patterns increases as one goes further below the Hopf bifurcation, i.e. as μ becomes more negative.

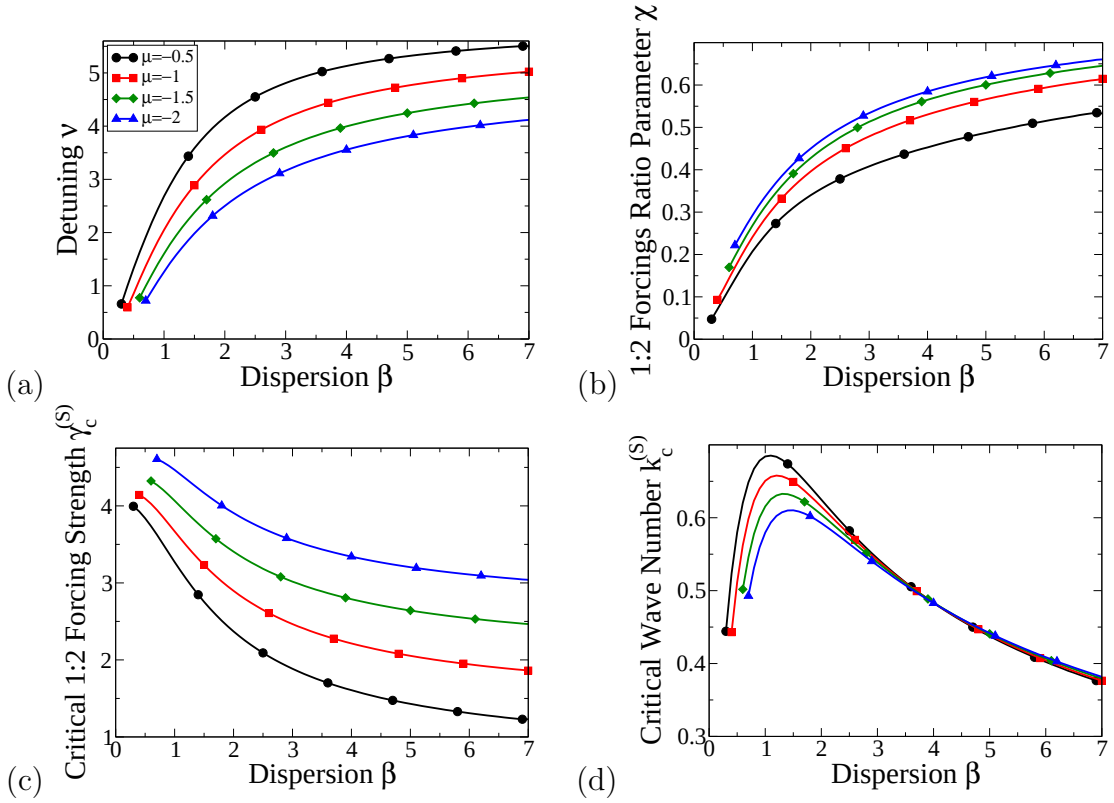

Figure 7.2. Linear parameters at the codimension-2 point $K = 2$ and $\gamma_c^{(H)} - \gamma_0^{(S)} = 0.01$ for detuning $\sigma = 4$ as a function of the dispersion β and the damping μ. (a) Detuning ν, (b) forcing ratio χ, (c) critical forcing strength $\gamma_c^{(S)}$, and (d) critical wave number $k_c^{(S)}$

CHAPTER 8

Weakly Nonlinear Analysis and Pattern Selection

To determine the stability of the desired subharmonic patterns we derive the corresponding amplitude equations by performing a weakly nonlinear analysis of (6.3). We then use energy arguments to guide us in terms of the relative stability of the various pattern comprised of different numbers of modes. We are in particular interested in the stability of patterns comprising three or more modes.

8.1. Amplitude Equations

Splitting the CGLE (6.3) again into real and imaginary parts, we obtain a system of real partial differential equations. For a subharmonic pattern with N modes, we expand (A_r, A_i) about $(0,0)$ as

$$\begin{pmatrix} A_r \\ A_i \end{pmatrix} = \epsilon \left\{ \sum_{m=1}^{N} Z_m(T) \left(\sum_{n=-\infty}^{\infty} \begin{pmatrix} X_n \\ Y_n \end{pmatrix} e^{i(n+\frac{1}{2})\nu t} \right) e^{i\mathbf{k}_m \cdot \mathbf{x}} + c.c. \right\} + \epsilon^2 \begin{pmatrix} A_r^{(2)} \\ A_i^{(2)} \end{pmatrix} + \epsilon^3 \begin{pmatrix} A_r^{(3)} \\ A_i^{(3)} \end{pmatrix} + \ldots, \quad |\mathbf{k}_m| = k_c \tag{8.1}$$

where $0 < \epsilon \ll 1$ and the complex amplitudes $Z_m(T)$ depend on the slow time $T = \epsilon^2 t$. The corresponding wave vectors are denoted by $\mathbf{k}_m$. We also expand γ as $\gamma = \gamma_c + \epsilon^2 \gamma_2$.

A standard but lengthy calculation yields amplitude equations for the $Z_j(T)$ describing the $N-$mode pattern:

$$\frac{dZ_i}{dT} = \lambda\gamma_2 Z_i - \left(b_0|Z_i|^2 + \sum_{j=1, j\neq i}^{N} b(\theta_{ij})|Z_j|^2 \right) Z_i, \quad i = 1 \ldots N, \tag{8.2}$$

where θ_{ij} corresponds to the angle between the wave vectors $\mathbf{k}_i$ and $\mathbf{k}_j$. To verify our calculations we compared the resulting amplitude equation coefficients with those obtained through our previous calculations presented in Chapter 4, for the special cases $\chi = 0$ and $\chi = \pi/2$ where such comparison is possible, for several parameter sets. We found that the coefficient values agree within machine precision. Note that there are no quadratic terms in (8.2), because these amplitude equations correspond to subharmonic patterns and must therefore be equivariant under the symmetry $Z_j \to -Z_j$.

In order to have stable complex patterns made up of many modes, the competition between modes needs to be sufficiently weak. Since in the amplitude equations (8.2) only pairwise mode interactions arise, a minimal condition for complex patterns to be stable is the stability of rectangle patterns, which are comprised of 2 modes at some angle θ_r, with respect to stripes. This requires $|b(\theta_r)/b_0| < 1$.

The self- and cross-coupling coefficients, b_0 and $b(\theta_{ij})$, respectively, can be strongly influenced by resonant triad interactions as illustrated in Fig.8.1. There the black circles represent the subharmonic critical circle and the red circle the wave vector of the most weakly damped harmonic mode for a given choice of critical forcing γ. At quadratic order resonant triad interaction takes place through two mechanisms, each feeding into the coefficients at cubic order. The first mechanism is through the interaction of two different wave vectors ($\mathbf{k}_1 + \mathbf{k}_2$ in Fig.8.1a) separated by an angle θ_r: the cross-coupling coefficient $b(\theta)$ is strongly impacted near $\theta = \theta_r$ if the mode excited at quadratic order through the interaction of these two wave vectors is weakly damped [**32**, **33**, **37**, **39**]. The angle

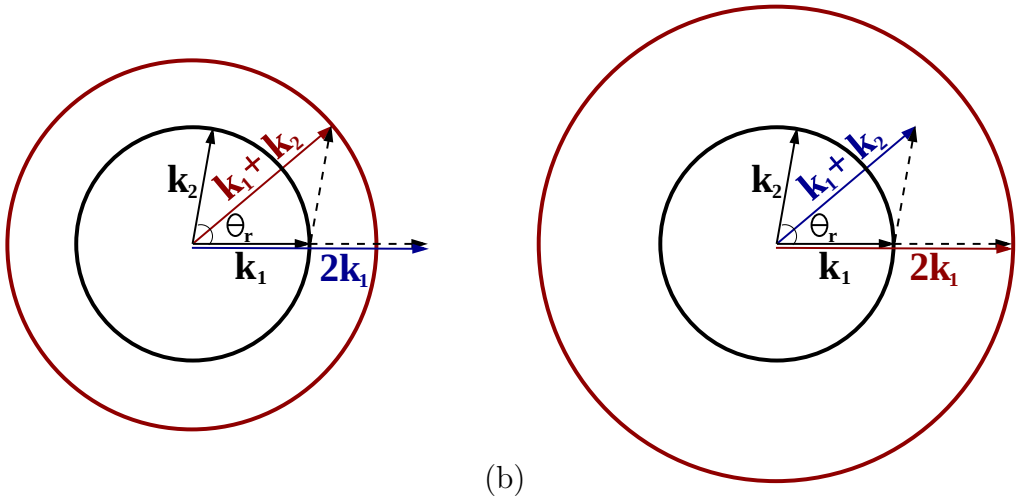

(a) (b)

Figure 8.1. Resonant triad interaction. Inner circle represents critical circle at $k_c^{(S)}$, outer circle represents weakly damped mode at (a) $K = 2\tan^{-1}(2/5)$, (b) $K = 2$. The wave vector $\mathbf{k}_1 + \mathbf{k}_2$ is relevant for $b(\theta)$ while $2\mathbf{k}_1$ affects b_0 (cf. eq.(8.2)).

θ_r is a function of the wavenumber ratio K, $\theta_r = 2\cos^{-1}(K/2)$. The second mechanism is through the interaction of a wave vector with itself ($2\mathbf{k}_1$ in Fig.8.1b): in this case, if the harmonic mode at $2\mathbf{k}_c$ is weakly damped, the self-coupling coefficient b_0 is strongly influenced [**31**,**39**,**42**]. The $|\mathbf{k}| = 0$ mode is also driven at quadratic order, but is strongly damped. In Fig.8.1a $K < 2$ ($\theta_r \neq 0$), so the mode excited by the vector $\mathbf{k}_1 + \mathbf{k}_2$ is weakly damped and the mode excited by the $2\mathbf{k}_1$ vector is strongly damped. In Fig.8.1b $K = 2$ ($\theta_r = 0$), so the opposite is true.

Fig.8.2 shows the effect of the resonant triad interactions on the self-coupling coefficient b_0, by plotting b_0 as a function of the 3:1 forcing phase Φ for different values of the 3:1 forcing strength ρ. Notice that the self-coupling coefficient b_0 exhibits sinusoidal behaviour with period π in Φ. This is because the quadratic term $\bar{A}^2$ in (6.3) has the coefficient $\rho e^{i\Phi}$. The particular solution of (6.3) at quadratic order in ϵ, $(A_r^{(2)}, A_i^{(2)})^T$ in (8.1), is

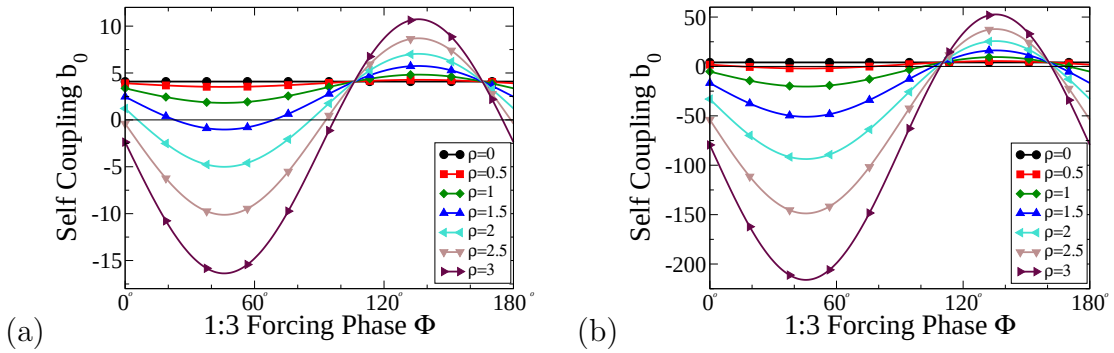

Figure 8.2. Self-coupling coefficient b_0 plotted against the 3:1 forcing phase Φ for various values of the 3:1-forcing strength ρ with $\alpha = -1$. (a) $K = 2\cos(\tan^{-1}(2/5)$, other parameters as in Fig.7.1a; (b) $K = 2$, other parameters as in Fig.7.1b.

therefore proportional to $e^{i\Phi}$. At cubic order that particular solution interacts with the linear solution also through $\rho e^{i\Phi}\bar{A}^2$, generating a term proportional to $\rho^2 e^{2i\Phi}$. Thus both the self- and cross-coupling coefficients b_0 and $b(\theta)$ in (8.2) are linear functions of of $\rho^2 sin(2(\Phi - \Phi_0))$ where the phase shift Φ_0 seen in Fig.8.2 results from the projection of the cubic term onto the complex left-eigenvector. Fig.8.2a corresponds to the case illustrated in Fig.8.1a with $K = 2\cos(\tan^{-1}(2/5))$; with this choice of K the resonance angle $\theta_r \equiv 2\tan^{-1}(2/5)$ is near $\pi/4$ and the associated Fourier modes fall on a regular grid [**87**] for later comparison with numerical simulation. In Fig.8.2b $K = 2$ and the effect of the resonant triad on b_0 is greatly enhanced - note the difference in scale compared to Fig.8.2a - and even quite weak forcing ρ can change the sign of b_0 and with it the direction of the bifurcation to stripes. In the following we restrict ourselves to values of the phase Φ for which $b_0 > 0$ and the stripes bifurcate supercritically.

To assess the mode competition for $K = 2$, Fig.8.3 shows the dependence of the cross-coupling coefficient ratio $b(\theta)/b_0$ on θ. To enhance the stability of patterns comprised of multiple modes by maximizing the range of weak competition we maximize the damping

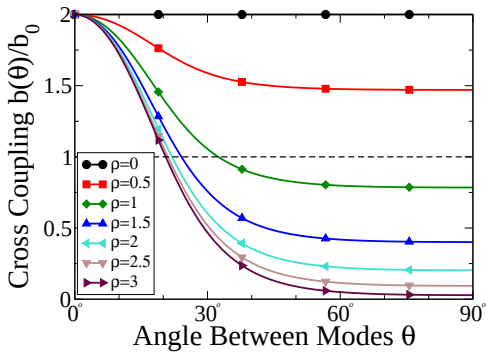

Figure 8.3. Coupling coefficient ratio $b(\theta)/b_0$ for $K = 2$ with $\Phi = 3\pi/4$ with linear parameters as in Fig.7.1b and nonlinear dispersion $\alpha = -1$ for different strengths of 3:1-forcing ρ. Rectangles are stable for $|b(\theta)/b_0| < 1$.

b_0 and choose $\Phi = 3\pi/4$ (cf. Fig.8.2). Since $K = 2$, the self-coupling b_0 is enhanced by the resonant triad, while away from $\theta = \theta_r \equiv 0$ the cross-coupling $b(\theta)$ is only weakly affected. Thus, as expected, for $\rho \geq 1$ the ratio $b(\theta)/b_0$ is strongly reduced away from $\theta = 0$ allowing for rectangle patterns corresponding to angles as small as $\theta = \theta_c \sim 30°$ and smaller to be stable with respect to stripes. Consequently, patterns comprised of four or possibly even more modes are expected to be stable, as discussed in Section 8.2.

The mode interaction also depends on the linear dispersion β and the nonlinear dispersion parameter α. These two parameters are system parameters that may not be tunable in experiments. It is therefore of interest to assess over what range in these parameters complex patterns are to be expected and to what extent the forcing parameters can be adjusted so as to reach the regions of interest for given system parameters.

The effect of the nonlinear dispersion parameter α on the ratio $b(\theta)/b_0$ is shown in Fig.8.4a for $\rho = 1$. Somewhat similar to the dependence on ρ, with increasing α the ratio $b(\theta)/b_0$ decreases and the range of θ for which rectangle patterns are stable increases. For more positive values of α even small forcing amplitudes ρ reduce the mode interaction

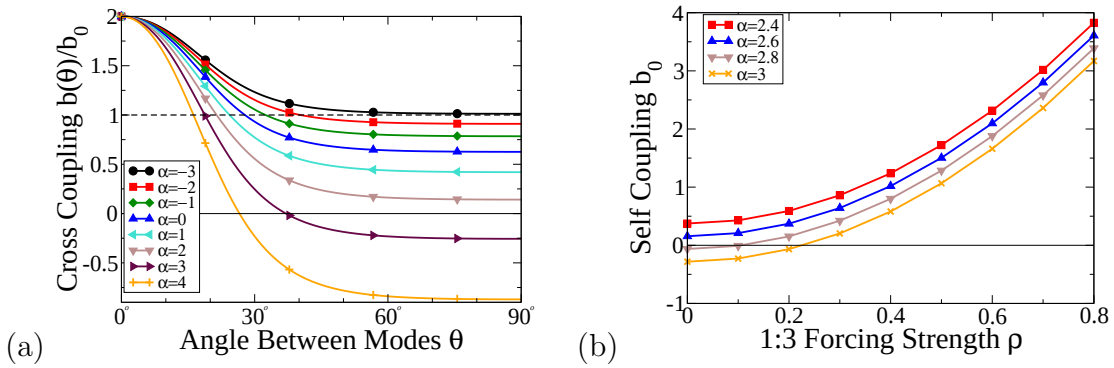

Figure 8.4. Coupling coefficient ratio $b(\theta)/b_0$ (a) and self-coupling b_0 (b) for $K = 2$ and $\Phi = 3\pi/4$ with parameters as in Fig.7.1b for 3:1 forcing strength $\rho = 1$ and different values of the nonlinear dispersion parameter α.

significantly, but as ρ is increased the ratio $b(\theta)/b_0$ saturates at values that are not much smaller than shown in Fig.8.3 for $\alpha = -1$. In the simulations discussed in the next chapter we use a moderate value of $\alpha = -1$. For $2:1$-forcing it was found that the self-coupling coefficient b_0 changes sign for $\alpha = \beta$, rendering the bifurcation subcritical for $\alpha > \beta$ [**24**]. With the addition of $3:1$-forcing the sign of b_0 depends also on the forcing strength ρ and, in fact, even for $\alpha = \beta$ the bifurcation to stripes can be made supercritical by increasing the forcing strength, cf.(4.6). This situation persists when the $2:1$ forcing is modulated, illustrated in Fig.8.4b where b_0 is shown as a function of ρ for different values of α near $\beta = 3$.

To assess the dependence of the mode interaction on the linear dispersion coefficient β we do not perform a scan in β but rather focus on one other value, $\beta = 1.4$, which corresponds to the value found experimentally for the Belousov-Zhabotinsky reaction [**84**]. We adjust the forcing parameters χ and ν to stay at the codimension-2 point $K = 2$ and $\gamma_c^{(H)} - \gamma_0^{(S)} = 0.01$. The nonlinear dispersion coefficient was found in the experiments to be $\alpha = -0.4$. Since the functional form of the angle dependence of $b(\theta)$ does not change much

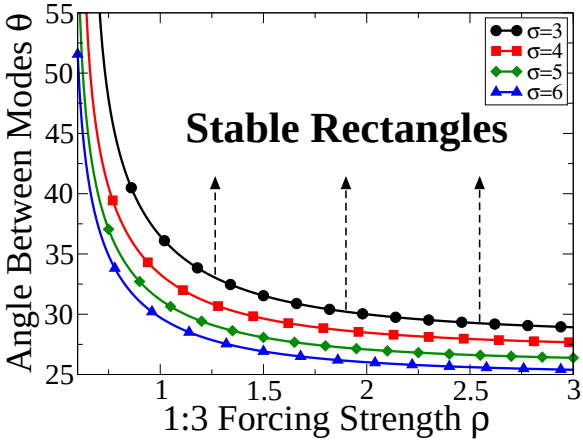

Figure 8.5. Belousov-Zhabotinsky case. Minimal angle θ_c for which rectangles are stable to stripes ($b(\theta_c)/b_0 = 1$) as a function of the 3:1-forcing strength ρ for different values of the detuning σ. Parameters $\mu = -1$, $\alpha = -0.4$, $\beta = 1.4$ with χ and ν tuned to the codimension-2 point $K = 2$ and $\gamma_c^{(H)} - \gamma_0^{(S)} = 0.01$. .

with the parameters we use the minimal angle θ_c for which rectangles are still stable with respect to stripes as a proxy for the strength of the mode competition. Thus $b(\theta_c)/b_0 = 1$. In Fig.8.5 we show θ_c as a function of the forcing strength ρ for various values of the overall detuning σ. Clearly, even for these experimentally relevant parameters the resonant triad interaction can be exploited to make the mode competition sufficiently weak to stabilize rectangle patterns over a wide range of angles. This suggests that multi-mode patterns should become stable for moderate values of the forcing parameters, which is confirmed below.

For $K = 2\cos(\tan^{-1}(2/5))$ the resonant triad affects mostly $b(\theta)$ rather than b_0. Fig.8.6 shows the resulting ratio $b(\theta)/b_0$ as a function of the angle θ. To ensure $b_0 > 0$ we use again $\Phi = 3\pi/4$. As expected $b(\theta)/b_0$ exhibits a prominent peak near $\theta = \theta_r = 2\tan^{-1}(2/5)$. As in Fig.8.3 the enhancement is increased with ρ (Fig.8.6a), and as α becomes more positive (Fig.8.6b). We also see from these plots that the range for which $b(\theta)/b_0 < 1$, that is, the

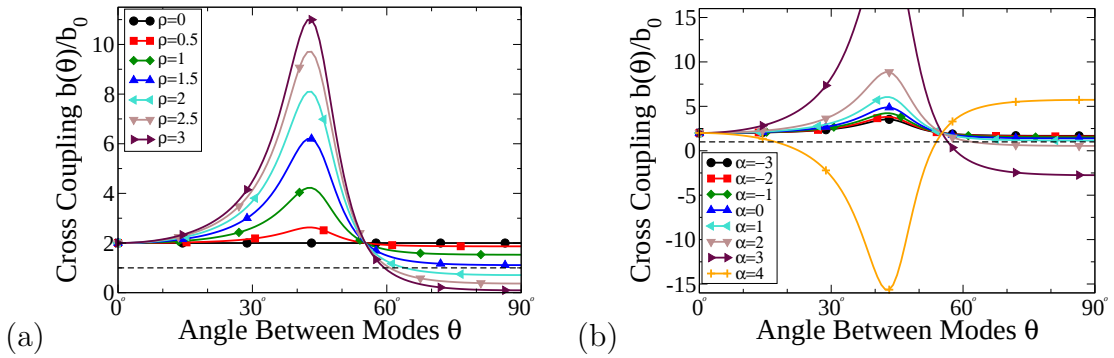

Figure 8.6. Coupling coefficient ratios for $K = 2\cos(\tan^{-1}(2/5))$ and $\Phi = 3\pi/4$ with parameters as in Fig.7.1a for (a) nonlinear dispersion parameter $\alpha = -1$ and different strengths of 3:1-forcing ρ and (b) 3:1 forcing strength $\rho = 1$ and different values of the nonlinear dispersion parameter α.

range of stable rectangles, is limited to $60° \lesssim \theta < 90°$. Thus, we anticipate only stripe, square or hexagon patterns to be stable in this regime.

For $K = 2\cos(\tan^{-1}(2/5))$ the competition between modes subtending an angle near θ_r is strongly enhanced for values of the 3:1-forcing phase near $\Phi = 3\pi/4$ resulting in a suppression of θ_r-rectangles. For the same K but $\Phi = \pi/4$, we expect correspondingly a selective enhancement of the θ_r-rectangles as long as ρ is sufficiently small so that $b_0 > 0$ (see Fig.8.2). This is shown in Fig.8.7, which depicts the behavior of the cubic coupling coefficient ratio as a function of the angle θ for different values of the 3:1-forcing strength ρ and of the nonlinear dispersion α in this regime. As the 3:1-forcing strength ρ is increased, and as the nonlinear dispersion α becomes more positive, the dip with minimum at $\theta = \theta_r = 2\tan^{-1}(2/5)$ becomes more and more pronounced. In parallel the range in θ of stable rectangle patterns increases around θ_r. Due to the narrowness of the dip we expect at most stripe and θ_r-rectangle patterns to be stable. For values of ρ and α such that $b(\theta)/b_0 < -1$ the corresponding rectangles pattern become subcritical and our

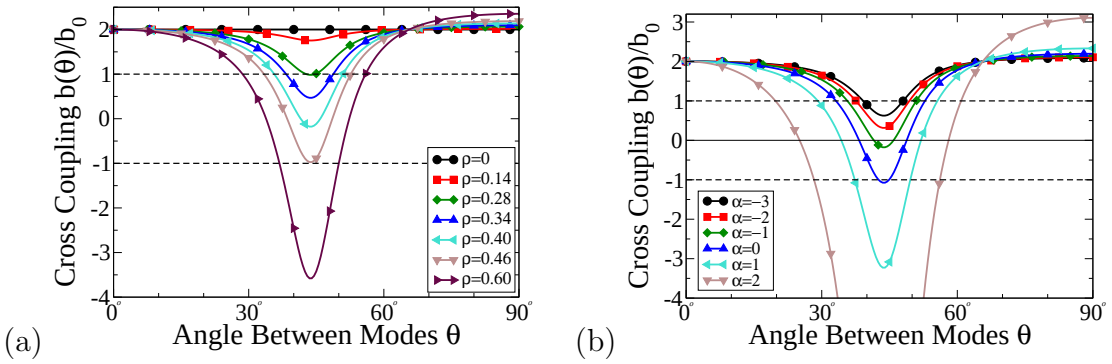

Figure 8.7. Coupling coefficient ratios for $K = 2\cos(\tan^{-1}(2/5))$ and $\Phi = \pi/4$ with parameters as in Fig.7.1a for (a) nonlinear dispersion parameter $\alpha = -1$ and different strengths of 3:1-forcing ρ and (b) 3:1 forcing strength $\rho = 1$ and different values of the nonlinear dispersion parameter α.

weakly nonlinear analysis to cubic order is insufficient to make predictions about pattern selection involving those modes.

8.2. Competition between complex patterns

If multiple patterns are simultaneously linearly stable they can coexist and compete in sufficiently large systems. Typically they then form domains and the competition involves the motion of walls separating the domains. If the system allows a Lyapunov function that function can serve as an energy and this competition can be characterized in terms of the difference between the energies associated with the respective patterns. Unless the domain walls become pinned by the underlying pattern [**88**, **89**], it is expected that the final state arising from random initial conditions consists of the pattern with minimal energy [**45**, **90**].

Because $b(\theta_{ij}) = b(\theta_{ji})$, (8.2) can indeed be derived from a Lyapunov function $\mathcal{F}$, such that $\frac{dZ_j}{dT} = -\frac{\partial \mathcal{F}}{\partial \bar{Z}_j}$ with

$$\mathcal{F} = \sum_{n=1}^{N} \left[-\lambda(\gamma - \gamma_c)|Z_n|^2 + \frac{1}{2}(b_0|Z_n|^4 + \sum_{m=1, m\neq n}^{N} b(\theta_{mn})|Z_n|^2|Z_m|^2) \right] \tag{8.3}$$

for a pattern with N modes. The Lyapunov function gives the energy $\mathcal{F}_{\mathcal{N}}$ for an equal-amplitude $N-$mode pattern, which we rescale to obtain $\hat{\mathcal{F}}_N$,

$$\hat{\mathcal{F}}_N \equiv \frac{\mathcal{F}_N}{(\gamma - \gamma_c)^2} = \frac{-(N/2)\lambda^2}{b_0 + \sum_{n=1, n\neq j}^{N} b(\theta_{jn})}, \tag{8.4}$$

for some $j \in [1, N]$. The sum in the denominator represents the sum of all cubic coefficients in (8.2). Since the modes are evenly spaced, the choice of j in (8.4) is arbitrary. We use the energy $\mathcal{F}_{\mathcal{N}}$ as a guide to predict which N-mode pattern will ultimately emerge.

Figs.8.8-8.11 show how the energies $\hat{\mathcal{F}}_{\mathcal{N}}$ vary with ρ, the strength of forcing near 3:1 resonance, for different patterns with N modes evenly spaced in Fourier space. Since the energy depends smoothly on the angles θ_{jn} (cf. (8.4)) little change in the energy is expected if the modes are not quite evenly spaced.

For $K = 2$ and $\alpha = -1$ the energies of the patterns with more than 3 modes are very close to each other, as seen in Fig.8.8a. For clarity we show therefore in Fig.8.8b the difference $\hat{\mathcal{F}}_N - \hat{\mathcal{F}}_4$. As one increases ρ, first stripe patterns ($N = 1$), then square patterns ($N = 2$), then hexagons ($N = 3$), and eventually supersquares ($N = 4$) have the lowest energy. For the respective parameter values, these are therefore the patterns we expect eventually to arise from noisy initial conditions. Also indicated in Figs.8.8a,b is the linear stability of these patterns. Here we determine the linear stability of an N-mode

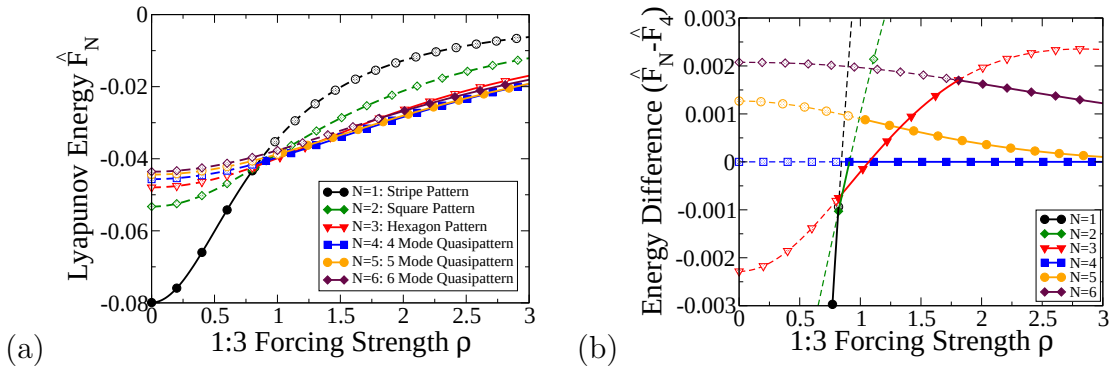

Figure 8.8. (a) Rescaled energies $\hat{\mathcal{F}}_N$ for evenly spaced modes in the case $K = 2$. Parameters as in Fig.7.1b with $\alpha = -1$ and $\Phi = 3\pi/4$. Solid (dashed) lines denote linearly stable (unstable) patterns. (b) Energy difference $\hat{\mathcal{F}}_N - \hat{\mathcal{F}}_4$ for the same data as shown in (a). The 4-mode pattern is preferred for $\rho > 1.2$.

pattern by calculating the linear stability of that pattern within the space spanned by the N evenly spaced modes and an additional mode rotated an arbitrary angle ψ with respect to the $\mathbf{k}_1$-mode in Fourier space. For larger ρ patterns comprised of 5 and 6 modes are linearly stable but do not have the lowest energy, though for $\rho > 2$ the energies of the patterns with 4 and 5 modes are very close.

In Section 8.1 we showed that for a more positive α relatively small values of the 3:1-forcing strength ρ are sufficient to stabilize rectangle patterns over a wide range of θ (cf. Fig. 8.4a). As a result we expect that the resonant triad can stabilize patterns comprised of more modes than was possible in the case $\alpha = -1$ depicted above. Fig.8.9b shows that this is indeed the case. Increasing α to $\alpha = 2.5$ reduces for $\rho > 1$ the energy of the 5-mode patterns below that of the 4-mode pattern and renders it the pattern with the lowest energy among the patterns with equally spaced modes. We therefore expect that in numerical simulations 5-mode patterns would arise over a large range in ρ.

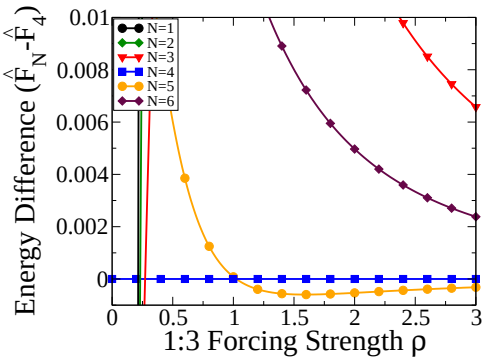

Figure 8.9. Rescaled energies $\hat{\mathcal{F}}_N$ for evenly spaced modes in the case $K = 2$. Parameters as in Fig.7.1b with $\alpha = 2.5$ and $\Phi = 3\pi/4$. 5-mode pattern preferred for $\rho > 1$.

For the parameter set that is relevant for the Belousov-Zhabotinsky reaction [**84**] we found that the mode competition is also sufficiently reduced to suggest the stability of multi-mode patterns (cf. Fig.8.5). This is confirmed in Fig.8.10, which shows the energies for $\alpha = -0.4$ and $\beta = 1.4$. While for $\sigma = 4$ the 4-mode pattern has an energy that is only barely below that of the hexagons and reaches those lower values only for large forcing strengths ρ (Fig.8.10), increasing σ to $\sigma = 6$ pushes the energy of the 4-mode pattern well below that of the hexagons (Fig.8.10b). We therefore expect that the complex patterns we discuss in this paper are accessible in this experimental system.

For $K = 2\cos(\tan^{-1}(2/5))$ with $\Phi = 3\pi/4$ (Fig.8.11a), stripes are again stable for small ρ. As ρ is increased stripes lose stability and square patterns ($N = 2$) become linearly stable and have the lowest energy beyond $\rho \approx 1.6$. Hexagon patterns ($N = 3$) become linearly stable at $\rho = 2.7$, but do not have lower energy than the square patterns. Patterns with more than 3 modes are linearly unstable, which is consistent with the predictions based on the coupling coefficient shown in Fig.8.6a: Fourier modes subtending angles smaller than $\pi/3$ compete strongly and therefore do not coexist stably. In simulations

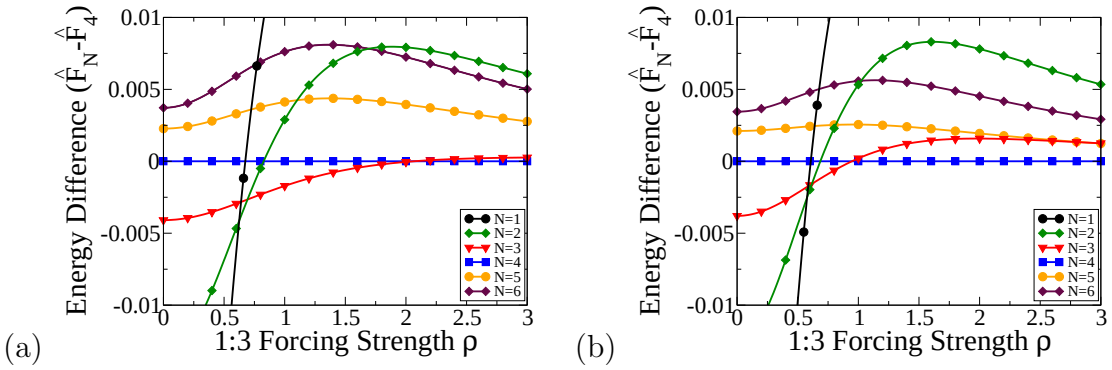

Figure 8.10. Pattern selection for Belousov-Zhabotinsky parameters [**84**]. Rescaled energy difference $\hat{\mathcal{F}}_N - \hat{\mathcal{F}}_4$ for N evenly spaced modes. Here $\alpha = -0.4$, $\beta = 1.4$, $\sigma = 4$ (a) and $\sigma = 6$ (b).

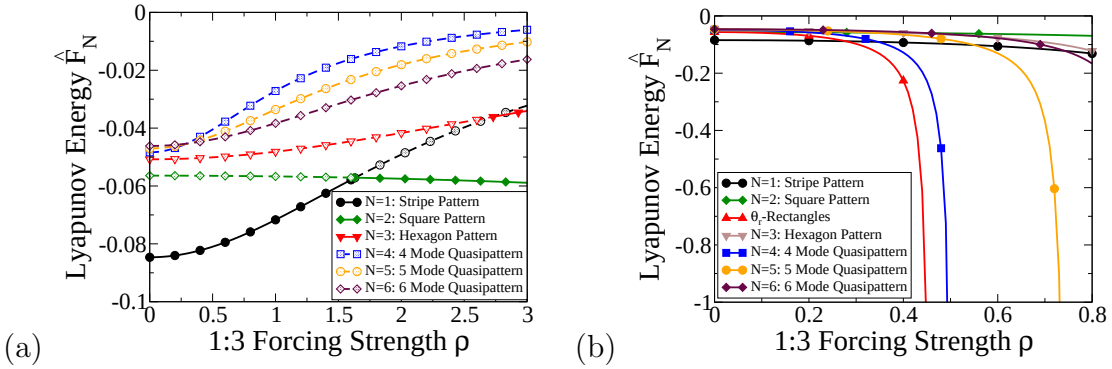

Figure 8.11. Rescaled energies $\hat{\mathcal{F}}_N$ for evenly spaced modes in the case $K = 2\cos(\tan^{-1}(2/5))$. Parameters as in Fig.7.1a with $\alpha = -1$ and (a) $\Phi = 3\pi/4$ (cf. Fig.8.6), (b) $\Phi = \pi/4$ (cf. Fig.8.7). In (a), solid (dashed) lines denote linearly stable (unstable) patterns.

starting from random initial conditions, we therefore expect either stripe patterns (for $\rho < 1.6$) or square patterns to arise. For $\Phi = \pi/4$, shown in Fig.8.11b, stripes again are stable and have the lowest energy for small ρ. For $\rho = 0.28$ they become unstable to rectangle patterns spanned by modes subtending an angle of $\theta = \theta_r \equiv 2\tan^{-1}(2/5)$. As ρ is increased to $\rho = 0.46$ this rectangle pattern becomes subcritical (cf. Fig.8.7) and the weakly nonlinear analysis taken to cubic order and the associated energy arguments

are not sufficient to make predictions about pattern selection. For $\rho > 0.28$ none of the patterns with equally spaced modes has lower energy than the rectangle pattern selected by the resonant triad. Note that in the cubic truncation (8.4) the energy for a pattern diverges when the respective bifurcation changes direction.

CHAPTER 9

Numerical Simulations

To confirm our predictions for the pattern selection, we perform numerical simulations of the complex Ginzburg-Landau equation (6.3). Being interested in the formation of complex patterns comprised of 3 or more modes, we focus on the case $K = 2$. The linear parameters are as in Fig.7.1a with nonlinear parameters $\alpha = -1$, $\Phi = 3\pi/4$, and various values of ρ. We use periodic boundary conditions and employ a pseudo-spectral method with Crank-Nicolson-Adams-Bashforth time stepping. To capture higher order harmonics we use 128 modes and their complex conjugates in Fourier space, and for the purposes of accuracy we use 256 time steps per period $T = 4\pi/nu$.

9.1. Simulations in a small domain

To test the weakly nonlinear analysis we focus on the regime where both hexagons and 4-mode patterns are linearly stable (Fig.8.8) and run numerical simulations in domains of minimal size for each pattern. Thus, all participating modes lie exactly on the critical circle. Since the 4-mode pattern with evenly spaced modes does not lie on a regular Fourier grid we approximate it by modes spaced at $\theta_1 = 2\tan^{-1}(1/2) \approx 53^\circ$ and $\theta_2 = \pi/2 - 2\tan^{-1}(1/2) \approx 37^\circ$ apart. Due to the smooth dependence of the energy on the angles θ_{jn} (cf. Eq.(8.4)) little change in the energy is expected if the modes are not quite evenly spaced. From Fig.8.8b, for a 3:1-forcing strength $\rho = 1$ hexagons and 4-mode patterns are both linearly stable to stripes and the 4-mode patterns are also linearly stable to square

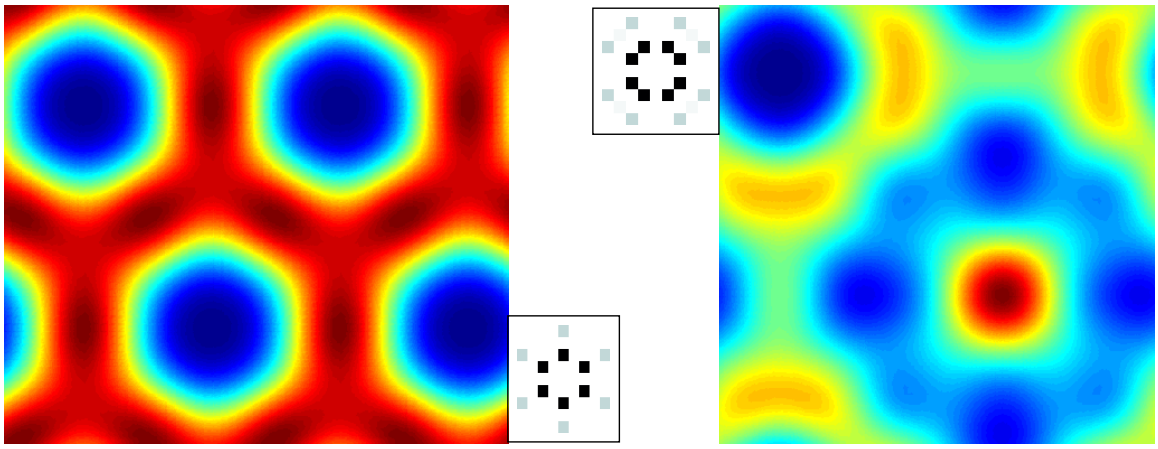

(a) (b)

Figure 9.1. Small-system numerical simulations of (6.3) for 3:1 forcing strength $\rho = 1$. (a) Hexagon pattern in rectangular domain, $L_x = 4\pi/k_c^{(S)} \approx 23.49$, $L_y = L_x/\sqrt{3} \approx 13.56$. (b) Supersquare pattern in square domain, $L = 2\pi/(\cos(\tan^{-1}(1/2))k_c^{(S)} \approx 13.13$. Parameters as in Fig.7.1b (case $K = 2$) with $\alpha = -1$, $\Phi = 3\pi/4$.

patterns. The numerical simulations confirm these stability predictions. Starting with a noisy initial condition generated from a uniform distribution with amplitude 0.05 we get as expected hexagons (Fig.9.1a) and supersquares (Fig.9.1b). Fig.9.1 also illustrates the slight difference in the domain sizes used in the simulations, which are required to accommodate the patterns.

9.2. Simulations in a large domain

To investigate the competition between N-mode patterns with different values of N in the same computational domain we perform simulations in a large system of linear size $L_x = L_y \equiv L$, given below, representing 40 wavelengths. Fig.8.8b shows that near $\rho = 1$ hexagons and 4-mode patterns are both linearly stable, but the pattern with minimal energy depends on ρ. In order to investigate the competition between these planforms

we start each simulation with the same noisy initial condition, generated from a uniform distribution with amplitude 0.01, and vary only ρ. Moreover, in order to clearly identify the *nonlinear* competition between hexagons and 4-mode patterns and its dependence on ρ, we choose L such that the Fourier modes with $\theta = \pi/3$ and $\theta = \pi/4$ have the same growth rates. This is achieved by taking $L = 40(2\pi/(k_c^{(S)} - d)) \approx 473.39$ for which the modes for the hexagons and the 4-mode patterns are at an equal distance $d = 0.004159$ on opposite sides of the critical circle.

To visualize the competition between the modes near the critical circle, Fig.9.2 shows the temporal evolution of the magnitude of the Fourier modes inside a narrow annulus around the critical circle, divided into bins with an angular width of 2° plotted stroboscopically at multiples of the period $4\pi/\nu$. For $\rho = 0.8$, based on energy arguments and the linear stability illustrated in Fig.8.8b, we anticipate the final state to consist of a stripe pattern. This is confirmed by the numerical simulation. While in the Fourier transform Fig.9.2a initially three modes come up, reflecting the linear stability of hexagons for $\rho = 0.8$, ultimately the pattern with lower energy, stripes, dominates and only a single mode remains. The splitting of the peak into two modes reflects a slight undulation of the resulting pattern, which is apparent in the snapshot of part of the final solution shown in Fig.9.3a. The competition can also be seen in in TimeEvolutionMovie_rhoIs0p8.mov (available in [**48**], and at [**91**]), which shows the temporal evolution of the full pattern strobed with period $4\pi/\nu$. More careful inspection shows that the middle peak, which seems weaker, actually consists of two modes of lesser strength that are slowly converging to a single strong peak.

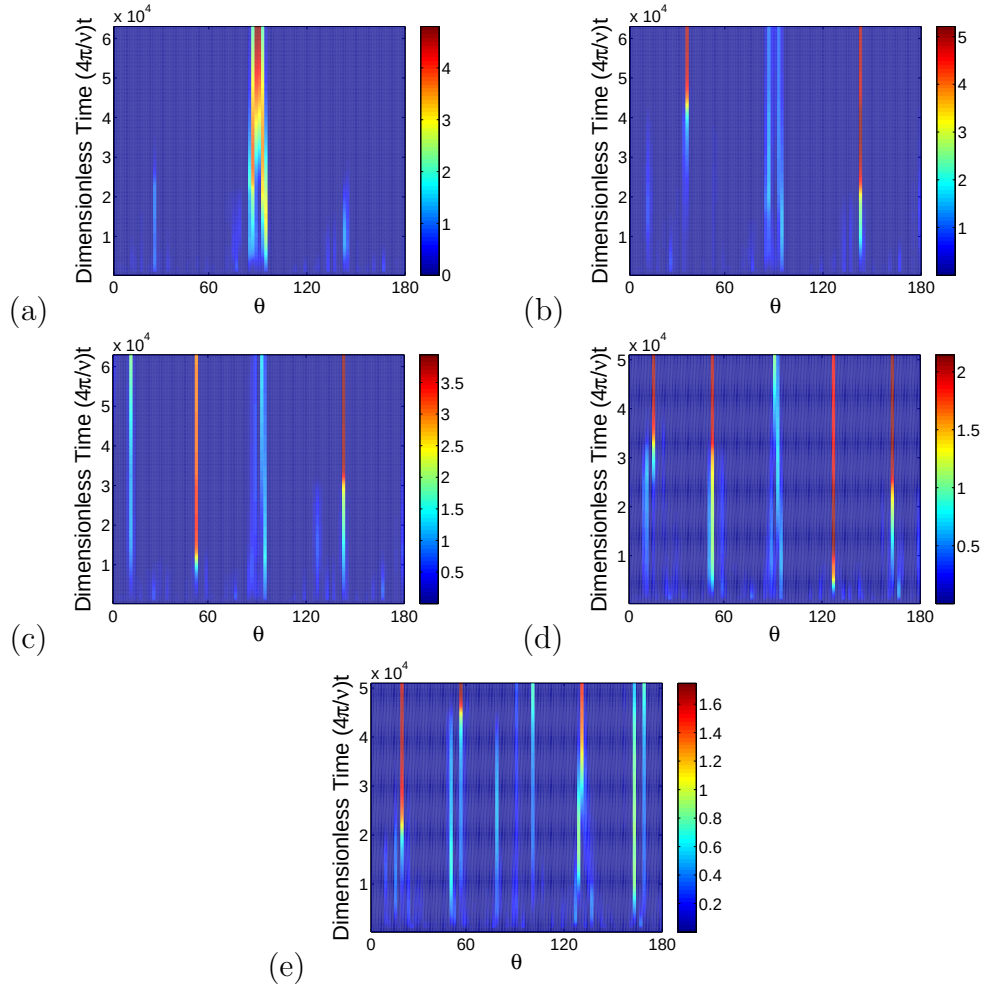

Figure 9.2. Strobed time dependence of the power spectrum in an annulus around the critical circle for varying 3:1 forcing strengths ρ. Parameters as in Fig.7.1b with $\alpha = -1$ and $\Phi = 3\pi/4$. All simulations use the same noisy initial condition. (a) $\rho = 0.8$, (b) $\rho = 1$, (c) $\rho = 1.2$, (d) $\rho = 2$, (e) $\rho = 3$.

Fig.9.2b shows the evolution of the Fourier transform for $\rho = 1$ corresponding to the time evolution of the full pattern shown in TimeEvolutionMovie_rhoIs1.mov (available in [**48**], and at [**91**]). As with the $\rho = 0.8$ case, initially the amplitudes of three modes grow. In contrast to the $\rho = 0.8$ case, however, for $\rho = 1$ stripes are unstable to hexagons, and hexagons have the lowest energy. Correspondingly the three modes persist resulting in

the hexagon patterns shown in Fig.9.3b. Note that the hexagon patterns are comprised of domains of up- and down-hexagons characterized by white and black centers, respectively. This reflects the fact that the amplitude equations (8.2) for these subharmonic patterns have no quadratic term, so neither the up- nor the down-hexagons are preferred. Whether eventually one of the two types wins out over the other depends on the interaction between the fronts connecting the domains.

For $\rho = 1.2$ we anticipate from Fig.8.8b that the resulting solution will be a 4-mode pattern. Indeed, Fig.9.2c shows 4 modes in the Fourier transform, though they are not quite equally spaced. The corresponding pattern evolution is shown in TimeEvolution-Movie_rhoIs1p2.mov (available in [**48**], and at [**91**]); Fig.9.3c shows the final state, characterized by supersquare (dash-dotted, blue circle) and antisquare (dashed, yellow circles) elements with approximate 4-fold rotational symmetry [**92**], as well as approximate 8-fold symmetric elements (solid, white circle).

From Fig.8.8b a 4-mode pattern is also anticipated for $\rho = 2$, but the numerical simulation actually results in a 5-mode pattern as shown in Fig.9.2d. The energies for evenly-spaced 4- and 5-mode patterns are very close for this forcing strength. Therefore changes in the energies that result from an uneven distribution of the modes may render the 5-mode pattern energetically lower. The corresponding pattern features elements with approximately 5- and 10-fold rotational symmetry (dashed,yellow and solid, white circles, respectively, in Fig.9.3d). For $\rho = 3$ even more modes persist for a long time and at the final time shown, $4\pi t/\nu = 5 \cdot 10^4$, the pattern has not settled into its final state yet. The

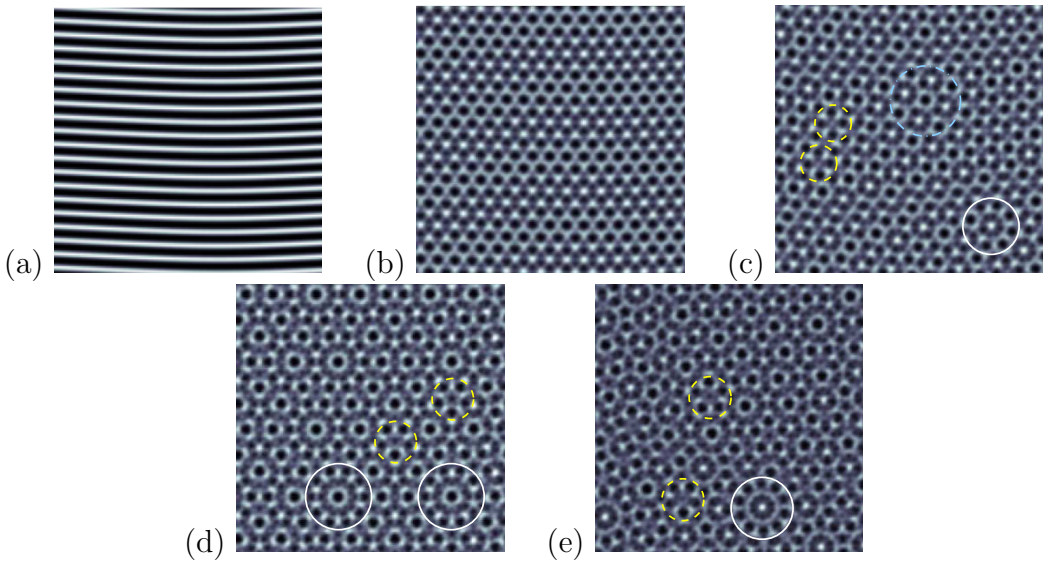

Figure 9.3. Zoom view ($0.25L \times 0.25L$) of final state at time $4\pi t/\nu = 5 \cdot 10^4$ for varying values of 3:1 forcing ρ with $L = 40(2\pi/(k_c^{(S)} - d)) \approx 473.39$. Other parameters as in Fig.7.1b (case $K = 2$) with $\alpha = -1$, $\Phi = 3\pi/4$. The circles mark characteristic features of the patterns. (a) $\rho = 0.8$, (b) $\rho = 1$, (c) $\rho = 1.2$, (d) $\rho = 2$, (e) $\rho = 3$.

temporal evolution of the full patterns for $\rho = 2$ and $\rho = 3$ are shown in TimeEvolution-Movie_rhoIs2.mov and TimeEvolutionMovie_rhoIs3.mov, respectively (available in [**48**], and at [**91**]).

To characterize the ordering process taking place in the evolution of the patterns we calculate the spectral pattern entropy $S = \sum_{i,j} p_{ij} \ln p_{ij}$, where $p_{ij} = \tilde{p_{ij}}/(\sum_{i,j} \tilde{p}_{ij})$ is the normalized power in the Fourier mode with amplitude $\tilde{p}_{ij}$ and the sum includes all modes within the critical annulus binned into 10° segments. The entropy allows an estimate of the effective number of Fourier modes e^S contributing to the pattern. Using this spectral pattern entropy rather than counting modes in a pattern's Fourier transform at a given time step allows us to understand trends and tendencies as a pattern evolves in time. Fig.9.4 illustrates the temporal evolution of e^S for different values of the 3:1 forcing

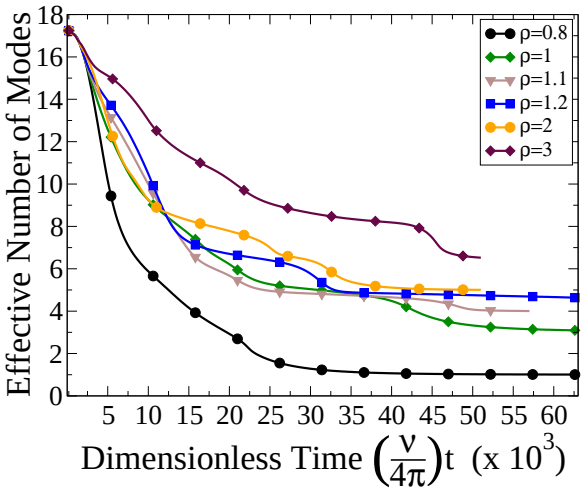

Figure 9.4. Effective number of Fourier modes e^S plotted as a function of time for different values of the 3:1 forcing strength ρ. Data taken from numerical simulations of (6.3) for parameters as in Fig.7.1b (case $K = 2$) with $\alpha = -1$, $\Phi = 3\pi/4$.

strength ρ. The number of significant modes increases with ρ, although not monotonically for all times: for example, the curves corresponding to $\rho = 1$ and $\rho = 1.2$ cross several times, near dimensionless times $\nu t/4\pi = 12 \times 10^3, 17 \times 10^3, 35 \times 10^3$, before beginning to converge smoothly to $e^S \approx 3$ and 4, respectively. While the decrease in the effective number of Fourier modes with time in the transients is monotonic it occurs in spurts. For $\rho = 3$, for instance, there is a sudden dip near dimensionless time $\nu t/4\pi = 45 \times 10^3$. These dips are related to the sudden disappearance of modes that is apparent in the time evolution plots Fig.9.2a-e.

The complex Ginzburg-Landau equation (6.3) describes the evolution of the oscillation amplitude on a slow time. The full time evolution of the underlying system involves also the Hopf frequency. To illustrate the full time dependence the movie SimulationOver2Periods_withFastOscs.mov (available in [**48**]) shows the evolution of the pattern over two forcing periods obtained for $\rho = 2$ as one might see it in an experiment. Fig.9.5

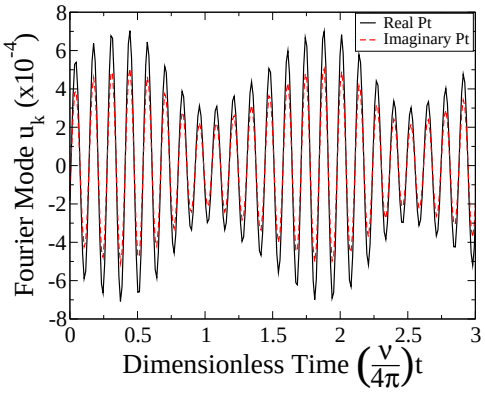

Figure 9.5. Temporal evolution of the real and imaginary parts of one of the spatial Fourier modes of the pattern shown in Fig.9.3e and in the movie SimulationOver2Periods_withFastOscs.mov (available in [**48**]).

shows the corresponding temporal evolution of the real and imaginary parts of one of the spatial Fourier modes. The beating reflects the quasi-periodic forcing of the system. Details about the quantity shown in the movie SimulationOver2Periods_withFastOscs.mov (available in [**48**]) and in Fig.9.5 are given in the Appendix.

CHAPTER 10

Conclusion

10.1. Conclusion for Part 2

We have demonstrated analytically and confirmed numerically that in systems near a Hopf bifurcation to spatially uniform oscillations, forcing with judiciously chosen waveforms can stabilize complex periodic and quasi-periodic patterns comprised of up to 4 and 5 Fourier modes. Essential for the success of this approach was the use of a quasi-periodic forcing function in which the frequency content near twice the Hopf frequency consists of two frequencies; thus, the forcing is slowly modulated in time. The choice of forcing function was motivated by Part 1. There we showed that, according to the cubic-order weakly nonlinear description, super-hexagon patterns are stable on the upper branch of a transcritical bifurcation. But through numerical simulations we showed that, on that upper branch, the amplitudes are too large and so the weakly nonlinear analysis taken to cubic order is not sufficient to describe the resulting patterns. With forcing modulated in time, since the investigated complex patterns are subharmonic in time with respect to that modulation, they arise in a pitchfork bifurcation and are amenable to a weakly nonlinear analysis. The stabilization of the complex patterns was achieved by exploiting resonant triad interactions that result from an additional forcing component with a frequency close to three times the Hopf frequency.

As expected from investigations in the context of the Faraday system [**32**, **38**, **41**–**43**, **45**], our weakly nonlinear analysis showed that the resonant triad interaction can significantly modify the competition between Fourier modes of different orientation through the excitation of weakly damped modes as shown in Fig.7.1. This damping is controlled by the differences in frequency and by the amplitude of the two forcing components near twice the Hopf frequency. Excitation of the weakly damped modes is controlled by the $3:1$-forcing $\rho e^{i\Phi}$. For sufficiently small damping the phase Φ can be chosen such that the self-coupling of the modes is significantly enhanced, which effectively reduces the competition between modes over a quite wide range of angles subtended by those modes. As in the Faraday system, this stabilizes complex patterns in the forced oscillatory systems investigated here. Alternatively, the forcing can be chosen to either suppress or enhance, depending on the phase Φ, the competition between modes differing in their orientation by a quite specific angle θ_r, which can be tuned over quite some range. In the Faraday system this approach, with suppression of competition between modes, can also lead to complex 4-mode patterns, which effectively consist of the combination of two square patterns that are rotated by an angle close to θ_r. In the forced oscillatory systems investigated here this mechanism alone does not yield complex patterns since in the unforced system squares are never stable, while in the Faraday system square patterns are stable for low viscosity [**12**, **31**, **41**]. Thus, in the present context this mechanism only leads to the stabilization of rectangle patterns. For sufficiently strong forcing their bifurcation can even be made subcritical, even though the stripe patterns (and the Hopf bifurcation itself) are supercritical.

We have complemented the weakly nonlinear analysis by direct simulations of the extended complex Ginzburg-Landau equation in large domains to study the competition between different, linearly stable, complex patterns. As expected from the variational character of the amplitude equations and the relationship between the energy of the various patterns and the forcing strength ρ, we find that as the resonant triad interaction is increased more complex patterns dominate over simpler patterns. For the parameters chosen in the numerical simulations we find patterns with 4-fold symmetric elements reminiscent of super-squares and anti-squares [**92**] as well as 5-fold symmetric elements. The weakly nonlinear analysis (see Fig.8.3b) suggests that for other system parameters patterns comprised of yet more modes could be stable.

It should be noted that we reached the regime in which complex patterns are stable by tuning the amplitudes and phases of the forcing function, which constitute external forcing parameters. Therefore we expect that the complex patterns should be accessible quite generally in forced oscillatory systems, in particular also in chemical oscillators [**25**,**28**,**79**]. Specifically, our weakly nonlinear analysis indicates that the dependence of the patterns on the nonlinear dispersion coefficient α of the unforced system can be compensated by the strength of the forcing close to three times the Hopf frequency (cf. Fig.8.3b). Moreover, for the parameters determined experimentally in the oscillatory Belousov-Zhabotinsky reaction [**84**] we have shown explicitly that moderate forcing strengths are sufficient to stabilize 4-mode patterns. It should be noted, however, that the complex patterns possibly arise only very close to onset. Therefore the application of our results to experiments may require systems with relatively large aspect ratios and a very careful tuning of the forcing parameters.

To characterize the temporal evolution of the patterns starting from random initial conditions and to distinguish the resulting patterns quantitatively we used the spectral entropy of the patterns, which quantifies the effective number of Fourier modes of the patterns. It allowed a clear distinction between patterns with three, four, or more significant modes. However a more detailed quantitative characterization of the transients that captures also the competition between multi-mode structures like super-squares and anti-squares, which have the same number of participating modes, is still an open problem (cf. [**93**]). The long-time scaling of the ordering process of such complex structures and a comparison with the ordering in stripe [**94**, **95**] or hexagon patterns [**96**] may also be interesting to study. Most likely, the number of different types of defects and their mutual interaction may play an important role. However, for the subharmonic patterns discussed here the amplitude equations do not contain any terms of even order. Therefore, the strong interaction between defects that is associated with those terms and that should make their dynamics in particular interesting in the case of 5-mode patterns [**97**] will not be present here.

10.2. Future Directions

We foresee many possible extensions of the work presented in this dissertation. First, to obtain the results we discussed restrictions were placed on the forcing. Specifically we fixed the tuning of the 3:1-resonant forcing to remove the time-dependence in the CGLE from the $\bar{A}^2$ term and we set the 1:1-resonant forcing so that the CGLE has no inhomogeneous terms (see Chaps.3,6). Relaxing these restrictions may result in different and interesting behaviour. In particular relaxing the restriction on the 1:1-resonant forcing

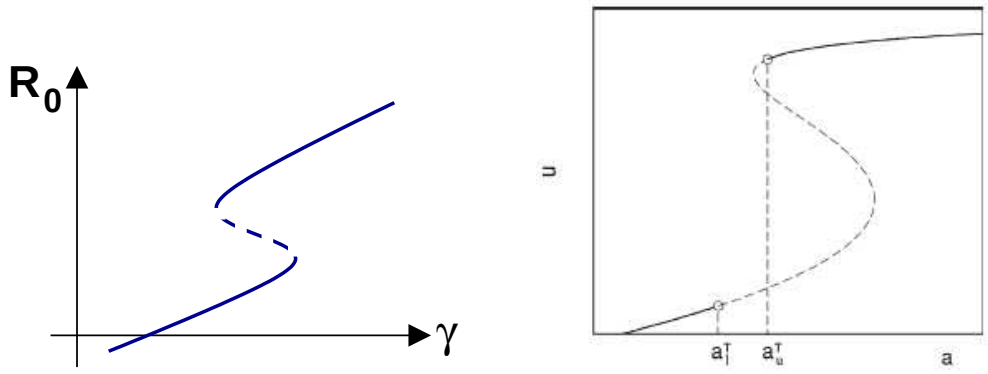

(a) (b)

Figure 10.1. Steady state solutions exhibiting bistability. (a) Possible steady state solution to the CGLE for general 1:1 resonant forcing, $A = 0$ is no longer a solution. (b) Steady state solution to for the Fitzhugh-Nagumo equation in [**98**] exhibiting simultaneous Turing instabilities of the both stable states, where u represents the solution amplitude, a is the control parameter, and a_l^T and a_u^T represent the onset of the Turing instability of the lower and upper branches respectively.

changes the steady state in a fundamental way - the solution $A = 0$ is not a solution to the CGLE with inhomogeneous terms. Instead the steady state's dependence on the forcing may look like Fig.10.1a, for $A = R_0 e^{i\phi}$ [**23**] with stable states appearing and disappearing in saddle node bifurcations. In this case there may be bistability of stable states if the upper and lower branches represent the stable branches, which leads to hysteresis between the states. Further, in [**98**, **99**], Dewel et al. discuss the formation of patterns in a reaction-diffusion system with similar bistable steady state through simultaneous or nearby Turing instabilities off the lower and upper branches, see Fig.10.1b. The simultaneous instabilities create two different length scales and thus generate resonant rhombic patterns [**99**], superlattice patterns, or quasi-patterns [**98**, **99**]. It may be that complex patterns may similarly arise in the CGLE with an inhomogeneous term and a bistable steady state, through simultaneous or nearby dispersive-type instabilities [**24**].

We considered the case where the detunings ν_{21} and ν_{22} of the 2:1-forcing have the same sign. It would also be interesting to consider the case where their signs are opposite, so that one of the detunings is just above the Hopf frequency, and the other just below. Then only one of the two forcing terms will yield a pattern-forming instability [**24**], while the other term will induce a phase-locking of spatially homogeneous oscillations. The result of the interaction between these two instabilities is not known.

We also did not explore the subcritical cases $b_0 < 0$ or $b(\theta)/b_0 < -1$. The weakly nonlinear analysis to cubic order is insufficient to make predictions about pattern selection in these cases. Fig.8.6, suggests that for $K = 2\cos(\tan^{-1}(2/5))$ large-amplitude rectangle patterns with θ close to $\theta_r = \tan^{-1}(2/5)$ could be stabilized by the forcing.

We achieved the stabilization of complex patterns by exploiting a single weakly damped spatial mode. As Fig.7.1 shows there is a sequence of local minima indicating instabilities to a harmonic mode, given by the linear stability analysis. It would be interesting to try to tune parameters so that there are two or more weakly damped harmonic modes. A wider variety of complex patterns may then be possible, by suppressing competition for specific ranges in the angle, as has been done in Faraday wave systems by employing multi-frequency forcing [**100**].

In a similar vein, it may be possible to tune parameters so that a spatially homogeneous mode is weakly damped at the onset of instability to a symmetry-breaking subharmonic mode with wave number $k_c^{(S)}$. Increasing the forcing strength γ so that both these modes are excited could lead to qualitatively different solutions than those shown here. This situation is addressed in [**101**]. They show that, in the case where the original system has up-down symmetry (so the pattern amplitude equations have no quadratic terms),

coupling between a symmetry-breaking mode and the zero mode leads to stable mixed states made up of hexagons, stripes, and a spatially homogeneous mode. In the case where the up-down symmetry is broken, the coupling can also lead to stable reentrant hexagons. For the modulated forcing presented in Part 2 of this dissertation, the spatially homogeneous mode can oscillate either subharmonically or harmonically; any coupling between the zero mode and a symmetry-breaking subharmonic mode depends on the nature of the zero mode. Thus, in the regime where a zero mode is weakly damped at the onset of instability to a symmetry-breaking subharmonic mode, simultaneously exciting both modes may lead to mixed states similar to those presented in [**101**], or patterns with more or less complexity dictated by the interaction between the oscillating modes.

Finally, here our focus was on systems below the Hopf bifurcation ($\mu < 0$). It would be interesting to pursue a similar study above the Hopf bifurcation. There the spontaneous oscillations, which do not arise in the Faraday system, and their competition with phase-locked patterns driven by the forcing may lead to additional complexity. For single-frequency forcing near 2:1 resonance labyrinthine stripe patterns are found to arise from the oscillations through front instabilities and stripe nucleation away in the parameter regime where, without forcing, there is no Benjamin-Feir instability [**79**]. If there is a Benjamin-Feir instability, which in the unforced regime can lead to defect-mediated turbulence, its interaction with the stabilizing influence of the forcing may give rise to labyrinthine stripe patterns or hexagon patterns [**23**, **78**]. It is unknown what happens if the stripes or hexagons are unstable to the more complex patterns discussed here.

We performed a few preliminary numerical simulations above the Hopf bifurcation with modulated 2:1-resonant forcing and varying 3:1-resonant forcing strength to get a

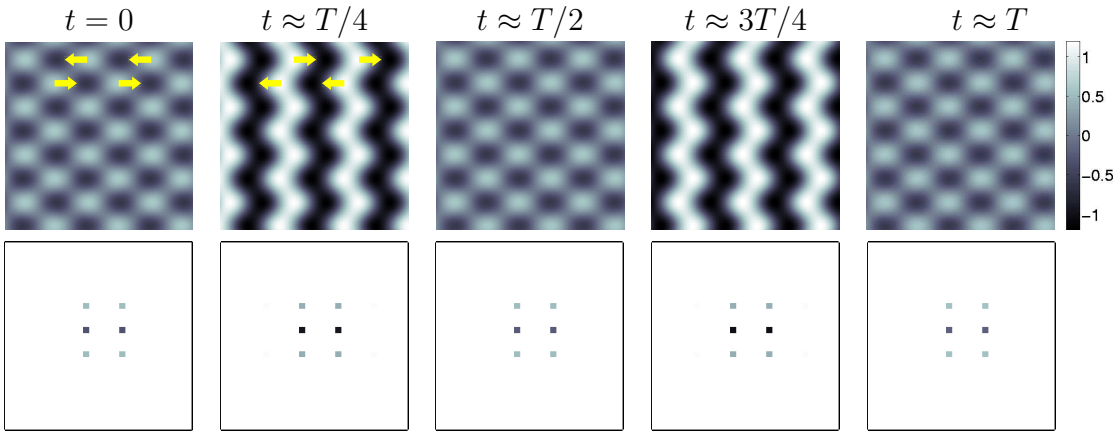

Figure 10.2. Small-system numerical simulations of (6.3) in a square domain, $L = 2\pi/(\cos(\tan^{-1}(1/2))k^{(SH)} \approx 13.13$, with $\mu = 0.1$ for 3:1 forcing strength $\rho = 0$. Snapshots taken over one period $T = 4\pi/\nu$. Other parameters as in Fig.7.1b (case $K = 2$) with $\alpha = -1$, $\Phi = 3\pi/4$.

preview of what may happen. We used the minimal domain size for a 4-mode pattern as described in Section 9.1 and simulation parameters are the same as those used in Chapter 9 except for the distance from the Hopf bifurcation μ for which we chose $\mu = 0.1$. Figs.10.2, 10.3, and 10.4 show snapshots from these simulations and the corresponding Fourier transform for increasing values of 3:1-forcing ρ, $\rho = 0, 1, 2$ respectively.

We observe after some transient behaviour interesting breathing patterns, which persist from $t = 100$ to the end of our simulations at $t = 500$; these patterns could represent a slowly-varying transient or an unstable solution. Specifically, for $\rho = 0$ in Fig.10.2 the columns of white dots appear to move back and forth horizontally, adjacent rows moving in opposite directions, as indicated by the yellow arrows for $t = 0$ and $t \approx T/4$. For $\rho = 1$ in Fig.10.3, the diagonal rows of black dots move back and forth in a direction perpendicular to the rows, again with adjacent rows moving in opposite directions, as indicated by the yellow arrows for $t = 0$ and $t \approx T/4$. And for $\rho = 2$ in Fig.10.4 the black dots seen for

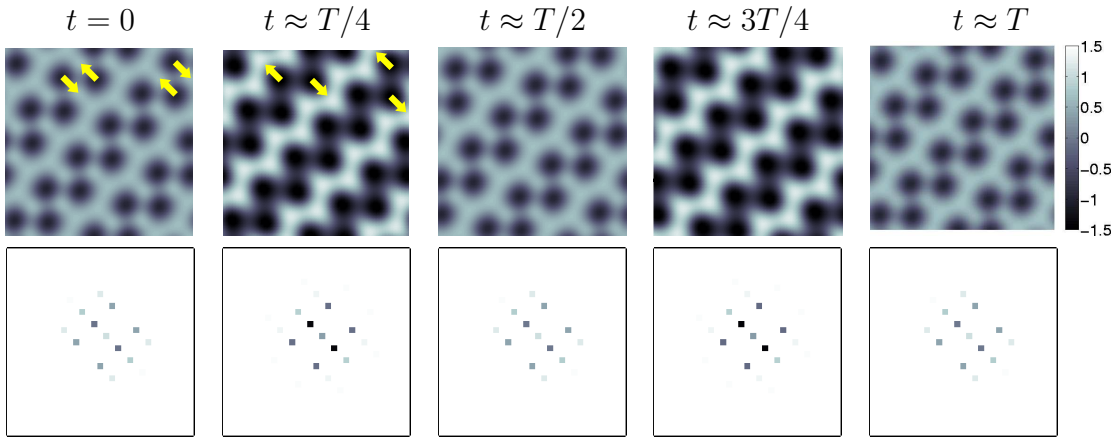

Figure 10.3. Small-system numerical simulations of (6.3) in a square domain, $L = 2\pi/(\cos(\tan^{-1}(1/2))k^{(SH)} \approx 13.13$, with $\mu = 0.1$ for 3:1 forcing strength $\rho = 1$. Snapshots taken over one period $T = 4\pi/\nu$. Other parameters as in Fig.7.1b (case $K = 2$) with $\alpha = -1$, $\Phi = 3\pi/4$.

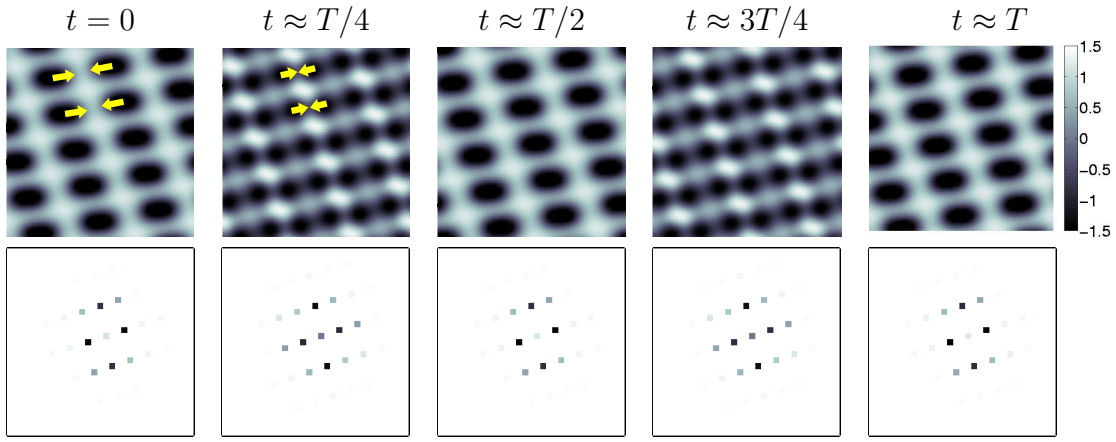

Figure 10.4. Small-system numerical simulations of (6.3) in a square domain, $L = 2\pi/(\cos(\tan^{-1}(1/2))k^{(SH)} \approx 13.13$, with $\mu = 0.1$ for 3:1 forcing strength $\rho = 2$. Snapshots taken over one period $T = 4\pi/\nu$. Other parameters as in Fig.7.1b (case $K = 2$) with $\alpha = -1$, $\Phi = 3\pi/4$.

$t = 0$, split and move apart in a direction perpendicular to the row as seen for $t \approx T/4$, and join with a split off dot from the adjacent row to form a new black dot as seen for

$t \approx T/2$; that dot then splits again. The period of this breathing behaviour is approximately $T = 4\pi/\nu$, suggesting a subharmonic response to the modulation of the forcing. The time-dependent behaviour is also apparent in the corresponding Fourier transforms in Figs.10.2, 10.3, and 10.4: the amplitudes of Fourier modes increase and decrease throughout the period. As with our results presented in Chaps.8 and 9 complexity of the patterns seems to increase with ρ. Notice for $\rho = 0$ in Fig.10.2, the Fourier transform shows 3 nonzero modes and their complex conjugates with increasing and decreasing amplitude. For $\rho = 1$ in Fig.10.3 the Fourier transform shows 3 nonzero modes and their complex conjugates with increasing and decreasing amplitude in the same relative orientation as the 3 nonzero modes for $\rho = 0$, with a few additional modes that appear and disappear. For $\rho = 2$ in Fig.10.4 the Fourier transform shows 4, not 3, modes and their complex conjugates with increasing and decreasing amplitude, and a few additional modes that appear and disappear. These intriguing test simulations suggest that further study in the regime above the Hopf bifurcation could yield some very interesting results.

References

[1] T. Aste and U. Valbusa. Ripples and ripples: from sandy deserts to ion-sputtered surfaces. *New Journal of Physics*, 7:122, May 2005.

[2] H. Bénard. Les tourbillons cellulaires dans une nappe liquide. *Rev. Gen. Sci. Pures Appl.*, 1900.

[3] M.C. Cross and P.C. Hohenberg. Pattern formation outside of equilibrium. *Reviews of Modern Physics*, 65:851–1123, 1993.

[4] Daniel Walgraef. *Spatio-Temporal Pattern Formation*. Springer-Verlag New York, Inc., 1997.

[5] D. Shechtman, I. Blech, D. Gratias, and J. Cahn. Metallic phase with long-range orientational order and no translational symmetry. *Physical Review Letters*, 53:1951, 1984.

[6] P.J. Lu and P.J. Steinhardt. Decagonal and quasi-crystalline tilings in medieval Islamic architecture. *Science*, 315:1106–1110, 2007.

[7] H.-K Ko, J. Lee, and K. J. Lee. Subharmonic bifurcations of standing wave lattices in a driven ferrofluid system. *Physical Review E*, 65:056222, 2002.

[8] M. Faraday. On a peculiar class of acoustical figures; and on certain forms assumed by groups of particles upon vibrating elastic surfaces. *Philosophical Transactions of the Royal Society of London*, 121:299–340, 1831.

[9] B. Christiansen, P. Alstrom, and M. T. Levinsen. Ordered capillary-wave states - quasi-crystals, hexagons, and radial waves. *Physical Review Letters*, 68(14):2157–2160, April 1992.

[10] W. S. Edwards and S. Fauve. Parametrically excited quasi-crystalline surface-waves. *Physical Review E*, 47(2):R788–R791, February 1993.

[11] W. S. Edwards and S. Fauve. Patterns and quasi-patterns in the Faraday experiment. *Journal of Fluid Mechanics*, 278:123, 1994.

[12] A. Kudrolli and J.P. Gollub. Localized spatiotemporal chaos in surface waves. *Physical Review E*, 54:1052, 1996.

[13] A. Kudrolli, B. Pier, and J.P. Gollub. Superlattice patterns in surface waves. *Physica D*, 123:99, 1998.

[14] H. Arbell and J. Fineberg. Two-mode rhomboidal states in driven surface waves. *Physical Review Letters*, 84(4):654–657, January 2000.

[15] H. Arbell and J. Fineberg. Pattern formation in two-frequency forced parametric waves. *Physical Review E*, 65:036224, 2002.

[16] M.-T. Westra, D. J. Binks, and W. van de Water. Patterns of Faraday waves. *Journal of Fluid Mechanics*, 496:1, 2003.

[17] Y. Ding and P. Umbanhowar. Enhanced Faraday pattern stability with three-frequency driving. *Physical Review E*, 73:046305, 2006.

[18] H. Chaté and P. Manneville. Phase diagram of the two-dimensional complex Ginzburg-Landau equation. *Physica A*, 224:348, 1996.

[19] Q. Ouyang and J. M. Flesselles. Transition from spirals to defect turbulence driven by a convective instability. *Nature*, 379(6561):143–146, January 1996.

[20] A. L. Belmonte, Qi Ouyang, and J. M. Flesselles. Experimental survey of spiral dynamics in the Belousov-Zhabotinsky reaction. *Journal de Physique II (Paris)*, 7:1425–1468, 1997.

[21] I. S. Aranson and L. Kramer. The world of the complex Ginzburg-Landau equation. *Reviews of Modern Physics*, 74:99, 2002.

[22] S. Madruga, H. Riecke, and W. Pesch. Defect chaos and bursts: Hexagonal rotating convection and the Complex Ginzburg-Landau equation. *Physical Review Letters*, 96:074501, 2006.

[23] P. Coullet and K. Emilsson. Strong resonances of spatially distributed oscillators: a laboratory to study patterns and defects. *Physica D*, 61:119, 1992.

[24] P. Coullet, T. Frisch, and G. Sonnino. Dispersion-induced patterns. *Physical Review E*, 49:2087, 1994.

[25] V. Petrov, Q. Ouyang, and H. L. Swinney. Resonant pattern formation in a chemical system. *Nature*, 388(6643):655–657, August 1997.

[26] A. L. Lin, M. Bertram, K. Martinez, H. L. Swinney, A. Ardelea, and G. F. Carey. Resonant phase patterns in a reaction-diffusion system. *Physical Review Letters*, 84(18):4249–4253, May 2000.

[27] A. L. Lin, A. Hagberg, A. Ardelea, M. Bertram, H. L. Swinney, , and E. Meron. Four-phase patterns in forced oscillatory systems. *Physical Review E*, 62(3):3790–3798, September 2000.

[28] A.L. Lin, A. Hagberg, E. Meron, and H.L. Swinney. Resonance tongues and patterns in periodically forced reaction-diffusion systems. *Physical Review E*, 69:066217, 2004.

[29] M. Dolnik, I. Berenstein, A. M. Zhabotinsky, and I. R. Epstein. Spatial periodic forcing of Turing structures. *Physical Review Letters*, 87(23):238301, December 2001.

[30] I. Berenstein, L. Yang, M. Dolnik, A. M. Zhabotinsky, , and I. Epstein. Superlattice Turing structures in a photosensitive reaction-diffusion system. *Physical Review Letters*, 91(5):058302, August 2003.

[31] W. Zhang and J. Viñals. Square patterns and quasi-patterns in weakly damped Faraday waves. *Physical Review E*, 53:4283, 1996.

[32] M. Silber, C. M. Topaz, and A. C. Skeldon. Two-frequency forced Faraday waves: Weakly damped modes and pattern selection. *Physica D*, 143(1-4):205–225, September 2000.

[33] J. Porter, C. M. Topaz, and M. Silber. Pattern control via multifrequency parametric forcing. *Physical Review Letters*, 93(3):034502, July 2004.

[34] N. D. Mermin and S. M. Troian. Mean-field theory of quasicrystalline order. *Physical Review Letters*, 54:1524, 1985.

[35] B. Malomed, A. A. Nepomnyashchy, and M. I. Tribelsky. Two-dimensional quasiperiodic structures in nonequilibrium systems. *Soviet Physics JETP*, 69:388, 1989.

[36] A. C. Newell and Y. Pomeau. Turbulent crystals in macroscopic systems. *Journal of Physics A*, 26(8):L429–L434, April 1993.

[37] J. Porter and M. Silber. Resonant triad dynamics in weakly damped Faraday waves with two-frequency forcing. *Physica D*, 190:93–114, 2004.

[38] J. Porter, C. M. Topaz, and M. Silber. Faraday wave pattern selection via multi-frequency forcing. *Physical Review E*, 93:034502, 2004.

[39] A. M. Rucklidge and M. Silber. Quasipatterns in parametrically forced systems. *Physical Review E*, 75:055203, 2007.

[40] A. M. Rucklidge and M. Silber. Design of parametrically forced patterns and quasi-patterns. *Preprint*, 2008.

[41] P. L. Chen and J. Viñals. Pattern selection in Faraday waves. *Physical Review Letters*, 79(14):2670–2673, October 1997.

[42] W. Zhang and J. Viñals. Pattern formation in weakly damped parametric surface waves. *Journal of Fluid Mechanics*, 336:301, 1997.

[43] W. Zhang and J. Viñals. Pattern formation in weakly damped parametric surface waves driven by two frequency components. *Journal of Fluid Mechanics*, 341:225, 1997.

[44] W. Zhang and J. Viñals. Numerical study of pattern formation in weakly damped parametric surface waves. *Physica D*, 116:225, 1998.

[45] P. Chen and J. Viñals. Amplitude equations and pattern selection in Faraday waves. *Physical Review E*, 60:559, 1999.

[46] J. M. Conway and H. Riecke. Multiresonant forcing of the complex Ginzburg-Landau equation: Pattern selection. *Physical Review E*, 76:057202, 2007.

[47] J .M. Conway and H. Riecke. Quasi-patterns in a model of chemical oscillations forced at multiple resonant frequencies. *Physical Review Letters*, 99:218301, 2007.

[48] J .M. Conway and H. Riecke. Superlattice patterns in the complex ginzburg-landau equation with multi-resonant forcing. *SIAM Journal of Applied Dynamical Systems*, submitted.

[49] F. Sagues and I. R. Epstein. Nonlinear chemical dynamics. *Dalton transactions*, (7):1201–1217, 2003.

[50] I. R. Epstein, J. A. Pojman, and O. Steinbock. Introduction: Self-organization in nonequilibrium chemical systems. *Chaos*, 16(3):037101, September 2006.

[51] A. De Wit. Spatial patterns and spatiotemporal dynamics in chemical systems. *Advances in chemical physics, Vol 109*, 109:435–513, 1999.

[52] I.R. Epstein and J.A. Pojman. *An introduction to nonlinear chemical dynamics: oscillations, waves, patterns, and chaos*. New York: Oxford University Press, 1998.

[53] W.C. Bray. A periodic reaction in homogeneous solution and its relation to catalysis. *Journal of the American Chemical Society*, 43:1262, 1921.

[54] W.C. Bray and H.A. Liebhafsky. Reactions involving hydrogen peroxide, iodine and iodate ion. i. introduction. *Journal of the American Chemical Society*, 53:38, 1931.

[55] K. R. Sharma and R. M. Noyes. Oscillations in chemical systems .13. detailed molecular mechanism for bray-liebhafsky reaction of iodate and hydrogen-peroxide. *Journal Of The American Chemical Society*, 98(15):4345–4361, 1976.

[56] A. N. Zaikin and A.M. Zhabotinsky. Concentration wave propagation in a 2-dimensional liquid-phase self-oscillating system. *Nature*, 225(5232):535–&, 1970.

[57] I. Prigogine and G. Nicolis. On symmetry-breaking instabilities in dissipative systems. *Journal of Chemical Physics*, 46:3542, 1967.

[58] I. Prigogine and R. Lefever. Symmetry breaking instabilities in dissipative systems. ii. *Journal of Chemical Physics*, 48:1695, 1968.

[59] R. J. Field, R. M. Noyes, and E. Körös. Oscillations in chemical systems .2. thorough analysis of temporal oscillation in bromate-cerium-malonic acid system. *Journal Of The American Chemical Society*, 94(25):8649–&, 1972.

[60] R. M. Noyes, R. J. Field, and E. Körös. Oscillations in chemical systems .1. detailed mechanism in a system showing temporal oscillations. *Journal Of The American Chemical Society*, 94(4):1394–&, 1972.

[61] A. T. Winfree. Spiral waves of chemical activity. *Science*, 175(4022):634–&, 1972.

[62] A.M. Turing. The chemical basis of morphogenesis. *Philosophical Transactions of the Royal Society of London. Series B, Biological Sciences.*, 237(641):37–72, August 1952.

[63] P. Borckmans, G. Dewel, A. De Wit, E. Dulos, J. Boissonade, F. Gauffre, and P. De Kepper. Diffusive instabilities and chemical reactions. *International journal of bifurcation and chaos*, 12(11):2307–2332, November 2002.

[64] V. Castets, E. Dulos, J. Boissonade, and P. De Kepper. Experimental evidence of a sustained standing Turing-type pattern. *Physical Review Letters*, 64(24):2953–2956, 1990.

[65] P. De Kepper, I. R. Epstein, K. Kustin, and M. Orban. Batch oscllllatlons and spatial wave patterns in chlorite oscillating systems. *Journal of Physical Chemistry*, 86:170–171, 1982.

[66] I. Lengyel and I. R. Epstein. Modeling of Turing structures in the chlorite-iodide-malonic acid-starch reaction system. *Science*, 251:650–652, 1991.

[67] Q. Ouyang and H. L. Swinney. Transition from a uniform state to hexagonal and striped Turing patterns. *Nature*, 352(6336):610–612, 1991.

[68] A. K. Horvath, M. Dolnik, A. P. Munuzuri, A. M. Zhabotinsky, and I. R. Epstein. Control of Turing structures by periodic illumination. *Physical Review Letters*, 83(15):2950–2952, October 1999.

[69] I. Lengyel and I. R. Epstein. A chemical approach to designing Turing patterns in reaction-diffusion systems. *Proceedins of the National Academy of Sciences*, 89:3977–3979, 1992.

[70] A. P. Munuzuri, M. Dolnik, A. M. Zhabotinsky, and I. R. Epstein. Control of the chlorine dioxide-iodine-malonic acid oscillating reaction by illumination. *Journal Of The American Chemical Society*, 121:8065–8069, 1999.

[71] I. Berenstein, L. F. Yang, M. Dolnik, A. M. Zhabotinsky, and I. R. Epstein. Dynamic mechanism of photochemical induction of Turing superlattices in the chlorine dioxide-iodine-malonic acid reaction-diffusion system. *Journal of Physical Chemistry*, 109:5382–5387, 2005.

[72] A. L. Lin, M. Bertram, K. Martinez, H. L. Swinney, A. Ardelea, and G. F. Carey. Resonant phase patterns in a reaction-diffusion system. *Physical Review Letters*, 84(18):4240–4243, May 2000.

[73] A. L. Lin, A. Hagberg, E. Meron, and H. L. Swinney. Resonance tongues and patterns in periodically forced reaction-diffusion systems. *Physical Review E*, 69(6):066217, June 2004.

[74] A. Hagberg and E. Meron. Complex patterns in reaction-diffusion systems: A tale of two front instabilities. *Chaos*, 4:477–484, 1994.

[75] B. Marts, A. Hagberg, E. Meron, and A. L. Lin. Resonant and nonresonant patterns in forced oscillators. *Chaos*, 16(3):037113, September 2006.

[76] J. Kim, J. Lee, and B. Kahng. Harmonic forcing of an extended oscillatory system: Homogeneous and periodic solutions. *Physical Review E*, 65(4):046208, April 2002.

[77] J. Kim, J. Lee, and B. Kahng. Responses of the complex Ginzburg-Landau equation under harmonic forcing. *Physica A*, 315(1-2):330–341, November 2002.

[78] K. Zhang, H. L. Wang, C. Qiao, and Q. Ouyang. Hexagonal standing-wave patterns in periodically forced reaction-diffusion systems. *Chinese physics letters*, 23(6):1414–1417, June 2006.

[79] A. Yochelis, A. Hagberg, E. Meron, A. L. Lin, and H. L. Swinney. Development of standing-wave labyrinthine patterns. *SIAM Journal of Applied Dynamical Systems*, 1:236, 2002.

[80] A.H. Nayfeh. *Perturbation Methods*. Wiley-VCH Verlag GmbH & Co. KGaA, 2004.

[81] H. Riecke, J. D. Crawford, and E. Knobloch. Time-modulated oscillatory convection. *Physical Review Letters*, 61:1942, 1988.

[82] S. L. Judd and M. Silber. Simple and superlattice Turing patterns in reaction-diffusion systems: bifurcation, bistability, and parameter collapse. *Physica D*, 136(1-2):45–65, February 2000.

[83] M. Silber and M. R. E. Proctor. Nonlinear competition between small and large hexagonal patterns. *Physical Review Letters*, 81(12):2450–2453, September 1998.

[84] F. Hynne and P. G. Sørensen. Experimental determination of Ginzburg-Landau parameters for reaction-diffusion systems. *Physical Review E*, 48:4106–4109, 1993.

[85] D.W. Jordan and P. Smith. *Nonlinear Ordinary Differential Equations, An Introduction to Dynamical Systems*. Oxford University Press, 3 edition, 1999.

[86] K. Kumar and L. S. Tuckerman. Parametric instability of the interface between two fluids. *Journal of Fluid Mechanics*, 279:49, 1994.

[87] A. M. Rucklidge and W. J. Rucklidge. Convergence properties of the 8, 10, and 12 mode representations of quasipatterns. *Physica D*, 178:62, 2003.

[88] Y. Pomeau. Front motion, metastability and subcritical bifurcations in hydrodynamics. *Physica D*, 23:3, 1986.

[89] D. Boyer and J. Viñals. Grain boundary pinning and glassy dynamics in stripe phases. *Physical Review E*, 65(4):046118, April 2002.

[90] H. Müller. Periodic triangular patterns in the Faraday experiment. *Physical Review Letters*, 71:3287, 1993.

[91] http://people.esam.northwestern.edu/ riecke/research/modcgl/modcgl.html.

[92] B. Dionne, M. Silber, and A. C. Skeldon. Stability results for steady, spatially periodic planforms. *Nonlinearity*, 10(2):321–325, March 1997.

[93] H. Riecke and S. Madruga. Geometric diagnostics of complex patterns: Spiral-defect chaos. *Chaos*, 16:013125, 2006.

[94] C. Harrison, D. H. Adamson, Z. D. Cheng, J. M. Sebastian, S. Sethuraman, D. A.Huse, R. A. Register, and P. M. Chaikin. Mechanisms of ordering in striped patterns. *Science*, 290:1558–1560, 2000.

[95] D. Boyer and J. Viñals. Domain coarsening of stripe patterns close to onset. *Physical Review E*, 6405(5):050101, November 2001.

[96] C. Sagui and R. C. Desai. Late-stage kinetics of systems with competing interactions quenched into the hexagonal phase. *Physical Review E*, 52(3):2807–2821, September 1995.

[97] B. Echebarria and H. Riecke. Sideband instabilities and defects of quasipatterns. *Physica D*, 158:45, 2001.

[98] G. Dewel, M. Bachir, P. Borckmans, and S. Métens. Super-réseaux et quasi-crystaux dans les systemes bistables. *C.R. Acad. Sci. Paris*, 329(IIb), 2001.

[99] G. Dewel, M. Bachir, S. Métens, and P. Borckmans. Pattern formation and spatial self-entrainment in bistable chemical systems. *Faraday Discussions*, 120:363–370, 2002.

[100] C. Topaz, J. Porter, and M. Silber. Multifrequency control of Faraday wave patterns. *Physical Review E*, 70(6 Pt.2):066206, December 2004. A qualitative effect on the system may also be produced through differences in the forcing frequencies, cf.

[101] G. Dewel, S. Métens, M'F. Hilali, P. Borckmans, and C.B. Price. Resonant patterns through coupling with a zero mode. *Physical Review Letters*, 74:4647–4650, 1995.

APPENDIX

Deriving the CGLE from the Brusselator

In Section 6 we derived the form of the extended CGLE (6.3) based on symmetry arguments. To illustrate that the additional terms arise from a general forcing function in a natural way we derive the coefficients of the equation here for the Brusselator, which often has served as a simple model for chemical oscillations [**27**]. With the forcing included, it can be written as

$$\begin{aligned}\frac{\partial u}{\partial \tilde{t}} &= 1-(1+B)u+D_u\Delta u+\big(1+f_1\sin((1+\nu_1)\tilde{t})+f_3\sin((3+\nu_3)t) \qquad (.1)\\ &\quad +f_2(\cos(\chi)\sin((2+\nu_{21})\tilde{t})+\sin(\chi)\sin((2+\nu_{22})\tilde{t}))\big)\,u^2v,\\ \frac{\partial v}{\partial \tilde{t}} &= Bu+D_v\Delta v-u^2v, \qquad (.2)\end{aligned}$$

where u and v represent two reacting and diffusing chemical species. In the formulation (.1,.2), which differs slightly from the form presented in [**27**] in the coefficients of the linear terms, the Hopf bifurcation occurs at $B=2$ and the Hopf frequency is given by $\omega=1$. The forcing near the Hopf frequency is given by $f_1\sin((1+\nu_1)\tilde{t})u^2v$, the modulated forcing near twice the Hopf frequency by $f_2(\cos(\chi)\sin((2+\nu_{21})\tilde{t})+\sin(\chi)\sin((2+\nu_{22})\tilde{t}))u^2v$, and the forcing near three times the Hopf frequency by $f_3\sin((3+\nu_3)t)u^2v$. The small parameters $\nu_j=O(\delta^2)$, $\delta\ll 1$, represent the detuning (cf. eqs.(3.3,6.1)), the parameters $f_1\equiv\delta^3\hat{f}_1$, $f_2\equiv\delta\hat{f}_2$, and $f_3\equiv\delta\hat{f}_3$ represent the small 1:1-, 1:2-, and 1:3 forcing strengths with $\hat{f}_j=\mathcal{O}(1)$, and the parameters D_u and D_v are the diffusion coefficients. To derive

the extended CGLE (6.3) we expand (.1,.2) near the Hopf bifurcation about the basic state $(u, v) = (1, B)$ as

$$\begin{pmatrix} u \\ v \end{pmatrix} = \begin{pmatrix} 1 \\ B \end{pmatrix} + \delta \left(\begin{pmatrix} (-1-i)/2 \\ 1 \end{pmatrix} C(\tilde{x}, \tilde{y}, t) e^{i\omega\tilde{t}} + \begin{pmatrix} (-1-3i)/4 \\ 1/2 \end{pmatrix} \hat{f}_3 e^{3i\omega\tilde{t}} + c.c. \right) + O(\delta^2).$$

To obtain the equation for the complex amplitude A we extract the frequency ν_{21} and write

$$C = \sqrt{2/3} e^{i(\tan^{-1}(1/8) + \nu_{21} t)/2} A. \tag{.3}$$

After rescaling the spatial coordinates as $(x, y) = \sqrt{(D_u + D_v)/2}(\tilde{x}, \tilde{y})$ we arrive at Eq.(6.3) with the coefficients given by

$$\mu = b/2 + 15|\hat{f}_3|^2/8, \tag{.4}$$

$$\sigma = -(\nu_{21}/2 + 33|\hat{f}_3|^2/8), \tag{.5}$$

$$\gamma = 6\hat{f}_2/\sqrt{65}, \tag{.6}$$

$$\rho = |\hat{f}_3|\sqrt{205/24}, \tag{.7}$$

$$\phi = \tan^{-1}(14/3) + \arg(\hat{f}_3). \tag{.8}$$

As before $\nu = \nu_{22} - \nu_{21}$ and $\eta = \rho e^{i\phi}$.

To give an impression of the temporal evolution of the patterns as they may be seen in experiments we show in (SimulationOver2Periods_withFastOscs.mov) (see also Fig.9.5) a movie of the u-component of the Brusselator. More precisely, we show only the spatial dependence associated with the wavevectors on the critical circle. In terms of the expansion (8.1) the corresponding amplitudes can be written as

$$u_k = Z \left(\left(-\frac{1}{2} - \frac{i}{2} \right) \sqrt{\frac{2}{3}} \sum_{n=-\infty}^{\infty} (X_n + iY_n) e^{in\nu t} e^{i\nu_{21} t/2 + i\omega\tilde{t}} + \left(-\frac{1}{2} + \frac{i}{2} \right) \sqrt{\frac{2}{3}} \sum_{n=-\infty}^{\infty} (X_n - iY_n) e^{in\nu t} e^{-i\nu_{21} t/2 - i\omega\tilde{t}} \right).$$

Here Z represents the steady-state amplitude of the Fourier mode given by the fixed-point solution of Eq.8.2.